NATIONAL CENTRE FOR NUCLEAR RESEARCH

Design and optimization of the strip PET scanner based on plastic scintillators

by

Paweł Kowalski

Supervised by prof. dr hab. Wojciech Wiślicki

Department of Complex Systems, National Centre for Nuclear Research

Co-supervised by prof. dr hab. Paweł Moskal

Institute of Physics, Jagiellonian University

A thesis submitted in partial fulfillment of the requirements for the degree of Doctor of Physics

in the

National Centre for Nuclear Research

May 20, 2021

Declaration of authorship

I, Paweł Kowalski, declare that this thesis entitled, 'Design and optimization of the strip PET scanner based on plastic scintillators' and the work presented in it are my own. I confirm that:

- This work was done wholly or mainly while in candidature for a research degree at this Institute.
- Where any part of this thesis has previously been submitted for a degree or any other qualification at this Institute or any other institution, this has been clearly stated.
- Where I have consulted the published work of others, this is always clearly attributed.
- Where I have quoted from the work of others, the source is always given. With the exception of such quotations, this thesis is entirely my own work.
- I have acknowledged all main sources of help.
- Where the thesis is based on work done by myself jointly with others, I have made clear exactly what was done by others and what I have contributed myself.

Signed: _____

Date: _____

Abstract

The novel whole-body PET system is developed by the J-PET Collaboration. It is built of relatively cheap plastic scintillator strips arranged axially in the form of a cylinder. Usage of plastic scintillators opens perspective for the cost-effective construction of the total-body PET. In order to determine properties of the scanner prototype and optimize its geometry, advanced computer simulations using the GATE software were performed.

Firstly, simulations were verified with experimental results for laboratory prototype. After that, the simulations were used to calculate the NEMA characteristics and maps of efficiency. The spatial resolution, the sensitivity, the scatter fraction and the NECR were estimated according to the NEMA norm as a function of the length of the tomograph, number of the detection layers, diameter of the tomographic chamber and for various types of the applied readout.

Simulations results were used to optimize geometry and working parameters of the J-PET scanner. They were also used to compare the J-PET solution with current commercial technology.

Streszczenie

Nowatorski tomograf całego ciała rozwijany jest w ramach projektu J-PET. Zbudowany jest ze względnie tanich plastikowych scyntylatorów ułożonych osiowo w formę walca. Zastosowanie plastikowych scyntylatorów otwiera perspektywy na zbudowanie taniego tomografu całego ciała. W celu wyznaczenia właściwości prototypu oraz optymalizacji jego geometrii, zostały przeprowadzone zaawansowane symulacje komputerowe z wykorzystaniem oprogramowania GATE.

W pierwszej fazie badań, symulacje zostały zweryfikowane z wykorzystaniem wyników eksperymentalnych, uzyskanych dla laboratoryjnego prototypu. Następnie symulacje zostały wykorzystane do obliczenia charakterystyk NEMA oraz map efektywności. Rozdzielczość przestrzenna, czułość, frakcja rozproszeniowa oraz NECR zostały wyznaczone w funkcji długości tomografu, liczby warstw detekcyjnych, średnicy komory detekcyjnej i rodzaju fotodetektorów.

Wyniki symulacji zostały wykorzystane w celu znalezienia optymalnej geometrii oraz parametrów pracy tomgorafu J-PET. Obliczone charaketerystyki posłużyły również do porównania rozwiązania J-PET z obecnie wykorzystywanymi komercyjnymi tomografami.

Acknowledgements

This thesis is a summary of several years of my doctoral studies in the field of Monte Carlo simulations of the J-PET tomograph. Its creation would not be possible without the effort and support of many people whom I would like to thank here.

First of all, I would like to thank professor Wojciech Wiślicki for patience, substantive support, constructive criticism and review. When I had a moment of weakness, thinking about leaving PhD studies, he encouraged me to continue this work.

The second person without whom this work would not be possible is professor Paweł Moskal. I am very grateful for the opportunity to work in his research group. He has inspired and supported me always when I was struggling with scientific problems.

I would also like to thank all my Colleagues from the Świerk Computing Centre at the National Centre for Nuclear Research (CIŚ NCBJ) and the J-PET teams. They have supported me in the field of cluster computing and data analysis.

In this place I would also like to extend my thanks to Tomasz Świerczek and Sebastian Rutka from Samsung Research and Development Institute. Thanks to them I could reconcile my PhD studies with work as a developer in Samsung company.

Na koniec chciałbym podziękować moim Bliskim. Mamie, za rozbudzenie we mnie ciekawości świata. Tacie, za to że nauczył mnie podstaw matematyki. Mojej kochanej Żonie Beatce, za wieloletnie wsparcie i wiarę w to, że tę pracę uda mi się kiedyś ukończyć.

Contents

Declaration of authorship iii

Abstract v

Streszczenie vii

Acknowledgements ix

Abbreviations xv

Preface 1

1 Introduction to Positron Emission Tomography 3
- 1.1 Interaction of gamma radiation with matter . . . 5
- 1.2 Scintillators . . . 6
- 1.3 Principle of operation of the PET tomograph . . . 7
- 1.4 Types of events in PET . . . 8
- 1.5 Image reconstruction . . . 9

2 The J-PET detector 13
- 2.1 Principle of operation of the J-PET scanner . . . 14
- 2.2 Prototypes of the J-PET tomograph . . . 17
  - 2.2.1 The three-layer 192-strip J-PET prototype . . . 18
  - 2.2.2 The Modular J-PET prototype . . . 20
- 2.3 Future of the J-PET project . . . 21

3 Simulations of the J-PET detector response with the GATE software 23
- 3.1 Implementation of the J-PET scanner within the GATE software . . . 24
  - 3.1.1 Simulated geometries . . . 24
  - 3.1.2 Material and readout properties . . . 27
  - 3.1.3 Sources and phantoms . . . 29
  - 3.1.4 Physical processes . . . 30
- 3.2 Analysis of the GATE output . . . 30
  - 3.2.1 Event selection method . . . 31

4 Verification of simulations using experimental data 39
4.1 Experimental data . . . 39
4.2 Simulations . . . 43

5 Performance characteristics of the J-PET detector 51
5.1 Materials and methods . . . 52
5.1.1 Sensitivity . . . 52
5.1.2 Map of efficiency . . . 53
5.1.3 Spatial resolution . . . 54
5.1.4 Scatter fraction and NECR . . . 55
5.2 Results . . . 57
5.2.1 Sensitivity . . . 57
5.2.2 Map of efficiency . . . 61
5.2.3 Spatial resolution . . . 68
5.2.4 Scatter fraction and NECR . . . 71

6 Comparison of the J-PET tomograph to commercial and the prototype PET devices 77
6.1 Performance of current PET scanners . . . 77
6.1.1 Commercial scanners in medical use . . . 77
6.1.2 PET devices under development . . . 78
6.2 The J-PET scanner vs. competitive solutions . . . 79

7 Optimization of the J-PET detector 83
7.1 Optimization of the construction . . . 83
7.1.1 Scintillators and photomultipliers . . . 84
7.1.2 Single module . . . 85
7.1.3 Detecting chamber . . . 86
7.2 Optimization of the operating parameters . . . 87
7.2.1 Fixed energy threshold . . . 87
7.2.2 Noise energy threshold . . . 91
7.2.3 Time window . . . 93
7.3 Recommendations for further prototypes . . . 94

8 Summary 95

A Measurements of the absorption length dependence on light wavelength 99

B Software developed for the simulation study of the J-PET detector 105
B.1 The GATE Output J-PET Analyzer . . . 106
B.2 The GOJA Manager . . . 109
B.3 The Simulations Manager . . . 110

C Smearing simulation results **113**
C.1 Coordinates x and y 113
C.2 Coordinate z and time 115

Bibliography **117**

Abbreviations

AFOV	**A**xial **F**ield **O**f **V**iew
CRT	**C**oincidence **R**esolving **T**ime
CT	**C**omputed **T**omography
DAQ	**D**ata **A**cquisition
FBP	**F**iltered **B**ack **P**rojection
FEE	**F**ront **E**nd **E**lectronics
FFT	**F**ast **F**ourier **T**ransform
FWHM	**F**ull **W**idth at **H**alf **M**aximum
GATE	**G**eant4 **A**pplication for **E**mission **T**omography
GOJA	**G**ATE **O**utput **J**-PET **A**nalyzer
IFFT	**I**nverse **F**ast **F**ourier **T**ransform
J-PET	**J**agiellonian **P**ositron **E**mission **T**omography
LOR	**L**ine **O**f **R**esponse
MC	**M**onte **C**arlo
MRI	**M**agnetic **R**esonance **I**maging
NECR	**N**oise **E**quivalent **C**ount **R**ate
NEMA	**N**ational **E**lectrical **M**anufacturers **A**ssociation
PET	**P**ositron **E**mission **T**omography
PMT	**P**hoto**m**ultiplier **T**ube
PSF	**P**oint **S**pread **F**unction
SiPM	**Si**licon **P**hoto**m**ultiplier
SNR	**S**ignal to **N**oise **R**atio
SSRB	**S**ingle **S**lice **Re**b**i**nning
STIR	**S**oftware for **T**omographic **I**mage **R**econstruction
TOF	**T**ime **O**f **F**light

TOT **T**ime **O**ver **T**hresholds

WLS **W**ave**l**ength **S**hifter

Preface

At the beginning of the 21^{st} century, humans are witnesses of the 4th industrial revolution. New technologies and inventions appear every day. There are intelligent factories, autonomous cars, human-like robots and futuristic spaceships. Although there is a huge improvement also in a field of medicine, people are still losing in fight with many diseases. One of such diseases is cancer. In Poland, during three last decades, number of people ill for malignancies grew up twice.

Even though there are methods of diagnosing and treatment of cancer, these methods are often not available for average person. One of the methods of diagnosing tumors is the Positron Emission Tomography (PET). While in highly developed countries, like in the USA, there are thousands of PET tomographs, in many other regions of the world access to PET scanners is very limited due to its price. Significant part of this amount is a cost of inorganic scintillating crystals used in a construction of the scanner.

One would think, if these inorganic scintillators are so expensive, maybe they could be replaced with something else? Plastic organic scintillators, which are more than order of magnitude cheaper than inorganic ones and exhibit good detecting performance, seem to be an obvious alternative. Although the PET tomography was developed in late 1950s, no one till now managed to build a medical PET using plastic scintillators.

However, the situation may change in an upcoming decade. Novel PET system based on plastic scintillators is developed by the J-PET Collaboration. The group, lead by Professor Paweł Moskal, was established at the Jagiellonian University in Cracow in 2012. Nowadays, it brings together scientists not only from the Jagiellonian University, but also from many other institutes, like the National Centre for Nuclear Research (NCBJ) in Świerk among them.

At the NCBJ there is a team focused on computational methods. Computing infrastructure of the Świerk Computing Centre (CIŚ) has been used to perform the Monte Carlo simulations of the prototype PET device, to analyze measurement data and to develop methods of signal and image reconstruction.

This thesis provides a complete numerical simulation of the J-PET scanner, starting from interactions of photons in plastic, light propagation along scintillation strips, studying different sources of background and leading to determination of measures to quantify scanner's performance and resolution. These studies are performed in order to understand all important properties of the apparatus, evaluate them according to the medical NEMA standards and optimize the detector's design. Before describing details of performed studies, some basics of the PET tomography are presented in the 1-st chapter. After that, in the 2-nd chapter, the J-PET tomograph is presented. In 3-rd chapter, methods of simulations are explained, while the 4-th chapter contains details of verification of simulations with measurement data. The 5-th chapter contains results of performed studies, 6-th chapter relates these results to the state of art and 7-th chapter contains some tips that could be used while designing the next prototypes of the J-PET scanner. All studies are summarized in 8-th chapter.

Chapter 1

Introduction to Positron Emission Tomography

Positron Emission Tomography (PET) is one of the nuclear medicine imaging techniques. In contrast to Computed Tomography (CT) or Magnetic Resonance Imaging (MRI), which allow to reconstruct exact shapes and positions of organs and tissues, PET is used mainly to observe metabolic processes in the body. Currently, most of imaging devices in the nuclear imaging are hybrid devices, which combine at least two techniques: PET with CT (PET-CT) or PET with MRI (PET-MRI). Only the combination of the structural (CT or MRI) and functional (PET) scans provides full information about the state of the patient's body (Fig. 1.1). While CT modality requires an external source of radiation (X-rays), in PET measurements, gamma radiation originating from the electron-positron annihilations is registered. The source of these positrons is the positron-emitting radionuclide tracer, based on biologically active molecules, introduced into the patient's body. After measurement, image of tracer concentration inside the body is reconstructed using the computer-aided methods.

The biologically active molecule most often used for PET is fludeoxyglucose (^{18}F-FDG or just FDG) [2]. The FDG is a glucose analog, with the radionuclide fluorine-18 substituted for the normal hydroxyl group in the glucose molecule. When the FDG is used as a tracer, the concentration of the tracer indicates tissue metabolic activity and corresponds to the regional glucose uptake. This tracer is commonly used to explore the possibility of cancer metastasis, due to a fact that cancer cells have usually faster metabolism than the

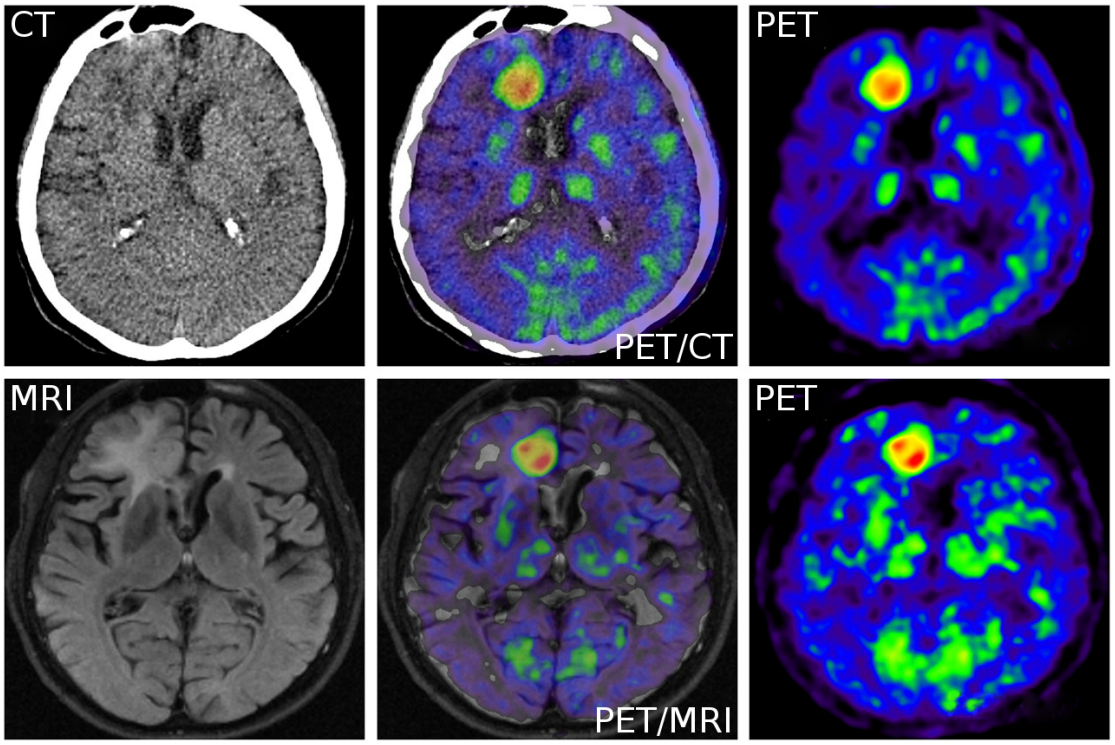

FIGURE 1.1: Comparison of the CT, MRI and PET images of a brain and combinations of these images. While the PET image shows the metabolism of different brain regions, both CT and MRI images show what are the structures inside the brain. Full information may be obtained only from combined images (image from Ref. [1]).

healthy ones. Although in most PET scans the FDG is imaged, many other radioactive tracers are used in PET to visualize concentration of other types of molecules of interest in tissues.

As it was mentioned above, the PET measurement involves detection of gamma radiation from annihilation of the positrons from the $\beta+$ active source with an electron in the surrounding tissue. Gamma radiation (γ-rays) is a penetrating electromagnetic radiation of a kind arising from the radioactive decay of atomic nuclei. It was discovered in 1900 by a French chemist Paul Villard during his studies of radiation emitted by radium. Ernest Rutherford has also investigated this kind of radiation and he called it the γ-rays.

While γ-rays were discovered in the beginning of the 20th century, the idea to use it for nuclear imaging appeared in the late 1950s. The first PET scanner was build in 1961 by James Robertson and his associates at the Brookhaven National Laboratory. It was a single-plane PET scanner, nicknamed the "head-shrinker" [3]. In late 1970s, the first device based on the 2-dimensional arrays of crystal detectors was developed and after that, the ring system, that has become the prototype of the modern PET scanner, was

proposed. In the early 1990s David Townsend, Ronald Nutt and co-workers proposed to combine PET with CT. Their invention was even named by TIME Magazine "the medical invention of the year" in 2000 [4]. Through next years, till now, teams all over the world, work on improvements of performance of the devices and they try to build the whole-body and modular PET scanners [5–10].

1.1 Interaction of gamma radiation with matter

Gamma rays interact with matter via following processes: photoelectric effect, Compton scattering and electron-positron pair production. These processes may be registered using scintillators. The first two processes are essential from the point of view of the PET technique, but for completeness, all three processes are shortly described in below paragraphs.

The photoelectric effect is the emission of electrons (called photo-electrons) or other free carriers when light shines on a material. The photon must have energy high enough to cause an emission of an electron. Incoming photon is completely absorbed and its energy ejects an electron from its host atom. This emitted electron (known as a photo-electron) moves through the scintillator, exciting many other molecular orbitals in the process and causing electrons to jump to higher energy levels. When these electrons return to their ground state, they re-emit absorbed energy as photons.

The Compton scattering is an inelastic scattering, in which a gamma (or X-ray) photon is scattered by a charged particle, usually an electron. It results in a decrease in energy (increase in wavelength) of the photon. This energy is transferred to the recoiling electron. Similarly to the photoelectric effect, the energy absorbed by the electron is subsequently re-emitted as photons. The differential cross section of the Compton scattering may be described with the Klein-Nishina formula [11].

The pair production is the process of creation of pair particle-antiparticle from a neutral boson, e.g. the pair electron-positron from the photon. If the photon is near an atomic nucleus, the energy of the photon may be converted into the electron-positron pair. The minimum energy for this process to occur is 1.022 MeV. The pair production is the dominant mode of photon interaction with matter for high-energy photons.

1.2 Scintillators

Scintillator is made of material in which part of the incident radiation is absorbed and then reemitted because of the luminescence, in form of light. If the reemission occurs immediately (within 10^{-8} s), the process is called fluorescence. Otherwise, if the emission is delayed because the excited state is metastable, the process is called phosphorescence (the delay time may last from few microseconds to hours depending on material [11]). Scintillators may be divided into classes: organic crystals, organic liquids, plastics, inorganic crystals, gases and glasses. Each type of the scintillating material has some unique properties and fits to a different application.

Inorganic crystal scintillators are grown in high temperature furnaces and are made of alkali halides (i.e., NaI, CsI) or oxides (i.e., BGO). They have scintillation properties due to their crystalline structure. This structure creates energy bands between which electrons can jump up to higher energy levels by excitation through ionizing radiation or down to lower energy levels by deexcitation through the emission of (visible) photons. Because of the absorption of the radiation, electrons go into excited states and then back into ground state with the emission of light. For inorganic crystals and energies below 1 MeV, both photoelectric effect and Compton scattering occur.

Plastic organic scintillator is a compound of aromatic hydrocarbons containing benzene rings. Its most distinguishing feature is a very rapid decay time of the order of a few nanoseconds or less. Light in organic scintillators arises from transitions of valence electrons of the molecules, excited by radiation. These electrons are delocalized and occupy π molecular orbitals. The π orbitals interact with each other and create a common nodal plane. Excited states of molecules may be divided into singlet excited states and triplet excited states (Fig. 1.2). Deexcitation of the singlet state leads to the fluorescence, which has the lifetime on the order of nanoseconds. Deexcitation of the triplet state leads to the phosphorescence, which has the lifetime of the order of milliseconds. When high time resolution is needed, the fluorescence is more important. For organic scintillators and energies below 1 MeV, gamma photons interact with a mater mainly via Compton scattering [12]. Photoelectric effect is highly dependent on the effective atomic number of the material, which is few times lower for plastics than for crystals.

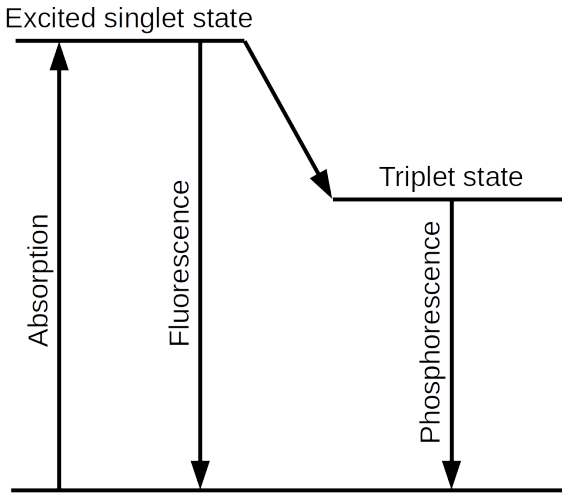

FIGURE 1.2: Energy levels of an organic molecule

1.3 Principle of operation of the PET tomograph

Positron-emitting radionuclide is injected into the patient's body as a radiotracer, i.e. joint to a biologically active molecule, and therefore absorbed by tissues. Such radiotracer may be based on glucose molecule which is faster absorbed by tissues with faster metabolism.

Emitted positrons either annihilate directly with electrons from tissues or form with it an unstable bound state called positronium [13, 14]. Majority of annihilations and positronium decays cause the emission of two back-to-back gamma photons with energy 511 keV in opposite directions. These gamma photons are detected by the opposite-side modules of a ring detector. Such modules are built of scintillating materials and photomultipliers. When gamma photon interacts with the scintillator (such interaction is colloquially called a hit), scintillating light is propagated to the coupled photomultipliers and converted into voltage signals. If two gamma photons are registered within a fixed time window, they are meant to be in a coincidence. The line connecting two hits in a coincidence is called the line of response (LOR). Set of LORs is used to reconstruct the final image of the source.

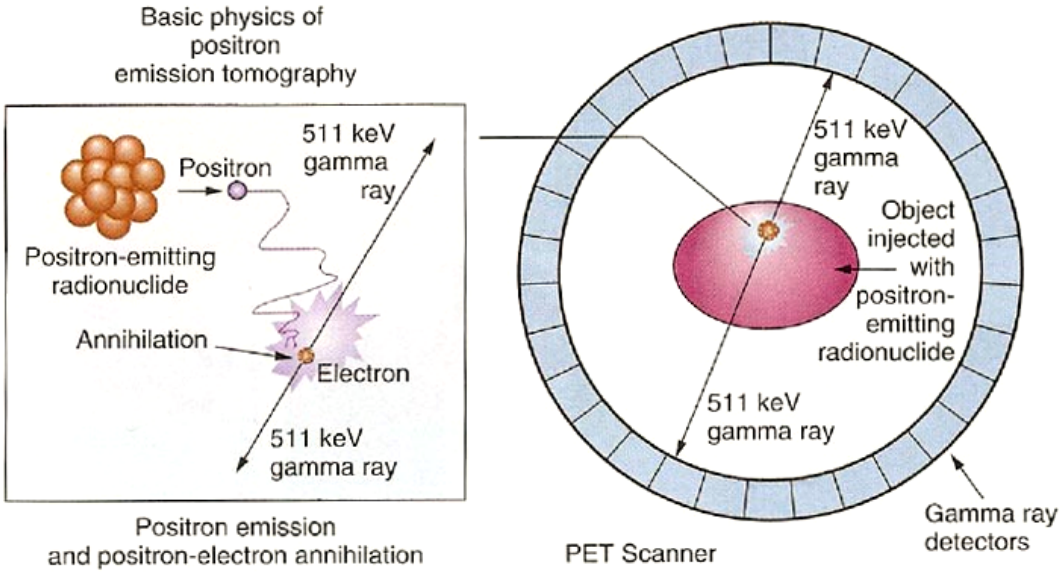

FIGURE 1.3: Basic physics of positron emission tomography; (left) annihilation of a positron and an electron and emission of 2 back-to-back gamma photons, (right) two emitted gamma photons define LOR inside of the detecting chamber of the PET tomograph (image from Ref. [15])

1.4 Types of events in PET

An event is defined as a set of consecutive interactions of gamma photons, originating from a single e^+e^- annihilation, and all interactions of secondary particles. As explained earlier, for 511 keV gamma photons such interactions may be the photoelectric effect or Compton scatterings. If the hits are detected within the fixed time coincidence window, they are operationally considered to originate from the same annihilation event. Any two hits within an event may form a coincidence. Coincidences may be classified into three types: true, scattered and accidental.

While true coincidences are desirable, the scattered and accidental coincidences contribute to the background, hinder the reconstruction of the image and deteriorate its final quality. Scattered coincidences may be divided into the detector- and phantom-scattered (or body-scattered in case of real medical measurements) coincidences. Detector-scattered coincidences are defined as coincidences in which at least one of interactions does not originate from the annihilation photon but from another point being a scattering center in the detector, either the primary or secondary one. Phantom-scattered coincidences are those in which at least one of the annihilation photons was scattered in the phantom

before the detection. Coincidences of hits from different annihilations are called accidental or random. Pictorial definitions of these different types of coincidences are shown in Fig. 1.4.

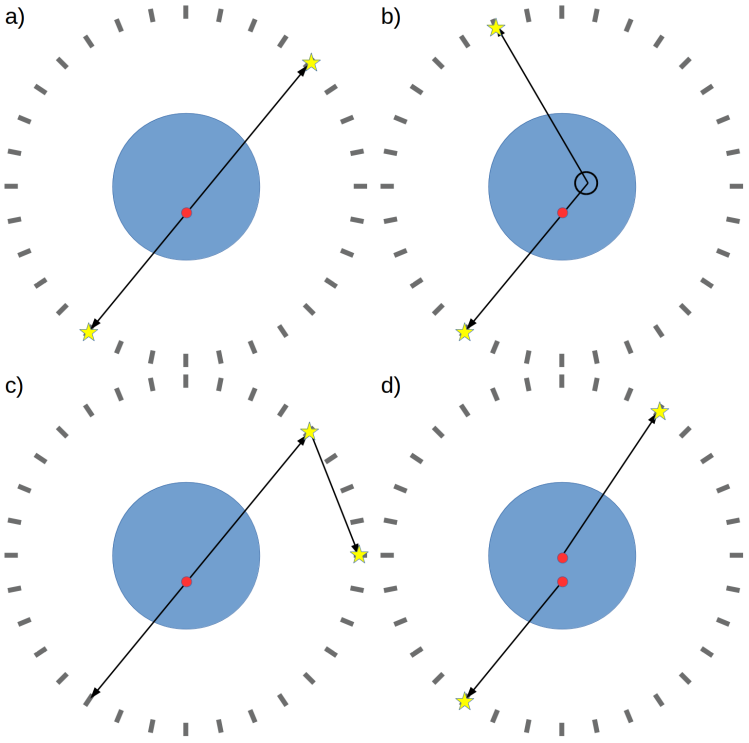

FIGURE 1.4: Pictorial definitions of different types of coincidences: a) true coincidence, b) phantom-scattered coincidence, c) detector-scattered coincidence and d) accidental coincidence. Blue large circle denotes the phantom, red dots denote the annihilation points, black circle denotes the scattering place in the phantom and yellow stars indicate interactions of gamma photons in the detector.

1.5 Image reconstruction

Fig. 1.5a shows how the set of LORs is used to reconstruct the image. Regions with the biggest density of LORs' crossings are considered to be regions containing points of annihilations. Unfortunately, there are many points that may be interpreted as annihilation points while in fact they are not (yellow dots). Precise information based on the time of flight (TOF) method, may be used to decrease this image background.

If the TOF information is used, it means that there is not only information about line connecting two detectors but also about times of interactions. Thanks to that we can estimate an interval of LOR with the highest probability of annihilation. On this way we

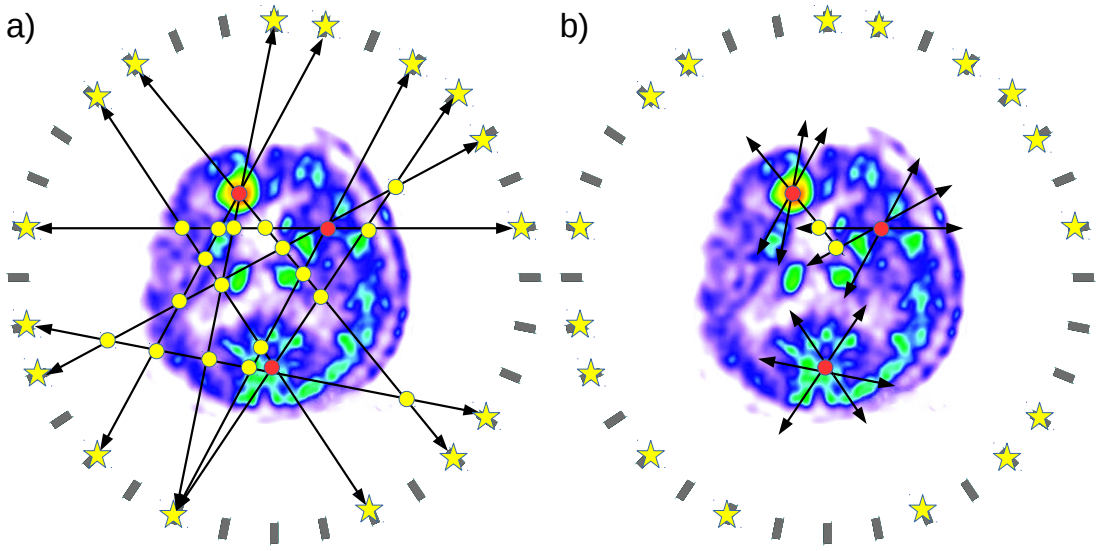

FIGURE 1.5: LORs without (a) and with (b) the TOF information included. Red dots denote the annihilation points, yellow dots denote the points that may be interpreted as annihilation points while in fact they are not.

can improve the resolution of the scanner (Fig. 1.5b). Difference between the non-TOF PET and the TOF PET scanner is visualised in Fig. 1.6. Adding the TOF information, number of false coincidences is strongly reduced, thus improving image quality.

There are many methods of the PET image reconstruction. Here, in order to give an example, only two of them are shortly described: Filtered Back Projection method (FBP) [17] and Maximum Likelihood Expectation Maximization method (MLEM) [17].

The FBP is an analytic method of image reconstruction. It consists of two main steps: back projection and filtering. At the back projection stage, for each image voxel, value of the emission density function (in units of emissions/volume) is computed as a sum of probabilities of each event. Each LOR is back-projected onto the voxels according to the probability of registering a given LOR under the condition that the registered event was emitted from a given voxel. Such obtained image is blurred. Because of that the filtering is performed. The image is transformed using the Fast Fourier Transform (FFT) into frequencies domain. The spectrum is then convoluted with the ramp Ram-Lak filter [18] (which leaves all frequencies unchanged except those above a cut-off, which are eliminated) and transformed again using the Inverse Fast Fourier Transform (IFFT) into the image domain. The 3D version of the algorithm consists of reconstructions of 2D images in slices and combining them into the single 3D image.

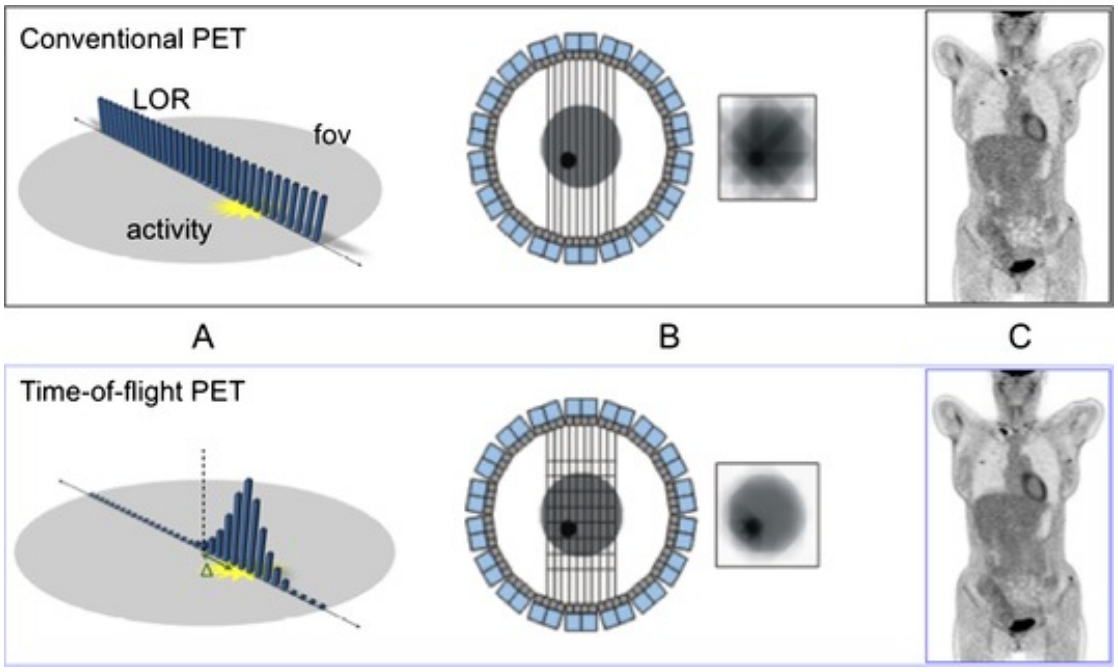

FIGURE 1.6: Difference between the conventional (non-TOF) PET scanner and the TOF PET one (image from Ref. [16]). (A) In conventional PET scanner, point of annihilation may be located anywhere along the LOR, while in case of TOF PET scanners, distribution of the annihilation point along LOR is non-uniform. This influences the resolution of the detector (B) and quality of reconstructed images (C).

The MLEM is an iterative method, widely used in commercial PET scanners. In this method every voxel of the 3D image is updated during each iteration with the value that maximizes the Poisson likelihood. The iterative methods make it possible to incorporate the Poisson probability density of registering a number of photons, taking into account noise and a number of other relevant physical features. The MLEM is an accurate and globally convergent algorithm [19].

There are many modifications and implementations of the above reconstruction algorithms. Set of reconstruction algorithms is implemented e.g. in the Software for Tomographic Image Reconstruction (STIR) package [20]. STIR is an open source software, which aims to provide a multi-platform object-oriented framework for all data manipulations in tomographic imaging.

Chapter 2

The J-PET detector

The J-PET is a novel PET scanner built of plastic scintillator strips [8, 21–23], in contrast to the classical PET scanners, based on inorganic crystal scintillators [24–31]. In case of crystal tomographs, annihilation photons are registered using the photoelectric effect, while in the J-PET the Compton scattering is used. In the J-PET, relatively low detection efficiency (in comparison to crystal PET scanners) is compensated with a high time resolution of plastic scintillators, an application of few concentric detection layers and a large Axial Field of View (AFOV) of the detector [23]. The use of plastic detectors opens perspective for the cost-effective construction of the total-body PET tomographs.

In such a total-body PET scanner, it would be possible to image a whole patient's body without moving the patient along the axis of the device. The total-body technique would increase the effective sensitivity, decrease the time of the examination and reduce a necessary image blur due to the patient's or scanner's movements when the whole body has to be examined. The clinical advantages of the total-body scanner are extensively discussed in Refs [32–35]. Such a solution gives a possibility of the significant reduction of radiation dose needed for the whole-body scan, possibility of usage of the short-lived tracers and possibility of studies of the kinetics in many organs simultaneously. Additionally, the dynamic range of the total-body PET scanners is much broader than that of classical ones, which allows for accurate measurements of the radiotracer distribution in both low and high distribution regions. It results in the fact that the radiotracers may be followed for a longer time before signal disappearance. Also the feasibility of the

multitracer studies is improved. One has to realize, however, that building a crystalline total-body PET may be suppressed by cost [1].

Much lower costs of building of the J-PET scanner based on plastic scintillators (due to the less expensive detector material and reduced number of the electronic channels) can make the total-body PET diagnostics more widely available. In addition, in the J-PET solution with axially arranged plastic strips, the readout is placed outside the detection chamber simplifying PET/MR hybrid construction and enabling extension of the AFOV without a significant increase of costs. Moreover, the J-PET solution enables to built a detector from multi-strip modules, the number of which can be adopted to the size of the patient. Such modular J-PET can contribute to broader applications of cancer diagnostics [36], especially for people with large size of the body or those with claustrophobia.

2.1 Principle of operation of the J-PET scanner

The J-PET scanner is built of axially-arranged plastic scintillator strips (Fig. 2.1a). The principle of operation of the J-PET tomograph may be explained using a simplified 2-strip model (Fig. 2.1b). Each scintillator is readout by two photomultipliers located at the ends of the strip. Optical photons, generated in the scintillator due to the interaction of the gamma photon with the scintillator and consecutive cascade of secondary photons, propagate to the ends of the strip. Thus, the scintillator strip acts also as a lightguide. Having times of arrivals of light signals to the ends of the strips, one can estimate the position and time of the interaction of the 511 keV photon [9, 21, 22, 37, 38]. Having positions and times of two interactions in coincidence, it is possible to calculate the point of emission along the LOR (see Sec. 1.3).

In the scintillation process, even few thousands of optical photons may be emitted. Due to the limited angular acceptance, absorption of photons in material and efficiency of photomultipliers, at best only few hundred of them are detected by the photomultipliers. Measured voltage signals consist of contributions of tens to hundreds of single-photon signals. Each photon reaches the photomultiplier at a slightly different time. It causes that final signal lasts few nanoseconds. Examples of such signals are presented in Fig. 2.2.

[1] The first estimations of the commercial costs of such scanners points to about 10 mln dollars [35].

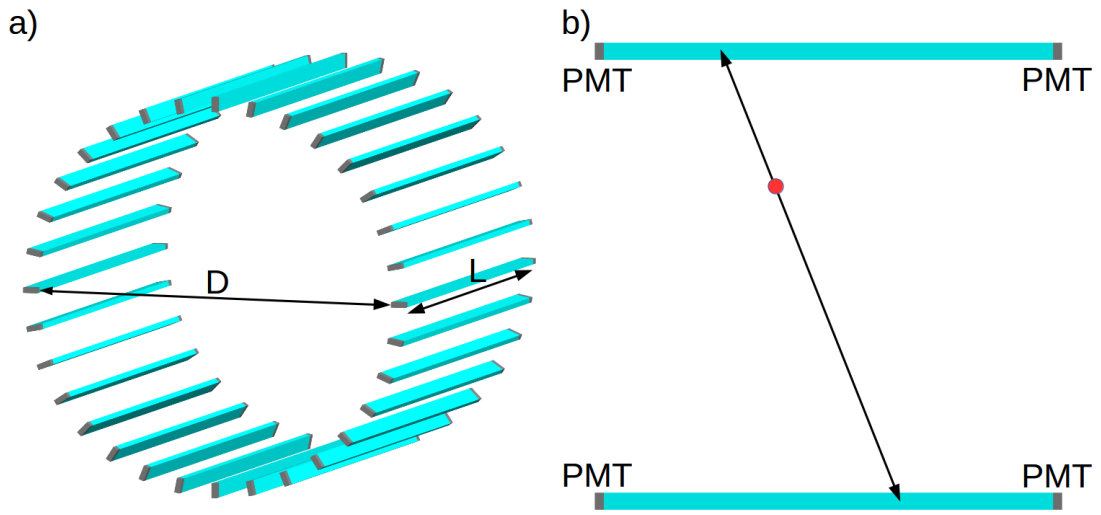

FIGURE 2.1: a) The exemplary geometry of the J-PET scanner; scintillators are cyan and photomultipliers (PMT) are gray. **D** stands for the diameter of the scanner and **L** for its length. For better visualization only 32 strips are shown. b) Pair of scintillator strips and two annihilation photons defining the LOR (details in the text). Red point denotes the annihilation point.

Signals measured by photomultipliers are sampled at 4 voltage levels using dedicated front-end electronics (FEE) boards [39] and collected with the triggerless data acquisition system [40, 41]. After that, having 8 time values (4 for raising edge of the signal and 4 for the trailing one) the signal is reconstructed using the algorithm based on the compressive sensing theory [37, 38]. Having signals from both sides of the strip, the time and the position of interaction is estimated [42]. Acquired data are processed offline using the JPetFramework software [43, 44] - from raw signals obtained from the FEE boards to the final reconstructed images.

Measurements showed that 80 ps hit-time resolution (standard deviation) for a 30 cm strip is achievable, allowing to determine the position of the interaction along the strip with spatial resolution of 2.2 cm (full width at half maximum [FWHM]) [21]. The hit-time resolution depends on the length of the strip - the longer the strip, the better the hit-time resolution.

While the J-PET scanner allows to measure the hit-time precisely, it does not allow to measure the deposited energy directly. As it was explained in the previous chapter, in crystalline scintillators incident gamma photons undergo photoelectric effect, while in case of plastic scintillators photons interact mainly via Compton scattering. Because of that, in the J-PET solution, contrary to classical PET scanners, there is no direct

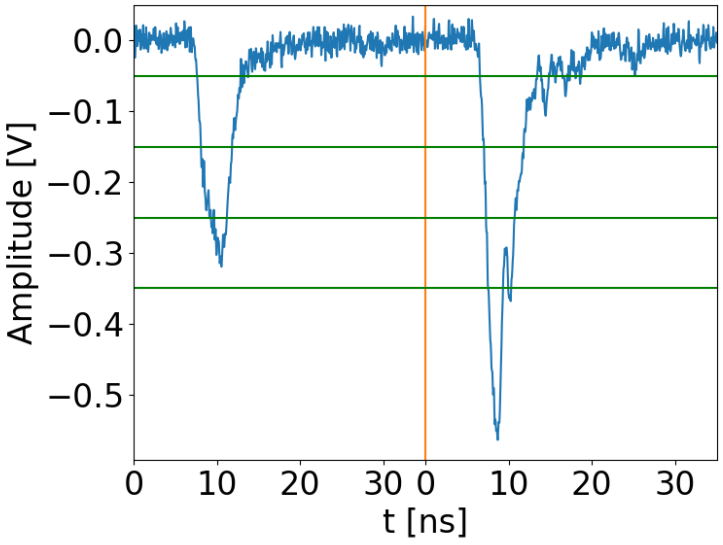

FIGURE 2.2: Examples of two voltage signals measured at the ends of the same scintillator. Each signal is measured at 4 electronic levels marked as green horizontal lines. The amplitude of the signal at the right end of the scintillator is higher, which means the interaction was nearer to the right end of the strip.

information on energy deposition of the interacting photon. Fortunately, a deposited energy is uniquely related to the time over thresholds (TOT) value, which is a sum of times of signals on 4 electronic levels of leading edge of the signal.

While in the method of energy determination based on the charge measurements, the relation between the charge and the energy is linear, in the approach based on the TOTs measurements, the relation is nonlinear (it is due to a nonlinearity of the width versus amplitude of a signal dependence [45]). In order to obtain the experimental energy calibration curve, the measurements performed with the annihilation chamber were used [46]. TOTs for monochromatic gamma photons from positron-electron annihilation were selected and used to determine the fit function. In the analysis presented in [46] it was shown that the data may be reproduced with the following function:

$$TOT(E_{dep}) = A_0 + A_1 \ln\left(E_{dep} + A_2\right) + A_3 \left(\ln\left(E_{dep} + A_2\right)\right)^2, \tag{2.1}$$

where A_0 = -2332.32 ns, A_1 = 632.04 ns/keV, A_2 = 606.91 keV and A_3 = -42.08 ns/(keV)^2. The inverse function, that allows to calculate the deposited energy having the TOT value, has the following form:

$$E_{dep}(TOT) = e^{\left(-A_1 + \sqrt{A_1^2 - 4A_3(A_0 - TOT)}\right)/(2A_3)} - A_2. \tag{2.2}$$

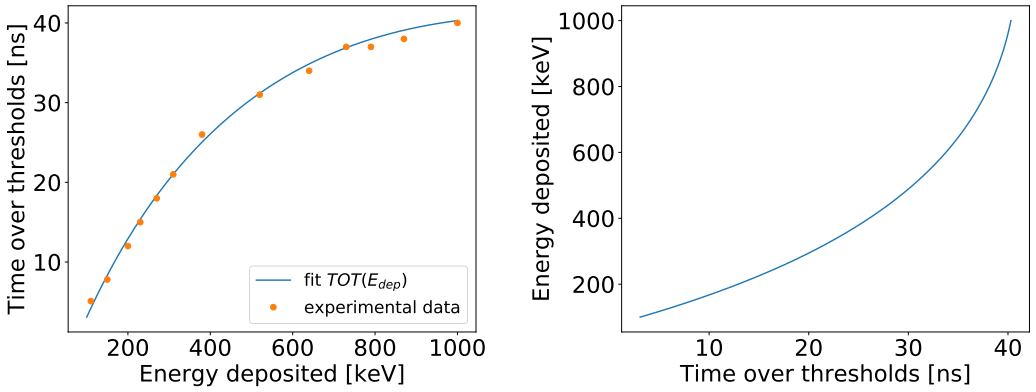

FIGURE 2.3: (left) Experimental data and the fit (Eq. 2.1); (right) dependence of energy deposited on TOT (Eq. 2.2); more details in text and in Ref. [46].

Both experimental data and above calibration curves are visualised in Fig. 2.3.

The fractional energy resolution for the energy deposited by the annihilation photon in the plastic scintillator strips was measured for a single strip J-PET prototype and it amounts to $\sigma(E)/E \approx 0.044/\sqrt{E(MeV)}$ [21].

2.2 Prototypes of the J-PET tomograph

The strips of the J-PET scanner may have different parameters and be arranged in different configurations. Till today, 4 prototypes were build. Additionally, in simulations some simplified geometries were tested to support designing and optimization of next prototypes (simulated geometries are described in next chapter).

The first prototype was built of only two 30-cm-long scintillator strips. The second prototype, which was the first one with the cylindrical detecting chamber, was built of 24 30-cm-long strips. The third one was built of 192 50-cm-long strips and these strips were arranged into 3 layers. The fourth prototype is the portable and modular J-PET tomograph with 50 cm AFOV. This tomograph consists of 24 modules, each with the weight of about 2 kg only [47].

Although some simulations of the 2-strip, the 24-strip and the modular prototypes were performed, only the 192-strip prototype is described in details, cause simulations of this prototype were used to verify the simulations (see Chap. 4). However, the modular prototype is also shortly explained.

2.2.1 The three-layer 192-strip J-PET prototype

The three-layer 192-strip J-PET prototype is colloquially called the "big barrel" (Fig. 2.4). The scanner consists of 192 50 cm x 19 mm x 7 mm scintillator strips. Strips are mounted between two square aluminum plates attached to cuboid frame and are arranged into 3 layers:

- inner layer with radius (from the axis of the scanner to the center of the strip) of 425 mm and 48 scintillator strips,
- middle layer with radius of 467.5 mm and 48 scintillator strips,
- outer layer with radius of 575 mm and 96 scintillator strips.

Drawing of the segment of the plate is presented in Fig. 2.5. Additionally, the scintillators are wrapped with the black Pokalon foil to limit escaping light and thus isolate the scintillators optically.

In case of the "big barrel" prototype, scintillator strips were made of the EJ230 material. This material has the following properties: atomic composition of $C_{10}H_{11}$, density of 1.023 g/cm^3, scintillation yield of 9700 1/MeV and refraction index of 1.58. The emission spectrum of this material is presented in the left panel of Fig. 2.6. Maximum of

FIGURE 2.4: The three-layer 192-strip J-PET prototype, colloquially called the "big barrel". (left) Photography of the laboratory with the J-PET prototype. The detector is visible in the main plan. Also the rack with the computing units and the high voltage power supplies is visible in the right part of the photography. (right) Scintillator strips are covered with the black Pokalon foil and mounted between two square aluminum plates. Aluminum tubes outside the detector chamber are the slots for the photomultipliers.

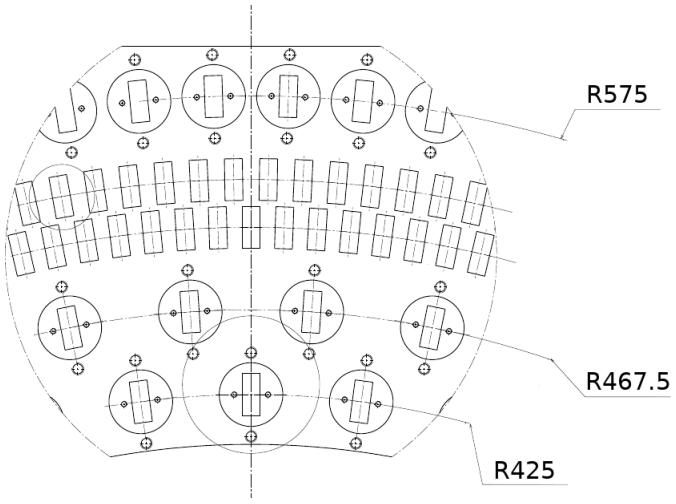

FIGURE 2.5: Drawing of the segment of the plate. The holes, through which the scintillators pass, are drawn with rectangulars. One can see that there are 5 rings of scintillator slots. Two rings (4th and 5th from inside) are dedicated for future development.

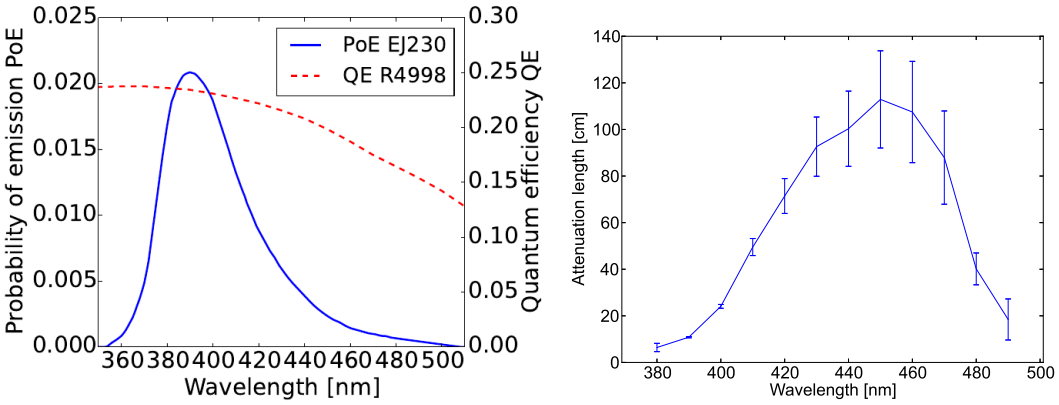

FIGURE 2.6: (left) Emission spectrum of the EJ230 material and quantum efficiency of the R4998 photomultiplier; (right) absorption length of the EJ230 material (error bars represent the standard deviation of the fitted absorption lengths for subsequent wavelengths; curve is to guide one's eye; details in App. A)

emission is at 391 nm. Photomultipliers used in the first prototype of the J-PET scanner were produced by Hamamatsu (model R4998). The quantum efficiency of the R4998 photomultiplier is presented in the left panel Fig. 2.6. While all mentioned properties were provided by the producers of the scintillators or the photomultipliers, the dependence of absorption length on light wavelength was not given. It was measured by us and is presented in the right panel of Fig. 2.6. The measurement procedure is described in details in App. A.

2.2.2 The Modular J-PET prototype

The Modular J-PET prototype is built of 24 axially arranged modules of scintillators (Fig. 2.7). Each module consists of 13 0.6x2.4x50 = 72 cm^3 scintillator strips. Matrices of 4 silicon photomultipliers S13361-6674 Hamamatsu are attached to both ends of each scintillator. In the future also the wavelength shifter (WLS) strips will be attached to the modules as visualised in Fig. 2.8. In such a configuration the scintillators will be used to measure the time of the interaction, while the WLS strips will be used to measure the position of the interaction along the strips. The position measurement will be performed with constant resolution, independent on the position along the strip and the length of the strip.

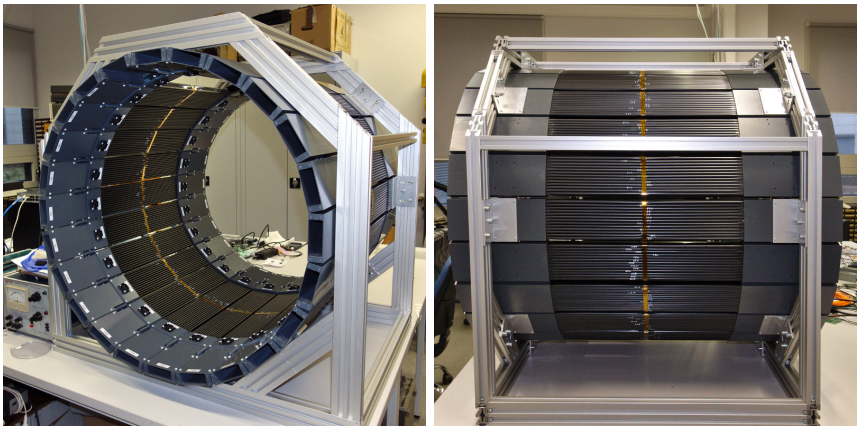

FIGURE 2.7: The 24-module Modular J-PET prototype.

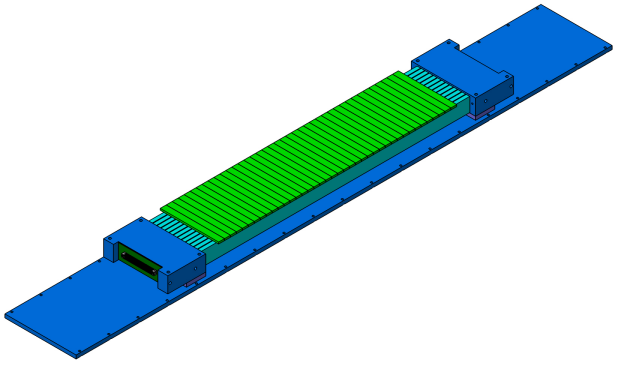

FIGURE 2.8: The geometry of the prototype module for the scanner based on both SiPM photomultipliers and WLS strips. Scintillator strips (light blue) in the prototype module are arranged into clusters consisting of over a dozen of strips. The WLS strips (green) are arranged perpendicularly to the scintillator strips. The results of the first experimental tests performed for the single plastic strip with array of WLS strips are reported in Ref. [48].

2.3 Future of the J-PET project

Although, the main target application of the J-PET scanner is the medical diagnostics, the device may be also used for some physics experiments, like studies of the positronium atoms (positronium imaging [13, 14, 49], positronium annihilation lifetime spectroscopy (PALS) [50–54]) and studies of annihilation-photon's polarization [55–58].

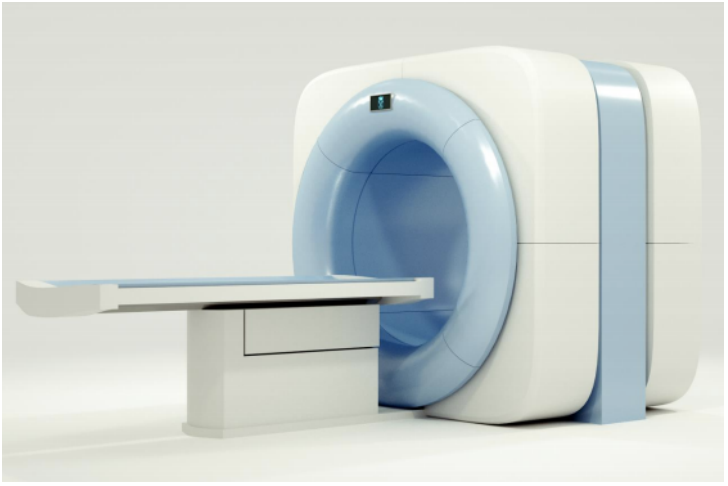

FIGURE 2.9: Visualisation of the future J-PET tomograph. Courtesy of K. Wołek. Prepared for the J-PET Collaboration.

The J-PET scanner may bring a breakthrough in the field of accessibility of the total-body PET tomography. However, some technical problems must be still resolved and medical certification must be performed. In the future, when the device will be already certified for medical purposes, it would look like in Fig. 2.9 and hopefully it will be possible to find such a J-PET tomographs also in Polish hospitals.

Chapter 3

Simulations of the J-PET detector response with the GATE software

Nowadays, there are at least few powerful Monte Carlo packages that are used for the nuclear medicine simulations. Two of them are Geant4 Application for Tomographic Emission (GATE) [59–61] and FLUKA [62–64]. Both agree well and sufficiently reproduce the empirical data [65, 66]. However, it seems that GATE is more often used for simulating PET devices, while FLUKA for planning proton therapies. Moreover, GATE is an open source software, while FLUKA is distributed only in a binary format. Because we wanted to have a possibility to modify code of the tool to adjust it to our purposes, we have decided to use GATE for the J-PET simulations.

GATE is based on the GEometry ANd Tracking (Geant4) platform. Geant4 [67–69] simulates interactions of radiation and material particles with matter using Monte Carlo methods, whereas the GATE package adapts the Geant4 toolkit to use in nuclear medicine. Despite its complexity, GATE is easily configurable using script language. In GATE, there are many facilities for designing PET scanners: repeaters that allow to design periodic structures of scanners, possibility of usage of advanced four-dimensional phantoms or ability to simulate time-dependent phenomena (like breathing, or changing of source activity). Thanks to its simplicity and configurability, GATE is used in many disciplines of medical physics to simulate complex devices and therapies. It was also

used in simulations of the J-PET detector to obtain the performance characteristics, to analyze the background given by accidental coincidences and multiple scattering of gamma photons and to prepare the input for development of algorithms of image reconstruction. In this chapter, it is explained how the J-PET detector was implemented within the GATE software and how the GATE output was analyzed for the purpose of studies presented in further chapters.

3.1 Implementation of the J-PET scanner within the GATE software

In order to perform the simulations of the J-PET scanner, firstly, the geometry of the scanner had to be described in the GATE script language. In order to describe the geometry (especially the prototype geometry), there is often need to define the physical properties of the materials used: the scintillator material and photodetectors. After defining geometry and materials, following elements were adjusted: physical processes taken into account, sources, phantoms, random numbers generator and time of simulations. All listed steps are described in following sections.

3.1.1 Simulated geometries

Simulations of the J-PET were performed for two major setups of the detector: the first in which the strips were placed uniformly on the side wall (or walls in case of multi-layer geometries) of the cylinder, the second in which scintillator strips were grouped into the cuboidal modules and also placed on the side wall of the cylindrical detecting chamber (this solution is called Modular J-PET).

In case of the first solution, simulations for different lengths and thicknesses[1] of scintillator strips, diameters of the detecting chambers, numbers of detection layers and for few readouts were performed. Three diameters D of the detector chamber (75 cm, 85 cm and 95 cm), four lengths L (20 cm, 50 cm, 100 cm and 200 cm) and two thicknesses T (4 mm and 7 mm) of scintillators were taken into account, for both single- and double-layer geometries.

[1]Thickness is a strip dimension perpendicular to both axis and radius of the detecting chamber.

The diameter D (see Fig. 2.1 from previous chapter) is defined as a distance between inner walls of the opposite strips. For the double-layer geometries, the outer layer consists of the same number of strips arranged in the cylinder with the radius larger by 3 cm (Fig. 3.1). The diameter of a double-layer geometry is defined as a distance between inner walls of the opposite strips of the inner layer. Values of the diameter were chosen as typical for the presently available tomographs [31]. Examples of visualisation of the J-PET geometries may be found in Fig. 3.2).

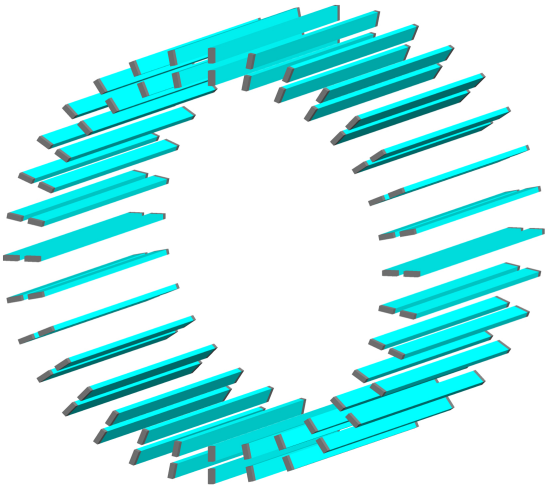

FIGURE 3.1: The exemplary geometry of the double-layer J-PET scanner. For better visualization only 32 strips in each layer are shown. Simulations of fully filled cylinder were performed.

The depth (size of the strip along the radius of the scanner) of each scintillator is 20 mm. Presently used crystalline tomographs have crystals with depths 20-30 mm, while their cross-sections (perpendicular to the radius of the scanner) range from 4 x 4 mm^2 to 6.3 x 6.3 mm^2 [2, 31]. Axial field of view L was tested in the range from the typical present tomographs (about 20 cm) to 200 cm whole-body scanners. Number of strips

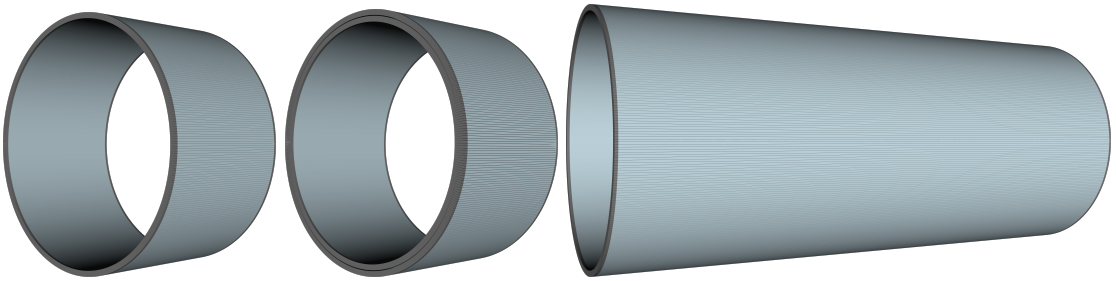

FIGURE 3.2: Example geometries of the J-PET scanner with diameter D = 85 cm: left - 1 layer, L = 50 cm; middle - 2 layers, L = 50 cm; right - 1 layer, L = 200 cm.

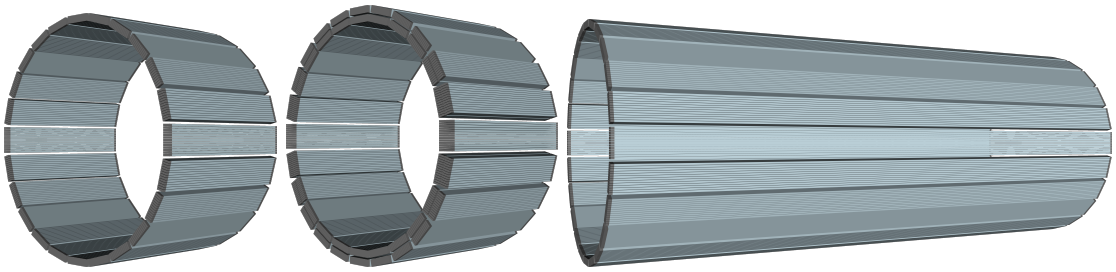

FIGURE 3.3: Example geometries of Modular J-PET scanner: left - 1 layer, L = 50 cm; middle - 2 layers, L = 50 cm; right - 1 layer, L = 200 cm.

depends on the diameter of the scanner and is calculated as the number of edges of the regular polygon circumscribed around the ring with the radius D/2[2] (see Tab. 3.1).

Thickness T [mm]	**Diameter D [cm]**		
	75	**85**	**95**
4	590	668	746
7	336	382	426

TABLE 3.1: Number of strips in a single layer of the detecting chamber of the J-PET scanner as a function of the thickness of the strip and the diameter of the chamber

In case of the Modular J-PET tomograph, scintillator strips were grouped into cuboidal modules. The Modular J-PET scanner was simulated for the fixed inner diameter of 76.4 cm, for 6 lengths of the strips (20 cm, 50 cm, 100 cm, 120 cm, 150 cm and 200 cm) and for single- and double-layer setups (it consisted of 24 or 48 modules). Each module consisted of 13 scintillator strips. Distance between adjacent strips was 1 mm. In case of double-layer geometries, the distance between the first and the second layer was 5 mm. Visualisation of a single module is presented in Fig. 2.8 (previous chapter), while visualisation of example geometries based on such modules are presented in Fig. 3.3. Fig. 3.5 also shows how the WLS layer was simulated - as the cuboid plate with thickness of 3 mm placed between two layers of modules (the WLS detectors are marked with green color).

Finally, the prototype 192-strip geometry was simulated. Visualisation of the prototype geometry simulated in the GATE software is presented in Fig. 3.4.

[2]The number of edges of the regular n-sided polygon circumscribed around the ring with the radius D/2 is $n = \frac{\pi}{\text{arc tg}\left(\frac{a}{D}\right)}$, where a is the length of the side of the polygon (in this case, the thickness of the scintillator).

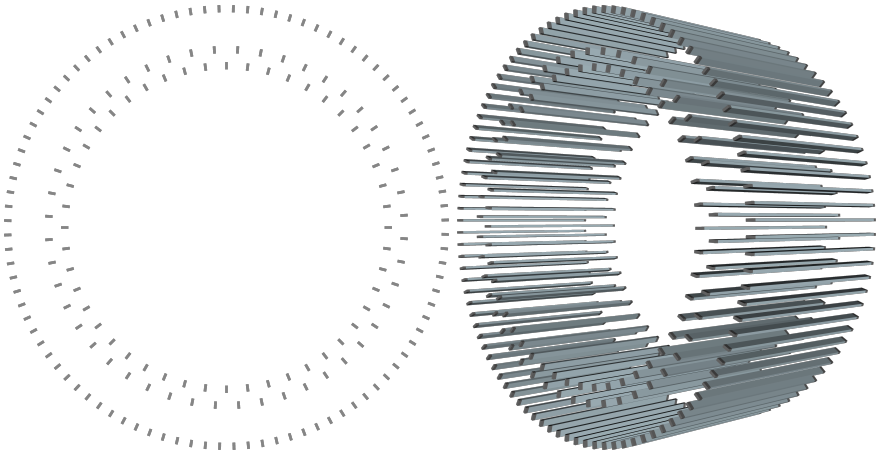

FIGURE 3.4: Geometries of the J-PET prototype simulated in the GATE software

3.1.2 Material and readout properties

In order to reflect actual properties of simulated tomographs, material and readout properties were implemented within the GATE software. The GATE user may specify material properties in 3 files: *GateMaterials.db*, *Materials.xml* and *Surfaces.xml*. The first one contains some basic information about the material, like atomic composition, density and state. In fact, implementing these base properties is enough for most of simulations. The second file is used to define properties needed to perform simulations of light propagation in scintillating materials. In the last one, properties of the surfaces may be defined (surfaces connecting volumes with different properties, like the surface between the scintillator and the photomultiplier).

Optical properties of EJ230 scintillating material and photomultipliers were implemented within the GATE software and used for simulations of optical photons inside the single 50 cm scintillator strip. These simulations were performed to improve methods of reconstruction of place of scintillation along the scintillator. Simulations including propagation of light photons are relatively slow due to a large number of optical photons generated in each scintillation. For example, if energy of 200 keV was deposited, about 1940 optical photons were emitted ($0.2\ MeV \cdot 9700\ \frac{1}{MeV}$). Because of that, in simulations described in further chapters only interactions of gamma photons were taken into account and optical photons were switched off. However, to reflect optical properties of the scintillator and different types of readout, results of these simulations were smeared with experimental resolutions. Light propagation may be replaced with the smearing of position and time of a hit due to a fact that if optical photons would be even propagated

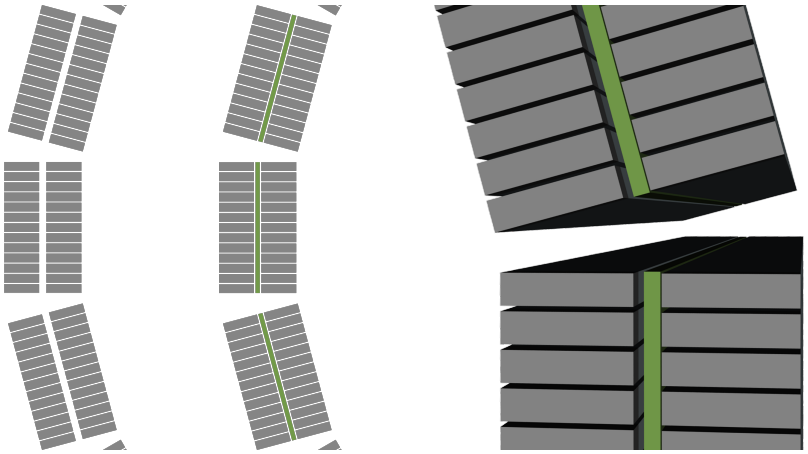

FIGURE 3.5: Details of example geometries of the Modular J-PET scanner without and with the WLS strips

and readout signals would be formed from them, then the hit details could be achieved only with a fixed maximum resolution. This resolution is limited by the method used to reconstruct the position and time of a hit along the strip, shape of the strip, material used and properties of the readout. Instead simulating all optical photons, the smearing may be applied to save the resources during simulation and time of post processing. Details concerning smearing with experimental resolutions may be found in App. C.

Following readouts were taken into account: R4998 vacuum tube photomultipliers (PMT), silicon photomultipliers matrices (SiPM) and SiPMs combined with an additional wavelength shifters (WLS) layer [48]. Each SiPM consisted of 10 AD8001 silicon photomultipliers arranged in 2 columns and 5 rows. The WLS strips were arranged perpendicularly to the scintillator strips allowing for the determination of the gamma photon interaction point along the tomograph axis based on the distribution of amplitudes of light signals in the WLS strips [48] (Fig. 3.5). An analogical solution was proposed for the AX-PET detector [70–72].

To smear the time of detection and spatial resolution along the scintillator strip, coincidence resolving time (CRT) was used. CRT is defined as a FWHM of the distribution of TOF. It depends on the shape and material properties of the scintillator strip and also on properties of the readout used. Using CRT, axial spatial resolution may be calculated as a $FWHM(z) = \frac{CRT \cdot c_{scin}}{\sqrt{2}}$, where c_{scin} is the group velocity of the light signal along the strip and is equal to about 12.6 $\frac{cm}{ns}$.

The used values of CRT and axial resolution as a function of the tomograph length L are shown in Fig. 3.6. The values of CRT and FWHM (in z coordinate) for PMTs and SiPMs were estimated based on simulations presented in Ref. [9] tuned to the empirical results for the single- and double-strip J-PET prototypes [21, 22]. The FWHM with the additional layer of the WLS strips was measured with the test setup described recently in the article [48]. The values indicated as WLS-2 show resolution achieved in the first test [48]. However, since the system was not fully optimized, there is still room for significant improvement indicated in Fig. 3.6 as WLS-1 by better matching between the emission spectrum of the scintillator and the absorption spectrum of the WLS and more efficient photon readout. In the test, only half of the WLS surface was covered by the SiPM.

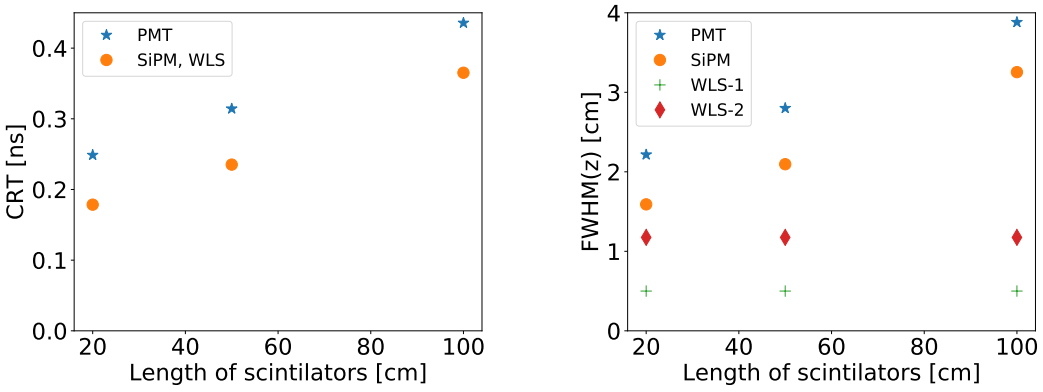

FIGURE 3.6: Values of CRT (left) and axial resolution (right), used for the simulations, as a function of the length of the scintillator, shown for different readouts [9, 48]. More details in the text.

3.1.3 Sources and phantoms

Sources of radiation or radioactive nuclei are only defined by their geometry and the properties of emitted radiation (energies, angular distributions, intensities, etc.) and are not themselves simulated in GATE. Two types of sources were used during the studies presented in this thesis: the back-to-back gamma source and the ion source for simulating the ^{22}Na isotope. For simplification, all sources emitted radiation isotropically and had activities constant in time. They could have different shapes - from points and 2-dimensional surfaces to the 3-dimensional shapes. Also, when phantom was simulated, the volume of the source was simulated as overlapping with the volume for the phantom either to imitate a human patient or other spatially extended phantom filled with active material.

There are two types of phantoms in GATE: voxel and analytical ones, i.e. with geometry defined analytically. In case of performance studies presented in following chapters, the analytical phantoms were used (NECR/SF phantom and IQ phantom). However, also the voxel 4D XCAT phantom [73] may be implemented in the toolkit.

3.1.4 Physical processes

Simulations were performed using the list of physical processes called *emlivermore_polar* that implements the low-energy Livermore model for electromagnetic processes [74, 75]. The low-energy Livermore model is designed for applications that require high accuracy of electrons, hadrons and ion tracking without magnetic field. The low-energy processes are the photo-electric effect, Compton scattering, Rayleigh scattering, gamma conversion, bremsstrahlung and ionisation. Also fluorescence and polarization of gamma photons are taken into account. These processes rely on shell cross sections data [74] in contrast to high energy processes that often use only parametrizations of these data. The data used for the determination of cross-sections and for sampling of the final state are extracted from the following publicly distributed evaluated data libraries: EPDL97, EPICS2014, EEDL, EADL and binding energy values based on data of Scofield.

The implementation of low-energy processes is valid for elements with atomic number between 1 and 99, and for energies down to 10 eV, upper limit depends on the process. This range of energies is sufficient for the purpose of the J-PET simulations due to the low-energy cut on 10 keV. Energy thresholds and other selection criteria used in the analysis are described in the following section.

3.2 Analysis of the GATE output

The GATE output is analyzed with the GATE Output J-PET Analyzer (GOJA) software elaborated by the author of this thesis (see App. B). GOJA implements the event selection method, which is described below.

3.2.1 Event selection method

As it was explained in section 1.4, a coincidence is a set of hits detected within the fixed time coincidence window. Among all coincidences, there are true and false ones. False coincidences may be grouped into detector-scattered, phantom-scattered and accidental ones. In order to extract true coincidences from the set of all coincidences and to minimize the background from the false ones, a two-level selection procedure is performed.

At the first level, only events with exactly two interactions registered with energy loss larger than 200 keV each and any number of interactions with smaller energy loss are accepted (value of 200 keV is explained in Sec. 7.2.1). We accept events with more than two scatterings in order to avoid rejection of such events as shown in Fig. 3.7a, which can be classified as true coincidences. However, these conditions accept some background events e.g. in Fig. 3.7b and 3.7c. Yet, the requirement of at least two interactions with energy loss above the 200 keV threshold reduces the contribution from coincidences of the type shown in Fig. 3.7c to a negligible level. This is because the 511 keV gamma photon cannot deposit more than 184 keV in more than one scattering [76] (see Sec. 7.2.1).

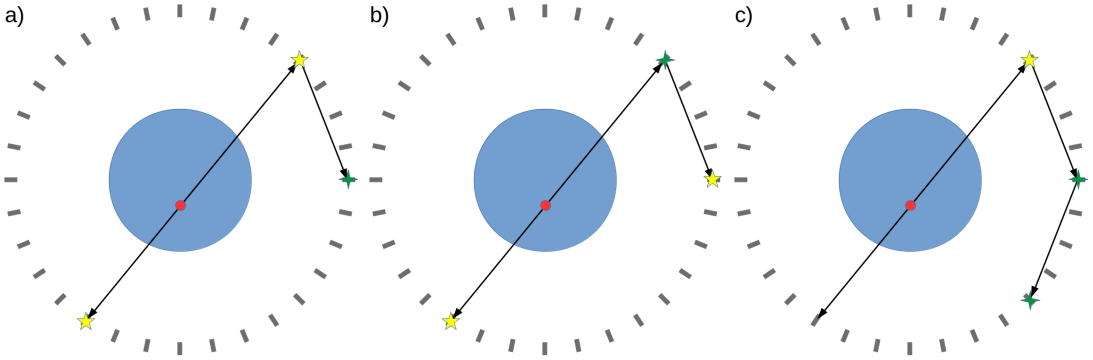

FIGURE 3.7: Exemplary events with three depositions of energy above the noise threshold: a) true coincidence, b) and c) detector-scattered coincidences. Yellow 5-arm stars visualize depositions of energy bigger than the fixed energy threshold (200 keV) and the green 4-arm stars – below 200 keV.

At the second level of event selection method, an event-by-event information about times and azimuthal angles[3] of interactions is used. Selection criterion was determined using simulation with the cylindrical phantom (NEMA scatter phantom, see 5.1.4) and the linear source placed at the radial distance of 25 cm from the axis of the scanner [76] and then used for all other simulations. The source was a 70-cm-long rod with a diameter of

[3] The azimuthal angle is the central angle in the plane perpendicular to the axis of the scanner. In Fig. 3.8 the azimuthal angle of the scintillator A would be ACE.

1.6 mm and activity of 1 MBq. The simulated geometry was the single-layer 384-strip detector with 50-cm-long and 7 mm thick strips and the diameter of 85 cm. Results of such simulation may be used to estimate scattering rejection criteria for big objects with diameters of about 50 cm (for example human body). These results are presented in Figs 3.9 and 3.10.

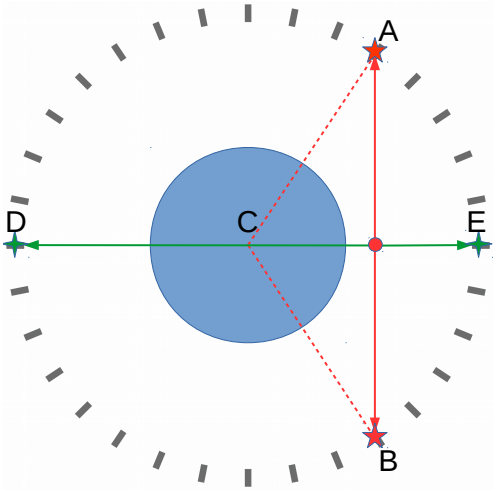

FIGURE 3.8: Schematic cross-section of one layer of the tomograph with cylindrical phantom (large blue circle) and the source (red dot). Two extreme cases explaining the structures seen in Fig. 3.9 are indicated. For the LOR passing through the centre of the tomograph (green arrows), the relative angle between strips is equal to 180° (angle DCE) and the hit time difference is equal to $\frac{50\ cm}{c} \approx 1.5\ ns$. In another extreme case (red arrows) the time difference between hits is equal to zero (paths of two gamma photons are equal) and the difference of angles between two red dotted lines is equal to about 115° (angle ACB), as illustrated in the figure.

The simulation showed that true coincidences lie in a well-defined region in the space spanned by the times and azimuthal angles differences above the red line[4] shown in Fig. 3.9.

For both phantom-scattered and detector-scattered coincidences, there are longitudinal structures visible in the space spanned by the time and azimuthal angle differences. These structures were discussed in details in Refs [77] and [76]. However, for consistency, the discussion is also shortly presented in below paragraphs.

In case of phantom-scattered coincidences, for fixed energy threshold set to 50 keV, there are three structures visible (Fig. 3.9, 2nd row). The first one is stretched between

[4] The red line is the ellipse with vertex at (2.2 ns, 180°), co-vertex at (0 ns, 80°) and center at (0 ns, 180°). The choice is based on results of simulations shown in Fig. 3.9. The choice of the red-line criterion is rather conservative and leaves room for further reduction of false coincidences in case of smaller objects imaging.

points (1.5 ns, 0°) and (2 ns, 180°). This structure contains coincidences, in which one of gamma photons was scattered in phantom at least once. Because of the scattering, the gamma photon changed direction and after that both photons were properly detected without any additional secondary scatterings. Ellipsoidal structure over the red line contains coincidences in which one of gamma photons was scattered in phantom but the energy deposited was so small so the photon did not change its direction (or it changed the direction slightly). Because of that, although it is a phantom-scattered coincidence, it has features of true coincidence. The third structure stretched between points (0 ns, 0°) and (3 ns, 180°) contains coincidences in which at least one phantom-scattered photon is additionally scattered in the detector. After applying 200 keV fixed energy threshold, most of phantom-scattered coincidences (especially those that are also detector-scattered) is removed from the coincidences dataset.

In case of detector-scattered coincidences, for fixed energy threshold set to 50 keV, there are two structures visible (Fig. 3.9, 3rd row). The structure stretched between points (0 ns, 0°) and (3 ns, 180°) contains coincidences in which at least one gamma photon was scattered in the detector and there were no secondary scatterings in the phantom. The larger is the angle of the primary scattered photon, the larger are time and azimuthal angle differences. For example, the bin with coordinates (2.9 ns, 180°) corresponds to the backscattering - primary particle is backscattered and it is registered in the strip on the opposite side of the detector (2.9 ns is the time needed by the photon to travel between opposite strips with speed of light in vacuum). Ellipsoidal structure over the red line contains coincidences in which at least one of gamma photons was scattered two times in the detector but the distance between the scatterings was very small (both primary and secondary scatterings happened in the same or in neighbour strips). After applying fixed energy threshold of 200 keV, most of detector-scattered coincidences is removed from the coincidences dataset.

Finally, applying ellipsoidal criterion limits also accidental coincidences. However, number of accidental coincidences is higher for 200 keV fixed energy threshold than for 50 keV fixed energy threshold for the same simulation output. It is due to the fact that for lower threshold, there are more events in which there are more than 2 hits with deposited energy exceeding the threshold. Because of that such events are not taken for further analysis. Fig. 3.10 highlights that applying both levels of event selection method maximizes the number of true coincidences and minimizes the scattered ones.

Efficiency of the second level of selection method depends on the simulation type and the source activity. For the simulation with rod source placed 25 cm off from the axis of the scanner, the percentage of rejected events (reduction factor with respect to the first level of selection) was 2.3%. In case of spatial resolution simulations (section 5.2.3) the reduction was 0.5%. For the NECR simulations (section 5.2.4), the reduction was between 0.5% for small activity concentrations and about 70% for the highest activity concentrations (about 90 kBq/cm^3), which shows that the higher the activity, the more important the reduction provided by the second level of event selection method (Figs 3.11-3.12). The chosen selection criterion may be also adjusted to the size of the investigated object and to the geometry of the detecting chamber.

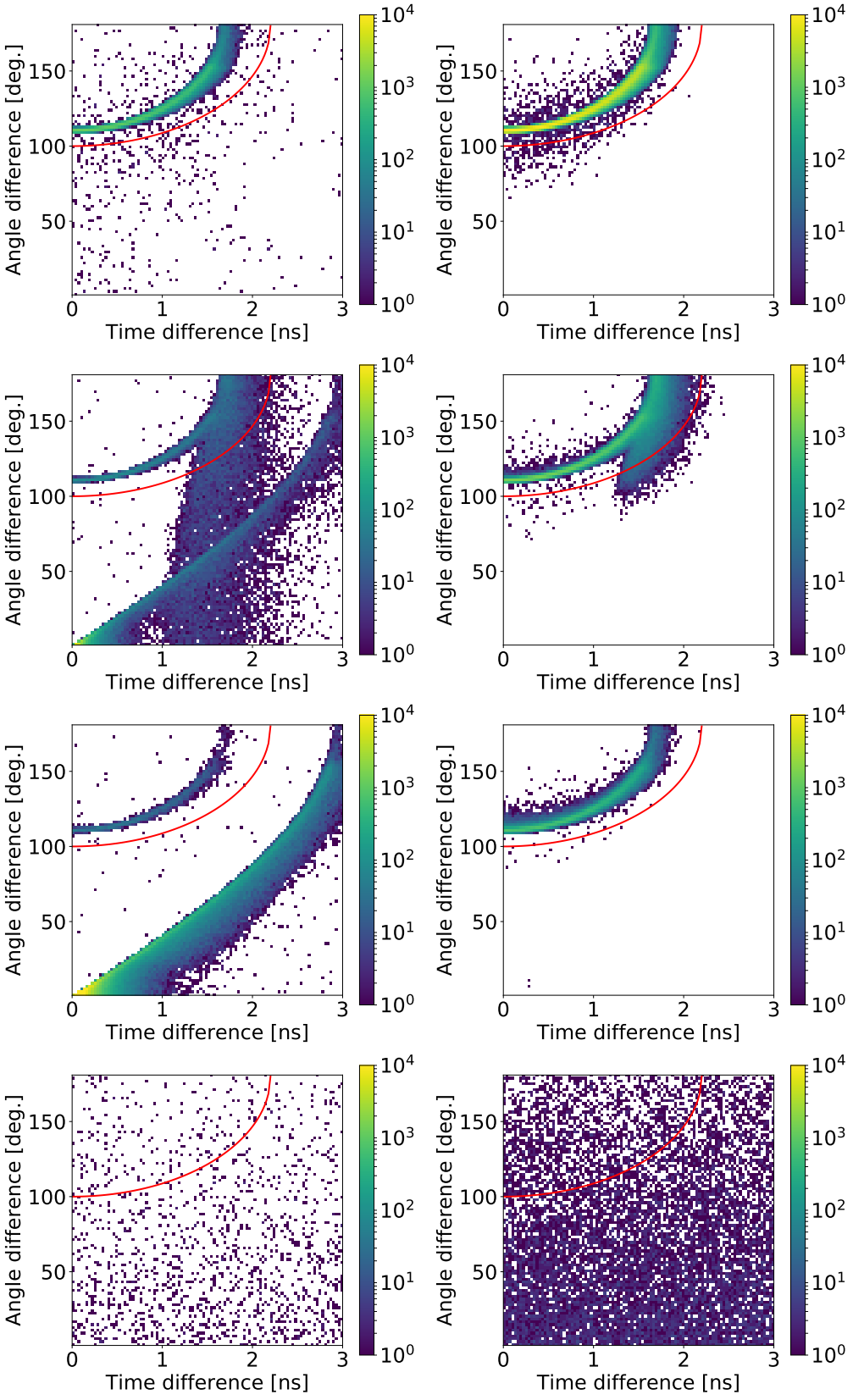

FIGURE 3.9: 2-dimensional histograms of time and central angle differences of subsequent hits in each coincidence; histograms in each column sum up to 1 mln coincidences; (left) 50 keV fixed energy threshold, (right) 200 keV fixed energy threshold. In next rows there are coincidences classified as (top) true, (2nd row) phantom-scattered, (3rd row) detector-scattered and (bottom) accidental. Structures visible in histograms are explained in text.

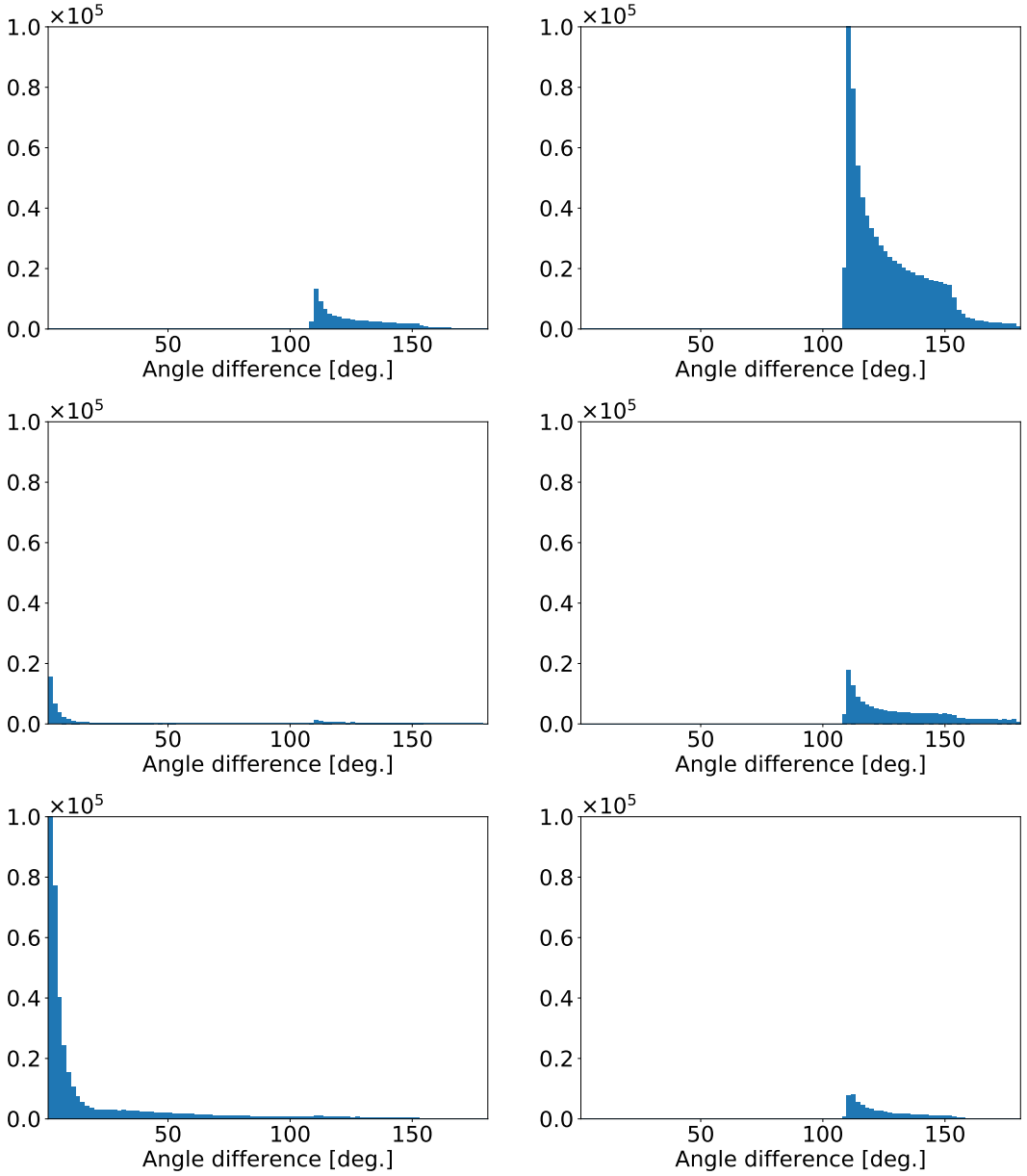

FIGURE 3.10: Angular projections of 2-dimensional histograms presented in Fig. 3.9. In next rows there are coincidences classified as (top) true, (middle) phantom-scattered and (bottom) detector-scattered. Applying 200 keV fixed energy threshold maximizes true coincidences and minimizes scattered ones.

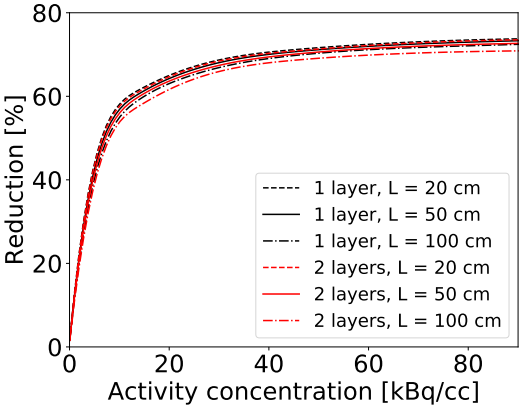

FIGURE 3.11: Reduction of number of events provided by the second level of event selection method for different geometries of the J-PET scanner

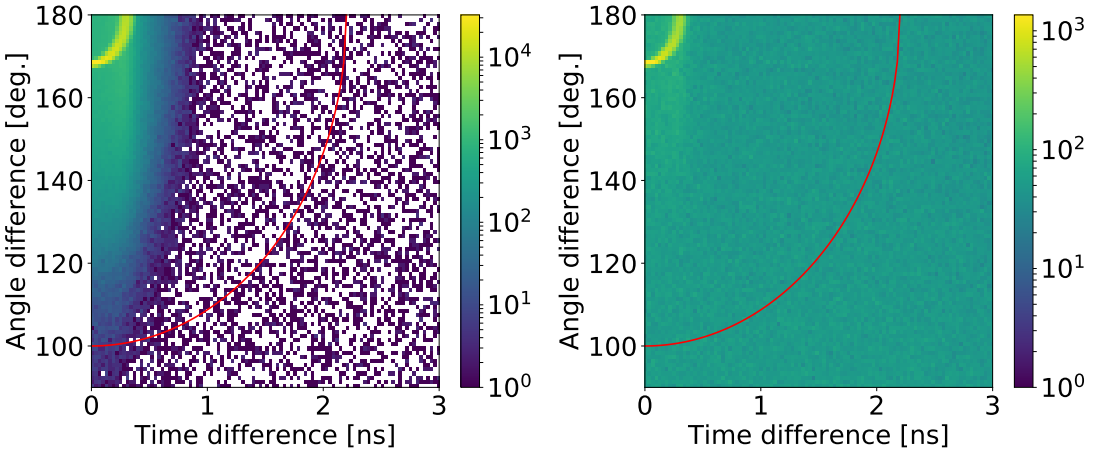

FIGURE 3.12: Results of the NECR characteristic simulation for the geometry with 50-cm-long scintillating strips visualized in the form of scatter plots of angle differences vs. time differences. The source was the 70-cm-long rod placed axially inside the scatter phantom at distance of 4.5 cm from the axis of the tomograph. Left panel shows result of simulation for small activity of 45 Bq/cm^3 and right panel for high activity of 90.9 kBq/cm^3. The second level selection criterion, indicated as the red line, reduces the number of events by a factor of 0.5% to 70% for the left and right panel, respectively.

Chapter 4

Verification of simulations using experimental data

In this chapter, the GATE simulations are verified with experimental data. Measurements of the J-PET "big barrel" prototype (see Sec. 2.2.1) were collected during time periods adjusted to lifetimes and availability of sources. Until June 2019 there were 8 measurement campaigns, called "runs". In the verification process, part of data obtained for the prototype during the 4th run were used [78]. This data were collected on 25th August of 2017.

4.1 Experimental data

Measurements chosen for the verification process were performed using 6 pointlike sources and they were inspired by the NEMA spatial resolution norm (see Chap. 5). Sources were placed in positions suggested in the norm but they differed with properties. Also the method of measurement was modified. While in the norm it is suggested to measure fluorine ^{18}F source subsequently in each of 6 positions, in the experiment 6 sodium ^{22}Na pointlike sources with different activities were measured at the same time (see Tab. 4.1). Such measurements were performed not to calculate the final NEMA spatial resolution of the scanner but to check the response of the device to sources consisting of few smaller pointlike sources. Also the methods of image reconstruction could be adjusted and tested

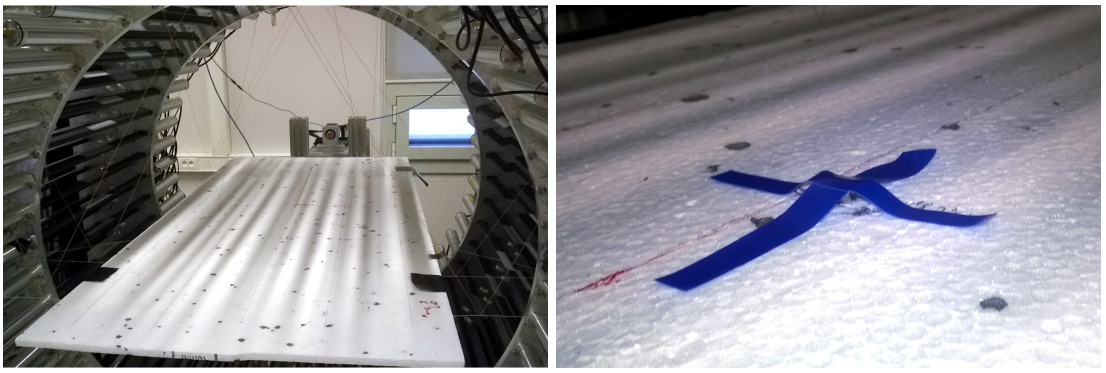

FIGURE 4.1: Measurement setup: pointlike sodium sources were placed on the styrofoam panel hanged using threads in the central position of the detecting chamber.

with these data, while in case of single pointlike source such studies could be biased with the simplicity of the source.

Source	**Position [cm]**	**Activity [kBq]**
37/12	(0,1,0)	204
39/12	(0,10,0)	207
UR450	(0,20,0)	1134
UR451	(0,1,-18.75)	1131
K4-390	(0,10,-18.75)	6198
L2-295	(0,20,-18.75)	7601

TABLE 4.1: Sources used in the measurements; the first column is the serial number of the source, second shows its position in reference to the centre of the detecting chamber and third indicates its activity.

The advantage of sodium over fluorine is its long halftime period of about 2.5 years and commercial accessibility. However, sodium emits also the gamma photon with energy 1275 keV from neon deexcitation and therefore some additional cuts in data processing were needed in order to minimize the background. The setup of the experiment is shown in Fig. 4.1. Sources were attached to the styrofoam panel using an adhesive tape. The panel was hanged using threads inside the central position of the detecting chamber.

Before the target measurements, some additional measurements and procedures were performed to synchronize and calibrate the detector. Firstly, synchronization of thresholds was processed using measurements of the annihilation chamber. Power supply voltages of photomultipliers were set to such values to give uniform response from all detector modules. Secondly, thresholds were calibrated in order to get uniform response from all channels. After that, the velocity calibration was performed using the collimator. Velocity calibration is needed because speed of light in a scintillator varies slightly between

different scintillators. Knowing the speed of light in each scintillator, a correction may be made during the data analysis. Finally, time calibration [79, 80] was performed using the reference detector. At this stage, strips were irradiated in their centers and time differences between two sides of each detector were measured. If the time difference was different than zero, the correction was applied. When the synchronization and calibration procedures were finished, target measurements with 6 sources were performed. Data collection was controlled using the remote connection. Compressed data files (711 files, each with size of 1 GB) were stored to the server for the offline analysis.

During the offline analysis, data were decompressed and processed with the *JPetFramework*[1] toolkit [43, 44]. Firstly, signals from time-to-digital converters (TDC) were used to reconstruct signals of single-photon scatterings (hits). After that, pairs of hits fitting in a fixed time window were combined to form coincidence events.

For verification, it was assumed, that the time window was 5 ns and there were exactly 2 hits with the deposited energy bigger than 200 keV and smaller than 341 keV and any number of scatterings with deposited energies smaller than 200 keV. Any event that contained the hit with deposited energy bigger than 341 keV was removed from the analyzed data set. The calibration curve (Eq. 2.2) was used to calculate the deposited energies needed for the data selection. Histograms of TOTs and deposited energies for 10 mln hits are presented in Fig. 4.2. Described selection provided about 42 mln coincidences.

After the coincidences selection, obtained data was used to plot 2-dimensional histograms of time and central angle differences of subsequent hits in each coincidence (Fig. 4.3 - top panel). Also the 1-dimensional projections were drawn (Fig. 4.3 - bottom panel). Structures visible in these figures are explained in next section with the help of results of simulations.

[1] `https://github.com/JPETTomography/j-pet-framework-examples.git`, commit 0f9a7d7

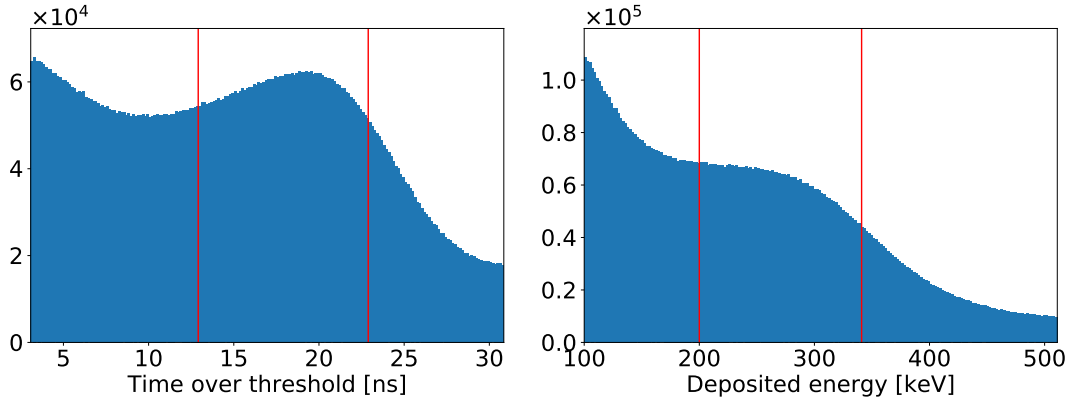

FIGURE 4.2: (left) Histogram of TOTs – values of cuts marked with red vertical lines: min = 12.91 ns, max = 22.89 ns. (right) Histogram of energies deposited – values of cuts marked with red vertical lines: min = 200 keV, max = 341 keV. Both histograms were drawn for 10 mln hits. The lower limit of each histogram is derived from the limit of the energy calibration method (the method was verified in range 100-950 keV, see Sec. 2.1).

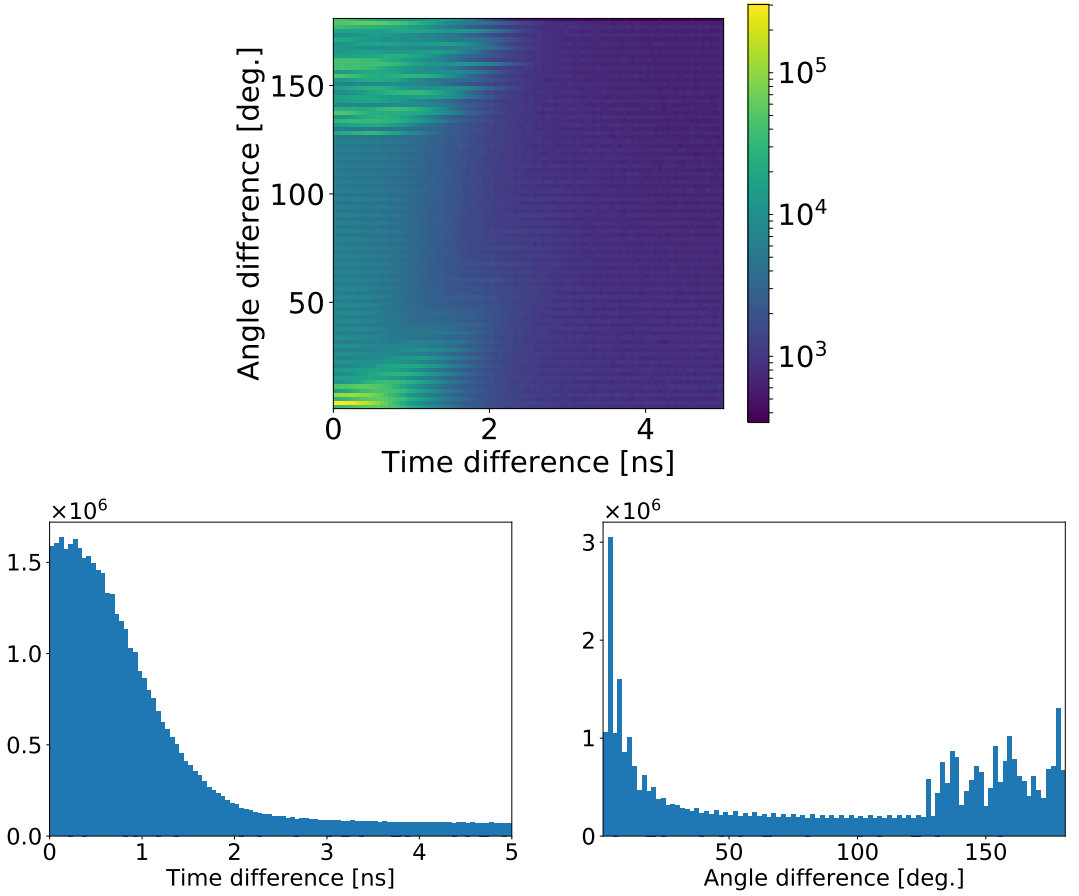

FIGURE 4.3: (top) 2-dimensional histogram of time and central angle differences of subsequent hits in each coincidence; for higher contrast the colorbar starts from minimum histogram value. (bottom) 1-dimensional projections of the top histogram of time and central angle differences for all coincidences collected from the experimental data set.

4.2 Simulations

The experiment was simulated using GATE package. Six sources of radiation were implemented as spheres with radiuses of 0.5 mm each. Their activities and positions were set to values from Tab. 4.1. Two scenarios were simulated: a) non-material back-to-back gamma sources, b) sodium ion sources. Results of simulations were processed using the GOJA software (see App. B) to obtain sets of coincidences. Coordinates x and y were aligned to strips centers, while z coordinates and times were smeared with experimental resolutions (see App. C). Histograms of time and central angle differences for coinciding hits are presented in Figs 4.4 and 4.5.

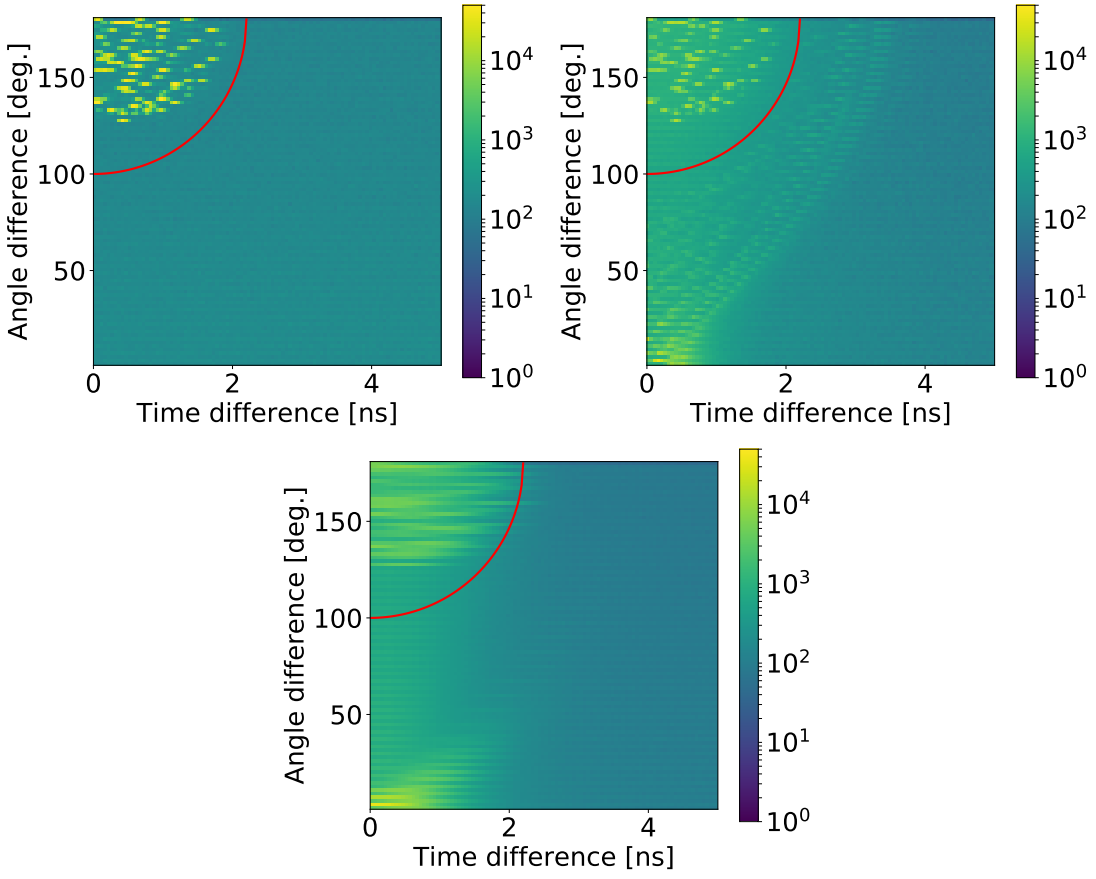

FIGURE 4.4: 2-dimensional histograms of time and central angle differences of subsequent hits in each coincidence; 5 mln of coincidences in each histogram; (top left) unsmeared simulated gamma back-to-back source, (top right) unsmeared simulated ion source, (bottom) experimental data (histogram presented in Fig. 4.3 rescaled to sum up to 5 mln coincidences); the selection criterion marked with the red line was described in details in Sec. 3.2.1.

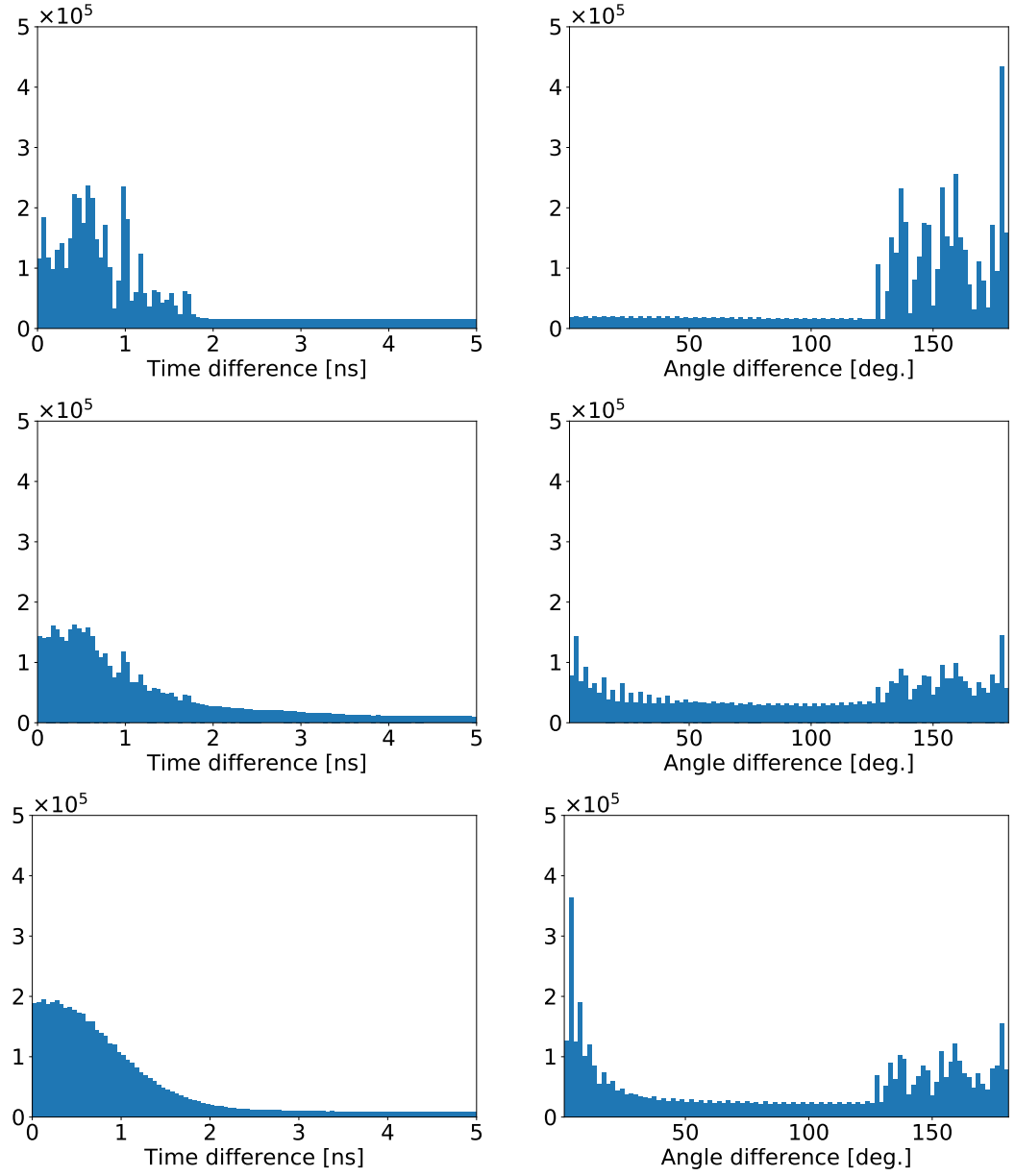

FIGURE 4.5: 1-dimensional projections of histograms presented in Fig. 4.4; histograms of (left) time and (right) central angle differences of subsequent hits in each coincidence; 5 mln coincidences in each histogram; (top) simulated gamma source, (middle) simulated ion source, (bottom) experimental data.

In order to compare the simulations with these two types of sources with the experiment, additional histograms of coincidences grouped by their types (true, detector-scattered, accidental) were drawn (Fig. 4.6). For the back-to-back gamma sources, most of the coincidences classified as the true ones are in the region above the selection criterion (Sec. 3.2.1). Also the detector-scattered coincidences are located above the selection criterion but there are far fewer of them. In case of the ion sources, both true and detector-scattered coincidences are spilled out in much broader region but most of true coincidences is located in the region above the selection criterion. True coincidences outside this region may originate from annihilations in the detector, not in the sources. As the sources are relatively small, some positrons get out of them and annihilate in the detector - because of that there are true coincidences located below the selection criterion with properties of the detector-scattered ones. For both types of sources, the accidental coincidences are spread uniformly in the space of time and central angle differences.

While in case of the simulation with the back-to-back gamma sources, the second level selection criterion reduces the number of all events by 27.8 %, in case of the ion sources it reduces the number of all events by 62.9 %. Among the selected coincidences (above the selection criterion) there were accordingly: 88.6 % of true, 5.4 % of detector-scattered and 6.0 % of accidental coincidences for the back-to-back gamma sources; 73.6 % of true, 19.3 % of detector-scattered and 7.1 % of accidental coincidences for the ion sources.

Till now, exact unsmeared simulated coordinates and times were taken for calculating presented histograms. However, the experimental results are naturally smeared. Because of that also the results of simulations were smeared. While the measurements were taken for the classical photomultipliers (PMT) readout also smearings for two other experimental resolutions were performed. The results are presented in Fig. 4.7. The simulation of ion sources with the PMT readout seems to be the most consistent with the experiment (see also Figs 4.4 and 4.5). On the other hand, in next prototypes, where the readout combined of silicon photomultipliers and the WLS shifters will be used, it will be possible to achieve results similar to the ones from the bottom row of Fig. 4.7.

Finally, only the coincidences over the selection criterion for both types of sources and with the PMT readout were histogrammed and drawn as 2- and 1-dimensional histograms (Figs 4.8-4.9). The histograms were rescaled to sum up to 1 mln coincidences. Although it seems that higher compatibility was obtained for the simulation with ion

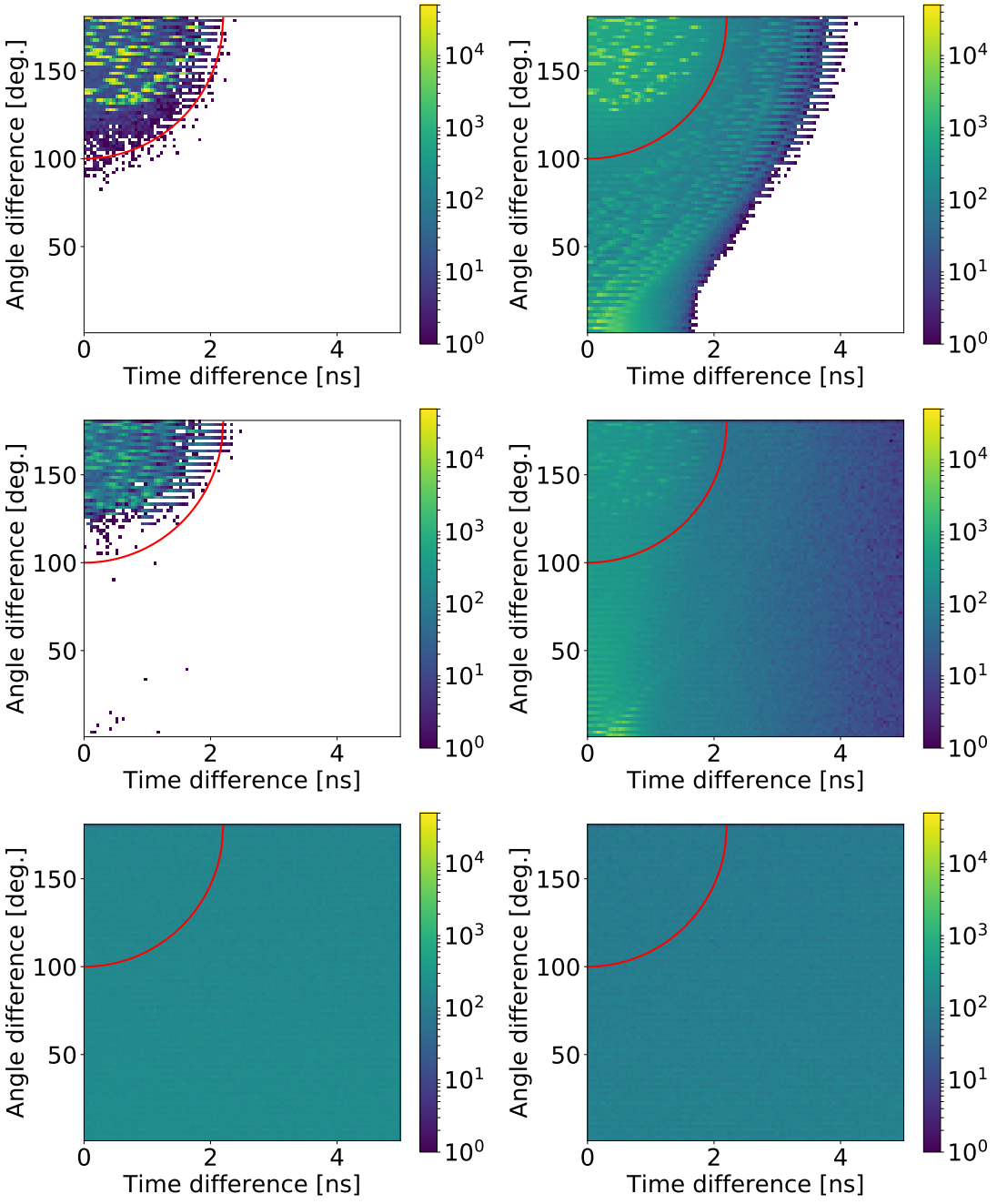

FIGURE 4.6: 2-dimensional histograms of time and central angle differences of subsequent hits in each coincidence; histograms in each column sum up to 5 mln coincidences; (left) simulated gamma back-to-back source, (right) simulated ion source. In next rows there are coincidences classified as (top) true, (middle) detector-scattered and (bottom) accidental. There are no phantom-scattered coincidences because there was no phantom in the simulations.

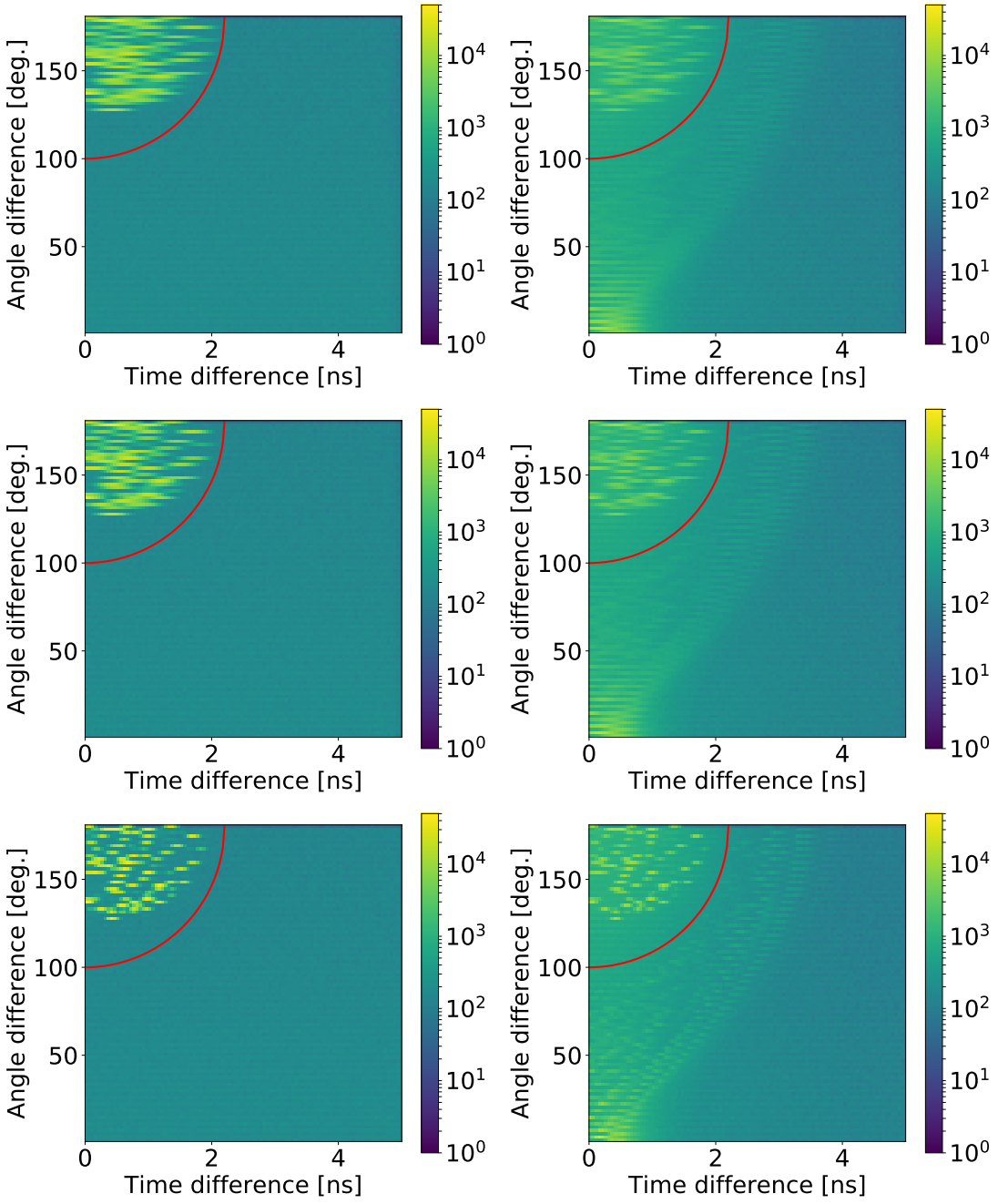

FIGURE 4.7: 2-dimensional histograms of time and central angle differences of subsequent hits in each coincidence; 5 mln coincidences in each histogram; (left) simulated gamma back-to-back source, (right) simulated ion source; (top) PMT readout, (middle) Si readout, (bottom) Si+WLS readout.

sources, for both simulations there is a satisfactory compatibility of simulation and experiment in both time and central angle differences spaces.

Peaks in the angle difference histograms are for the same differences. While for the ion sources, their amplitudes are nearly identical, for back-to-back gamma sources peaks seem to be much sharper. It is due to a much lower background level for this type of source and scaling a sum of histogram to a fixed value. As it was explained above, higher background level for the ion sources is caused by the fact that some positrons annihilate in the detector, not in the sources, which leads to overestimating true and detector-scattered coincidences. Additionally, sodium source emits additional gamma photon from neon deexcitation, which increases the accidental coincidences. In the time differences domain, there is a higher compatibility for the ion sources. However, it seems that also in this case the smearing is underestimated (in relation to obtained experimental histogram).

In this chapter the simulation methodology was verified using the example of simulations of one of measurement campaigns of the "big barrel" J-PET scanner. It was shown, that for the ion gamma sources and smearing data with the experimental resolutions, the compatibility is not only qualitative, but also quantitative. However, in further simulations only back-to-back gamma sources will be taken into account. Usage of these sources lowers the background level and simplifies the analysis of results, which makes it easier to understand properties of the prototype detector. Back-to-back gamma sources do not introduce additional gamma photons from the neon deexcitation, which makes simulations with them more adequate to measurements with the fluorine sources, used commonly for obtaining characteristics of the PET scanners. It is also worth to mention, that simulations with back-to-back gamma sources are much less computationally complex than the ones with the ion sources and because of that they are much more efficient. Both processor time and disk space are saved when these simplified sources are used.

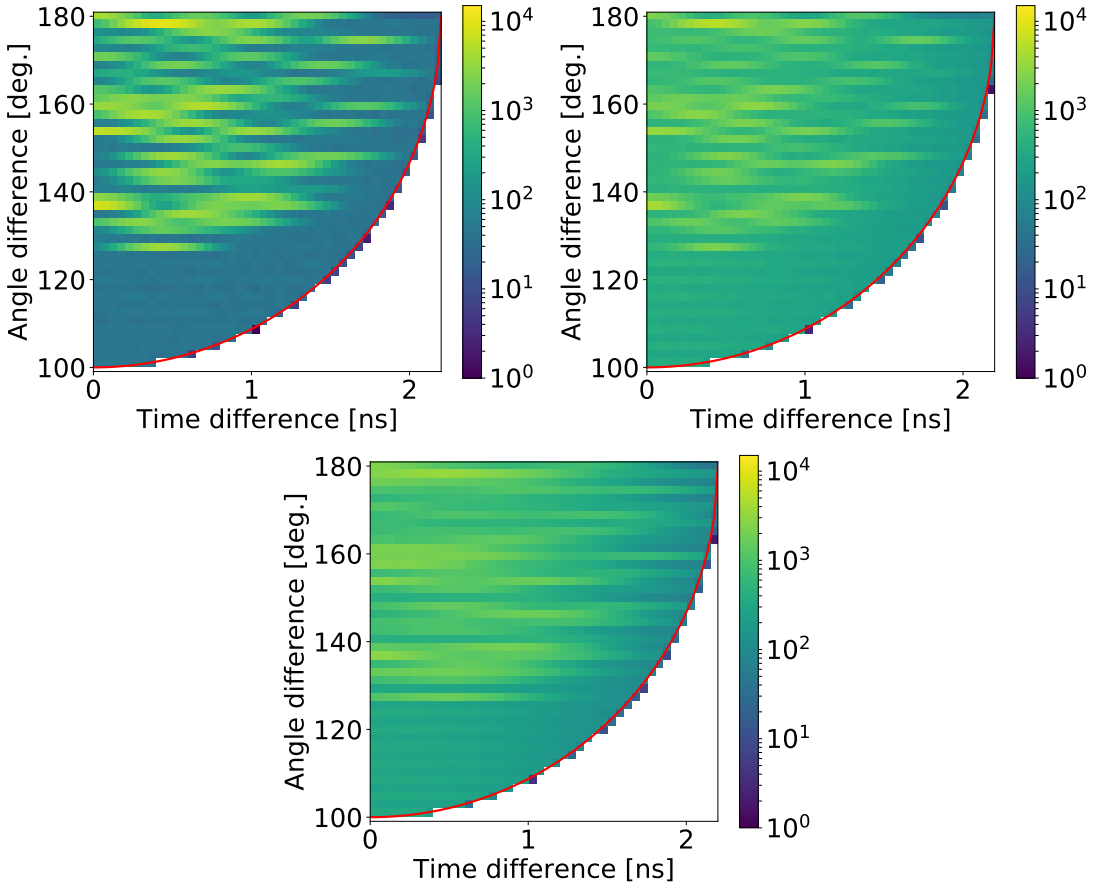

FIGURE 4.8: 2-dimensional histograms of time and central angle differences of subsequent hits in each coincidence; 1 mln of coincidences in each histogram; (top left) simulated back-to-back gamma source, (top right) simulated ion source, (bottom) experimental data.

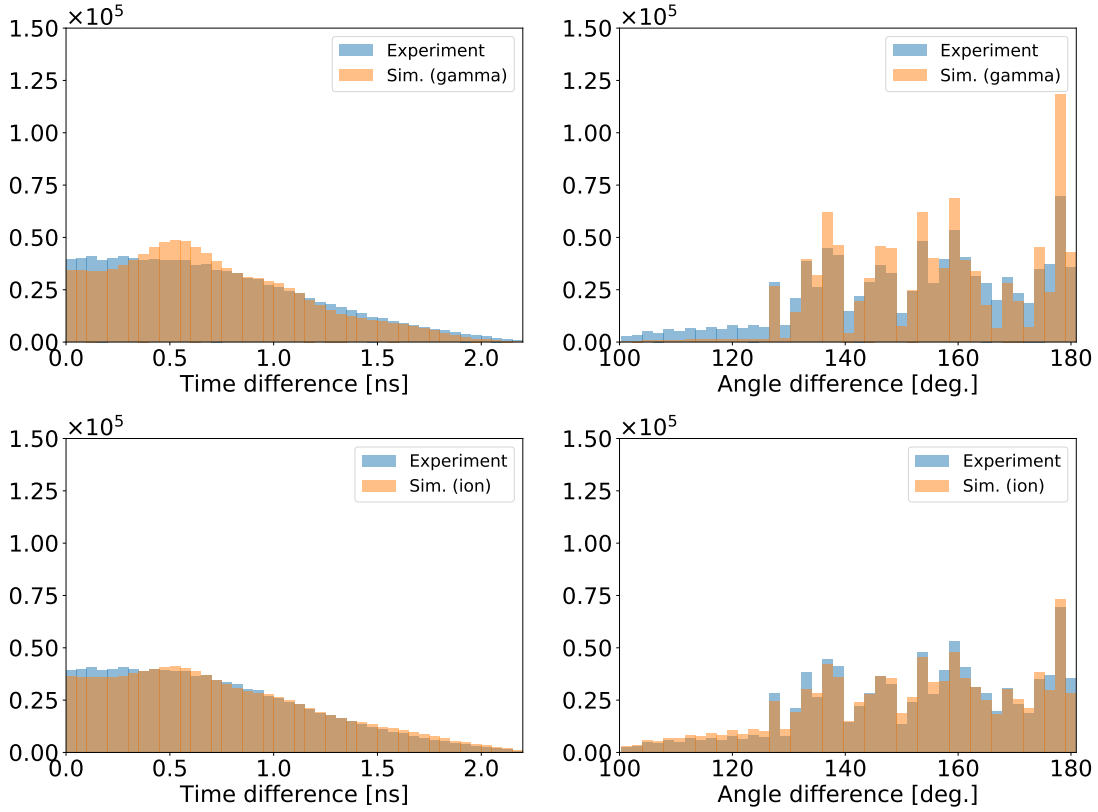

FIGURE 4.9: Histograms of (left) time and (right) central angle differences of subsequent hits in each coincidence; all histograms are normalized to 1 mln coincidences; (top) experimental data vs. simulated back-to-back gamma sources, (bottom) - experimental data vs. simulated ion sources.

Chapter 5

Performance characteristics of the J-PET detector

The National Electrical Manufacturers Association (NEMA) is the association of electrical equipment and medical imaging manufacturers in the United States, which publishes standards for medical diagnostic imaging equipment. One of its standards is NEMA-NU-2 [81], for the Positron Emission Tomography (PET) devices. It defines a set of comprehensive characteristics of PET scanners: spatial resolution, scatter fraction, noise equivalent count rate (NECR) [82], sensitivity and image quality. These characteristics allow to compare different PET tomographs and are required worldwide for any such equipment intended for real medical usage.

Performance characteristics of the prototype PET scanner may be obtained using GATE Monte Carlo simulations. While the NEMA norms are the standard, also the maps of efficiency of the J-PET scanner were calculated as the extension of the sensitivity norm. In case of the NEMA norms, the GATE software was used to simulate a set of tomograph geometries with back-to-back gamma sources (defined by the points of the electron-positron annihilations), corresponding to sources defined in the NEMA norm. The following NEMA characteristics were obtained from simulated data: spatial resolution, scatter fraction, NECR and sensitivity. For maps of efficiency, planar 2-dimensional sources were used. Some results presented in this chapter, concerning both maps of efficiency and the NEMA characteristics, were already published in Refs [76, 77, 83–85].

In case of the sensitivity, scatter fraction and NECR not only standard sources and phantoms were simulated but also sources and phantoms extended to 200 cm were taken into account (in comparison to 70-cm-long in standard). It is due to a long AFOV of tested geometries that is up to 2 m. Simulations may be taken into account in discussion on the future form of the NEMA-NU-2 norm, to describe total-body scanners in a more comprehensive way. Detailed version of these studies is described in a new publication, which is currently under preparation.

5.1 Materials and methods

In this section, algorithms for obtaining the above-mentioned performance characteristics are explained. In all simulations both the primary and secondary scatterings of annihilation photons in the detector material were taken into account. Simulated times and positions of interactions were smeared using tomograph resolutions obtained experimentally. Further on, in order to reduce the fraction of events with gamma photons scattered in the phantom or in the detector, the signals were processed using selection criteria based on the correlations between the hit-time, hit-position and energy deposition of annihilation photons in the detector (details in Chap. 3).

5.1.1 Sensitivity

The sensitivity of a positron emission tomograph is expressed as the true coincidence events rate T normalized to the total activity A of the source.

In order to calculate sensitivity, a linear 1 MBq source of back-to-back gamma photons with length of 70 cm was simulated along the axis of the scanner in the centre of the AFOV. The NEMA norm requires that the activity should be such, that the number of accidental coincidences is smaller than 5 % of all prompt coincidences. The activity of 1 MBq fulfills that condition for all simulated geometries. The ratio of the accidental coincidences ranges from 0.80 % to 1.34 %, depending on the geometry. The norm requires also that the number of true coincidences for each slice of the scanner should be at least 10,000. Additionally, the 200-cm-long linear source with the same total activity was simulated.

While the sensitivity is a parameter that describes the whole detector with just one number, there is also a sensitivity profile dependent on the position along the axis. For sensitivity profile, the space of the detecting chamber had to be divided into slices and values of the sensitivity profile were calculated for each slice. A slice in PET tomography is a cylindrical-shape segment of the AFOV of the scanner, stretched between single ring of crystals. Its length results from the axial size of a single crystal. Since the J-PET is built from strips arranged axially, it has no physical slices and the space inside the detector was divided into 1 cm virtual slices.

5.1.2 Map of efficiency

Map of efficiency is a 2-dimensional dependence of efficiency of the detector on position on its cross-section (longitudinal or transversal). In order to calculate the maps, the planar sources with zero thickness were used. Usage of such planar sources simplifies obtaining the maps for exact positions of cross-sections. For the longitudinal map (along the axis of the scanner) a rectangular source was used. The source was in the plane containing the axis, had length equal to the length of the detector and width equal to its inner diameter. For the transversal map (in direction perpendicular to the axis of the scanner) a circular source was used. The source was placed in the centre of the AFOV, had diameter equal to the inner diameter of the detecting chamber and it was stretched between the scintillators forming cylinder.

Each map was simulated with source activity of 1 MBq. Because sources had different areas, concentration activity was dependent on the geometry configuration and the map type. However, regardless of these differences, 10 mln of coincidences was collected for each map.

After simulation and data preprocessing, each map was divided into 5 x 5 mm^2 pixels. For each pixel, efficiency was calculated using the following formula:

$$\begin{aligned} E &= \frac{T}{s \cdot t \cdot a}, \\ [E] &= \frac{cps}{kBq \cdot cm^2}, \end{aligned} \tag{5.1}$$

where E is an efficiency in a chosen pixel with, T is a number of true coincidences that were originated from the pixel, s is the area of the pixel, t is the simulated time and a is an activity of the source in kBq per cm^2 (activity density).

While the sensitivity and its profile may be simulated and measured experimentally, maps of efficiency in practice may be obtained only with simulation. Map of efficiency not only extends the standard sensitivity norm (due to providing 2-dimensional information in comparison to 1-dimensional from the sensitivity profile) but is also useful in some image reconstruction algorithms.

5.1.3 Spatial resolution

Spatial resolution of a PET scanner represents its ability to distinguish between two points after image reconstruction [81]. In order to obtain this characteristic, signal determination from the annihilation must be performed and corresponding images must be reconstructed. The NEMA norm recommends to use the FBP algorithm during the spatial resolution determination. The FWHM of the obtained distributions is referred to as point spread function (PSF) and is used as a measure of the spatial resolution. Since the spatial resolution depends on the position inside the AFOV of the scanner, the PSF must be determined for six different positions, defined by the norm. In the axial direction, the source should be placed at the centre of the AFOV and at the distance of three-eighths of the AFOV from the centre of the scanner. In the transverse direction, source should be placed at distances: 1 cm, 10 cm and 20 cm from the axis of the scanner.

In simulations, spherical sources of back-to-back gamma photons, with a diameter of 1 mm, were used. The activity of the source was sufficiently low (equal to 370 kBq [10 μCi]) that the number of accidental coincidences is below 5 % of all collected events. The ratio of the accidental coincidences for each simulated geometry and source position was smaller than 0.2 %. According to the NEMA norm, the number of collected prompt coincidences for each position of the source should be at least 100,000.

Before reconstruction, simulated data were smeared taking into account experimental time and position resolutions. After the selection and data smearing, reconstruction was performed. The smearing of positions and times was performed for three different readout cases as it is shown in Fig. 3.6. For the reconstruction, according to the NEMA norm,

the FBP method was used. The 3D FBP algorithm from the Software for Tomographic Image Reconstruction (STIR) [20] package was used [86].

For each 3D image, a voxel with the maximum intensity was found and three 1-dimensional profiles going through this voxel in direction x, y and z were determined. For each profile, values of FWHM were obtained. These values are interpreted as the spatial resolution of the scanner.

5.1.4 Scatter fraction and NECR

Scatter fraction of the PET scanner quantifies the sensitivity of the detector to scattered radiation. It may be expressed as a ratio between the scattered coincidences and the sum of scattered and true coincidences. It is measured (or simulated) for relatively low source activity, when the number of accidental coincidences is negligible.

NECR is the characteristic that shows the influence of scattered and random coincidences on the performance of the scanner as a function of the source activity and it is a measure of the effective sensitivity of the scanner [29]. The NECR may be defined as:

$$NECR = \frac{T^2}{T + S + R}, \tag{5.2}$$

where T stands for the rate of true coincidences, S – scattered coincidences, R – random (accidental) coincidences. Typically, the NECR grows up to a certain activity concentration and after it decreases slowly. Such a peak of NECR is a figure of merit showing the optimal value of activity of the source for a fixed geometry of the scanner. The smaller value of the activity at the peak, the smaller activity may be applied to the patient in order to get the best possible results. The NECR is also linearly correlated to the square of the Signal to Noise Ratio (SNR^2) [82], the parameter used to determine the reconstructed image quality.

In J-PET, built from plastic scintillators, the annihilation photon interacts via Compton scattering, in a significant fraction of events (depending on the detector geometry) more than once. Therefore, the scattered coincidences consist of the detector- and phantom-scattered ones. However, applying the fixed energy threshold (200 keV) reduces most of the detector-scattered coincidences (see Sec. 3.2.1 and Ref. [76] for more details).

For both scatter fraction and NECR, simulated phantom is a solid cylinder made of polyethylene with an outside diameter equal to 203 mm and length 700 mm. Parallel to the axis of the cylinder, a hole with diameter 6.4 mm is drilled in a radial distance from the axis of the phantom equal to 45 mm. A line source insert is also made of polyethylene and it is a tube with the inside diameter 3.2 mm and outside diameter 4.8 mm. The tube may represent known activity and be placed inside the hole of the phantom. Additionally, 200-cm-long phantom and source were simulated. Only their lengths were modified, while all other parameters (like diameters) were the same as for 70-cm-long ones.

In the simulation used to obtain the scatter fraction pairs of photons, flying back-to-back and emitted from the source with activity 1 kBq, were generated. The value of the activity for obtaining the scatter fraction is limited by the condition that the ratio between the random and true coincidences should be smaller than 1 % [81]. For such a small activity, there were only single accidental coincidences per each data set consisting from hundreds of thousands of prompt coincidences, which means that the activity of 1 kBq fulfills this condition. The NEMA norm also requires that the number of acquired prompt coincidences must be at least 500,000. In presented studies, the number of prompt coincidences was 1 mln.

As a first step of the data processing, the space inside the scanner is axially divided into N virtual slices and N^2 oblique sinograms are generated. The sinogram is a transformation of the LOR into a pair of values: the distance of this LOR to the centre of the detector (in x-y plane) and the angle between the LOR and the x axis of the cross-section of the scanner.

In the second stage, oblique sinograms are converted into rebinned sinograms using the Single Slice Rebinning (SSRB) algorithm [87]. The SSRB assigns a LOR between two detectors (in case of the J-PET tomograph between two regions of different strips) to the sinogram of the transaxial slice lying midway, axially between the two detectors. The number of rebinned sinograms is equal to $2N - 1$. After that, rebinned sinograms are merged into one sinogram (example in the left panel of Fig. 5.1). Using this summed sinogram, all projections are shifted along the "Displacement" axis with maximum value to zero and summed in order to get a 1-dimensional profile (example of such a profile is shown in the right panel of Fig. 5.1). After summing up, values of such obtained profile

at distances ±2 cm from zero are calculated (the distance of 2 cm is specified in the norm). The area of the profile over the line crossing two points at ±2 cm is interpreted as true coincidences, whereas the area below this line corresponds to the scattered (and accidental) coincidences.

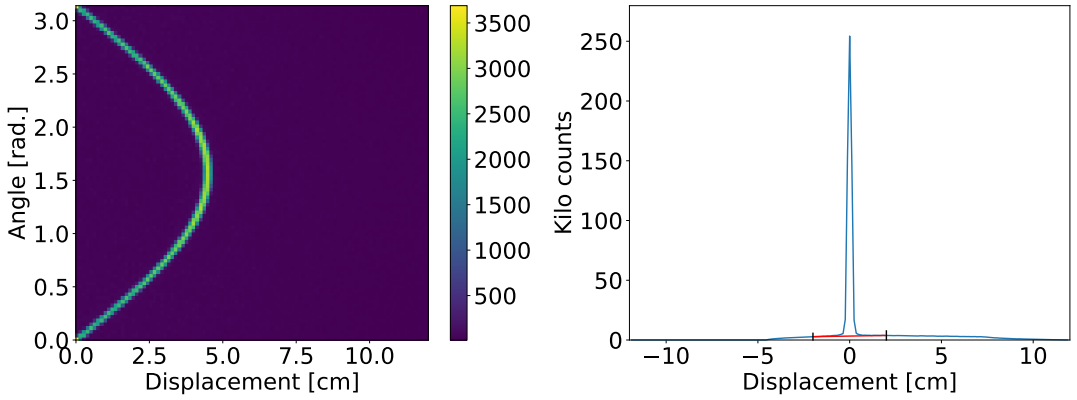

FIGURE 5.1: Sub results of the scatter fraction simulation for single-layer geometry with diameter of 85 cm and strips with length of 50 cm. (left) The sinogram for a whole scanner (all slices summed). (right) One dimensional profile calculated as an aligned to zero using maximum value and summed projections of sinogram presented in left panel. The cut level visualized as a red line is determined using values of the profile at ±2 cm from zero.

Method of obtaining the NECR is analogous to the method of measuring and calculating scatter fraction. While the scatter fraction is measured for single activity of the source, the NECR varies as a function of the activity.

5.2 Results

In this section, chosen results of computed characteristics are presented. Because of the variety of possible configurations of the J-PET scanner (taking into account parameters listed in section 3.1.1) only exemplary results for some geometries are presented in the thesis.

5.2.1 Sensitivity

Sensitivities for different geometries of the J-PET scanner are presented in Fig. 5.2. Sensitivity profiles are presented in Figs 5.3 (70-cm-long source) and 5.4 (200-cm-long source). Profiles are presented for positions in range between ± half source length.

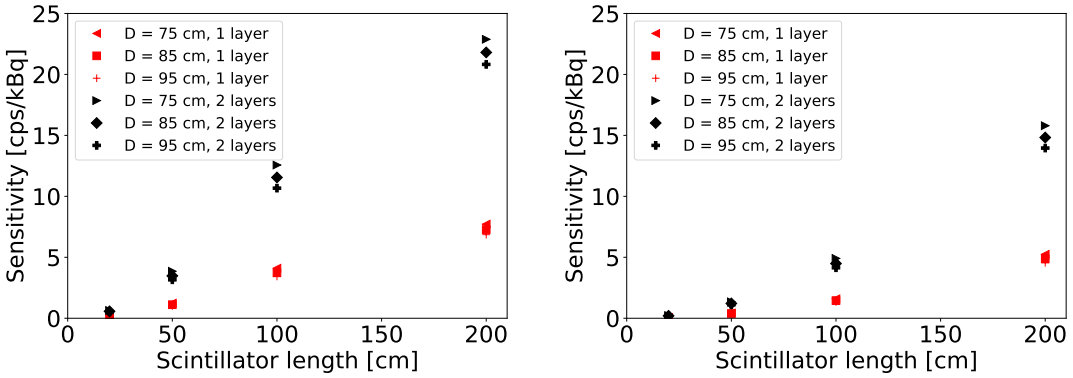

FIGURE 5.2: Sensitivities for different geometries of the J-PET scanner; (left) 70-cm-long standard source, (right) 200-cm-long extended source.

One can see, that values of sensitivities obtained for single- and double-layer geometries with the same diameters and lengths of strips, differ about 3 times. At first moment, one could suppose that the sensitivity for the double-layer geometry would be almost 4 times bigger than for the corresponding single-layer one. However, there are two reasons, that the ratio between the corresponding sensitivities is about 3. Firstly, probability of detection of the single gamma photon with two layers is about 1.82 times bigger than with one layer (the efficiency of registration of the 511 keV photon in the first layer is equal to about 17.8%)[1]. It means that the probability of registration of the coincidence with double-layer geometry would be at most $1.82^2 = 3.31$ times higher than for single-layer geometry with the same strips length. Secondly, not all true coincidences are properly registered due to a fact that if beside the scatterings forming the true coincidence, the additional (scattered or accidental) interaction occurs during the time window, the event is rejected. The effect is the stronger, the higher the detection efficiency (which grows with the number of layers and with the length of strips). Both effects lead to the improvement of sensitivity by factor of about 3 only.

Adding the second layer of strips increases the detection efficiency. However, the rate of the detector-scattered and accidental events grows faster than the rate of true coincidences. This is caused by the fact that in case of two layers there is additional probability for interlayer scatterings which are not increasing the rate of true coincidences but may increase the rate of scattered and accidental coincidences.

[1] In the first layer about 0.178 of all hits is registered, therefore, about 0.822 reaches the second one. The second layer again registers about 0.178 of hits that reached it ($0.178 \cdot 0.822 \approx 0.146$). Summarily, about $0.178 + 0.146 = 0.324$ of all hits going through two layers, is registered. In reference to single-layer geometry, double-layer geometry is more sensitive by a factor of $0.324/0.178 = 1.82$.

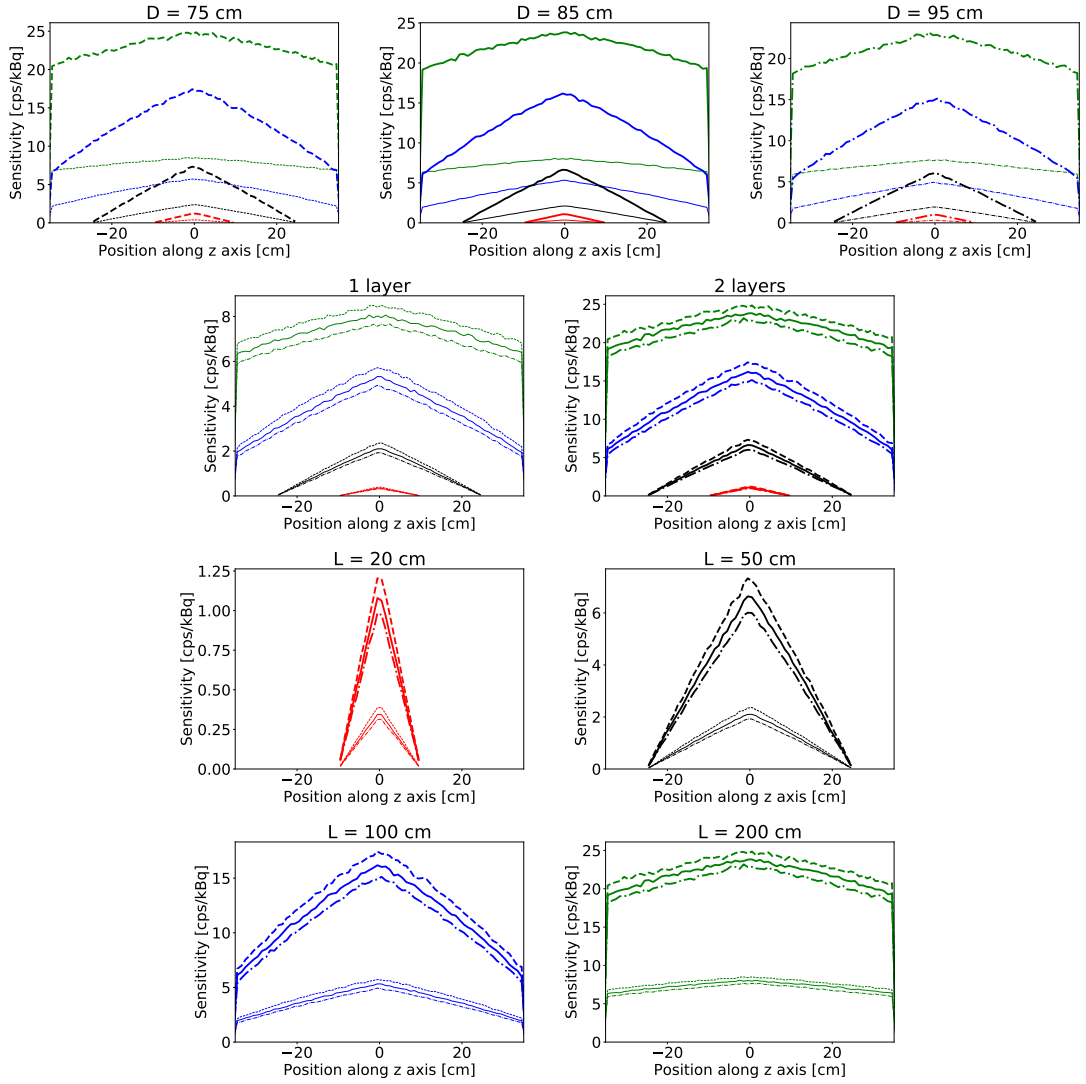

FIGURE 5.3: Sensitivity profiles grouped by the diameter of the detecting chamber (1st row), number of layers (2nd row) and lengths of the scintillators (3rd and 4th rows). Legend: D = 75 cm (dashed - -), D = 85 cm (solid -), D = 95 cm (dashed-dotted -.-), 1 layer (thin lines), 2 layers (thick lines), L = 20 cm (red), L = 50 cm (black), L = 100 cm (blue), L = 200 cm (green).

Let's take into account a single event: for single-layer geometry exactly two hits interact in opposite strips and they fit in the time window. The event is treated as a true coincidence. If we would add second layer of strips, then we would increase the probability of a situation, in which we would have the same true coincidence as above and additional scattered or accidental hit, which also fits in the coincidence window with two first hits. Then, the event won't be treated as a true coincidence. It may be rejected because there are 3 hits and due to the finite energy resolution all may be registered with energy above the fixed energy threshold (200 keV) in the time window. Of course the same may

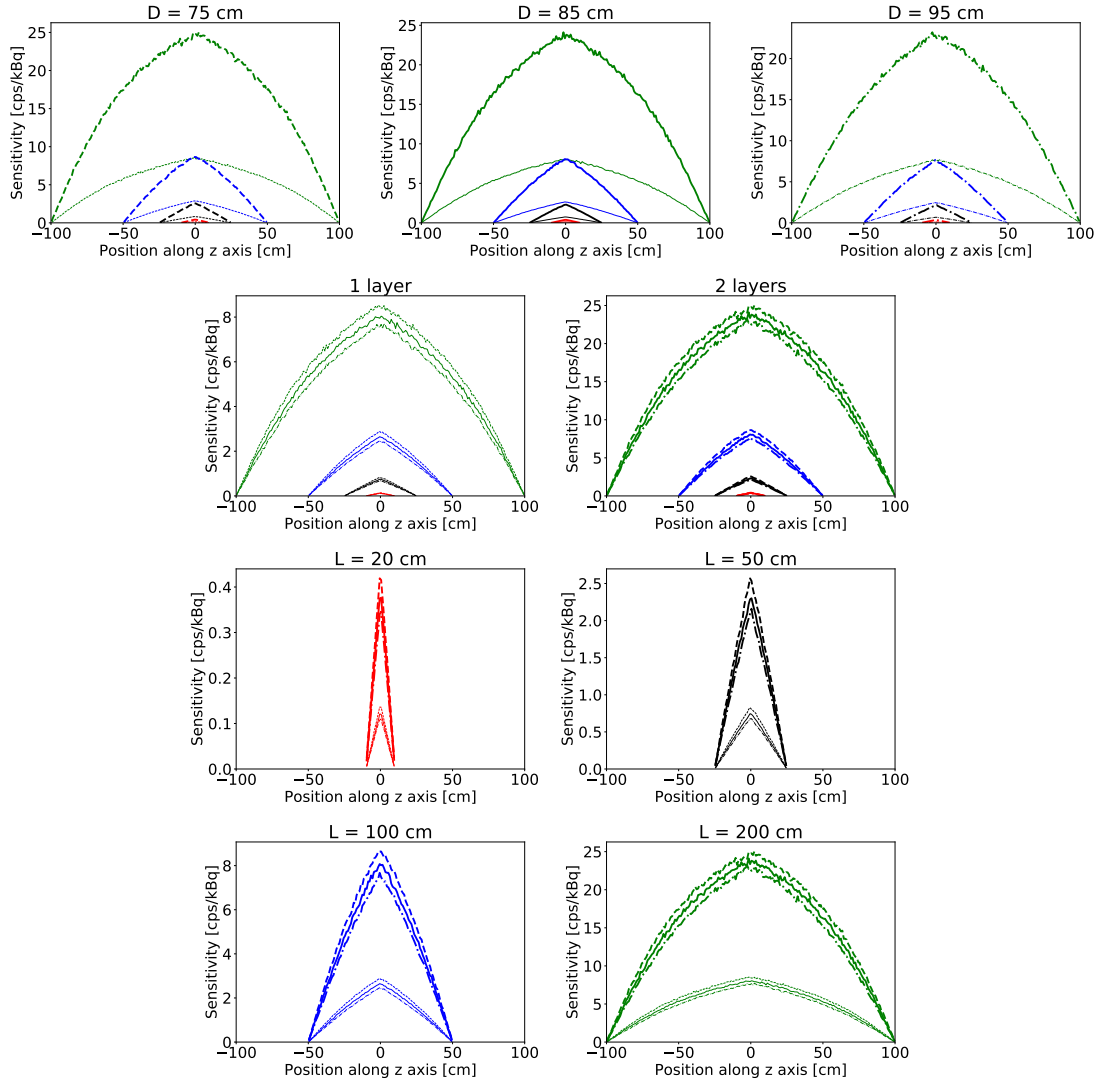

FIGURE 5.4: Sensitivity profiles for 200-cm-long source grouped by the diameter of the detecting chamber (1st row), number of layers (2nd row) and lengths of the scintillators (3rd and 4th rows). Legend: D = 75 cm (dashed - -), D = 85 cm (solid -), D = 95 cm (dashed-dotted -.-), 1 layer (thin lines), 2 layers (thick lines), L = 20 cm (red), L = 50 cm (black), L = 100 cm (blue), L = 200 cm (green).

happen for single-layer geometries but the effect is stronger for double-layer geometries.

Sensitivities and sensitivity profiles obtained for 2 m long rod sources are much lower than for 70 cm sources. It is because the shorter the source, the more activity is located in the central region of the AFOV of the scanner (which translates into higher number of detected true coincidences). The difference is more visible for shorter lengths of scintillators (the larger part of source extends beyond the detecting chamber). As visible in sensitivity profiles (Figs 5.3 and 5.4), sensitivity is much higher in the center of the AFOV than in the ends of the detecting chamber.

5.2.2 Map of efficiency

In this section maps of efficiency for following configurations of the J-PET scanner are presented: single- and double-layer regular cylinder J-PET scanner with lengths 50 cm, 100 cm and 200 cm (Figs 5.5-5.7), single- and double-layer Modular J-PET scanner with lengths 50 cm, 100 cm and 200 cm (Figs 5.8-5.10) and three-layer laboratory prototype (Fig. 5.11). For each configuration, region with semi-uniform efficiency lies in a cylinder with radius of about 2/3 of the radius of detecting chamber and ± 1/4 AFOV from the center of the detector. Region with the highest efficiency is located in the nearby of the scintillators, reaching efficiency of about 2.5 times higher than in the central region of the detecting chamber. While in case of the regular J-PET geometries there are no visible artifacts caused by strip construction of the detector, for the Modular J-PET configurations, due to the modular construction, there are some linear nonuniformities in longitudinal maps. These nonuniformities are also visible for the laboratory three-layer prototype because of angular gaps in its construction (Fig. 5.11).

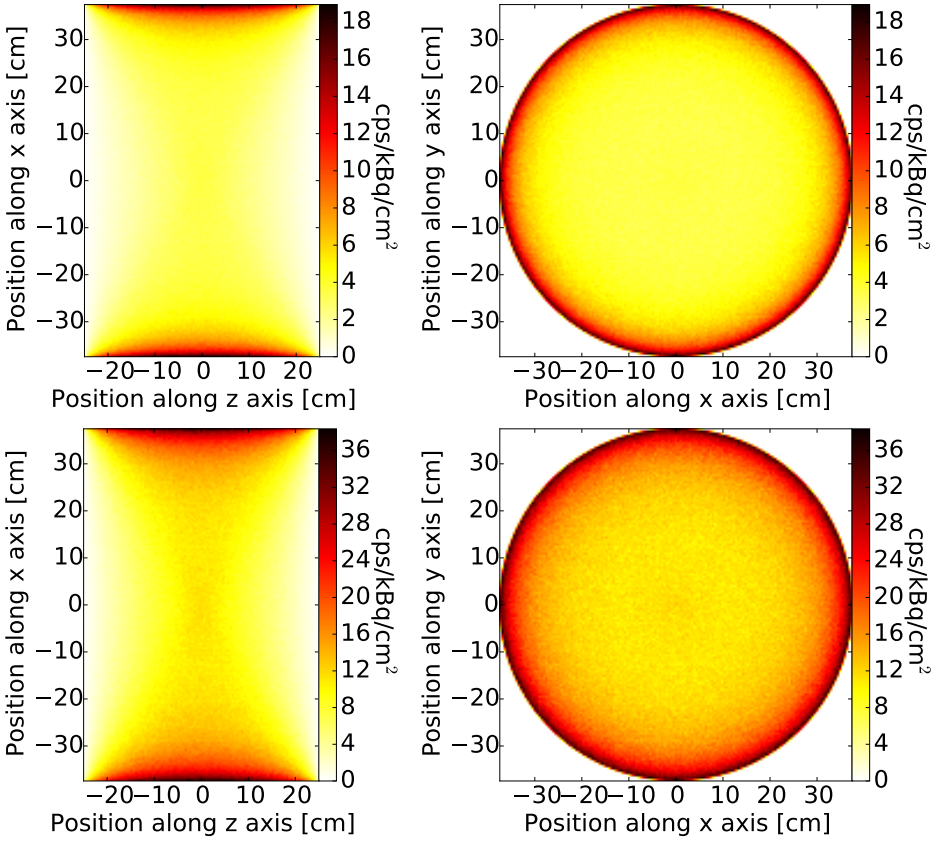

FIGURE 5.5: Maps of efficiency for the single-layer (top) and double-layer (bottom) J-PET scanner with 50-cm-long strips

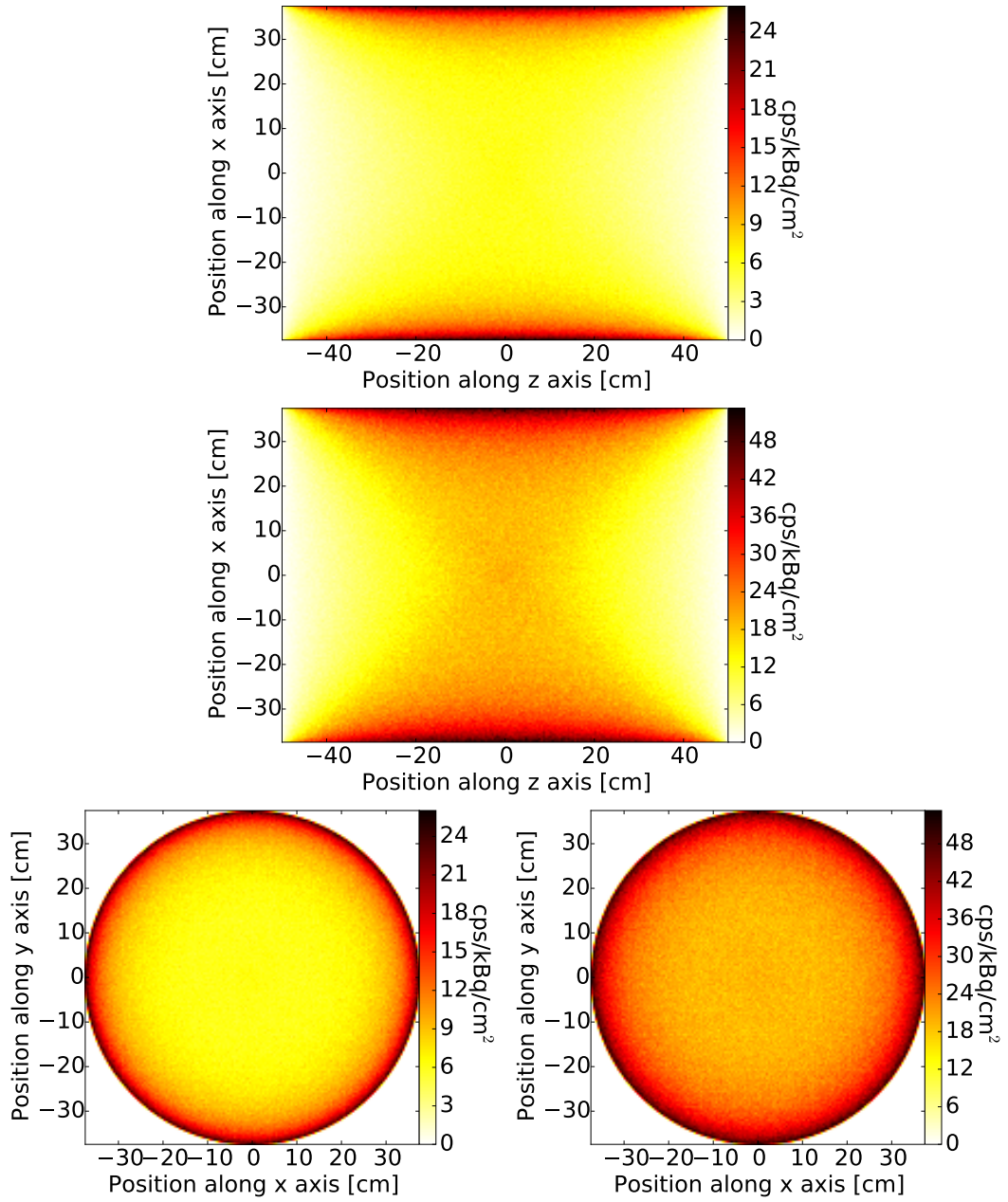

FIGURE 5.6: Maps of efficiency for the single-layer (top and left bottom) and double-layer (middle and right bottom) J-PET scanner with 100-cm-long strips

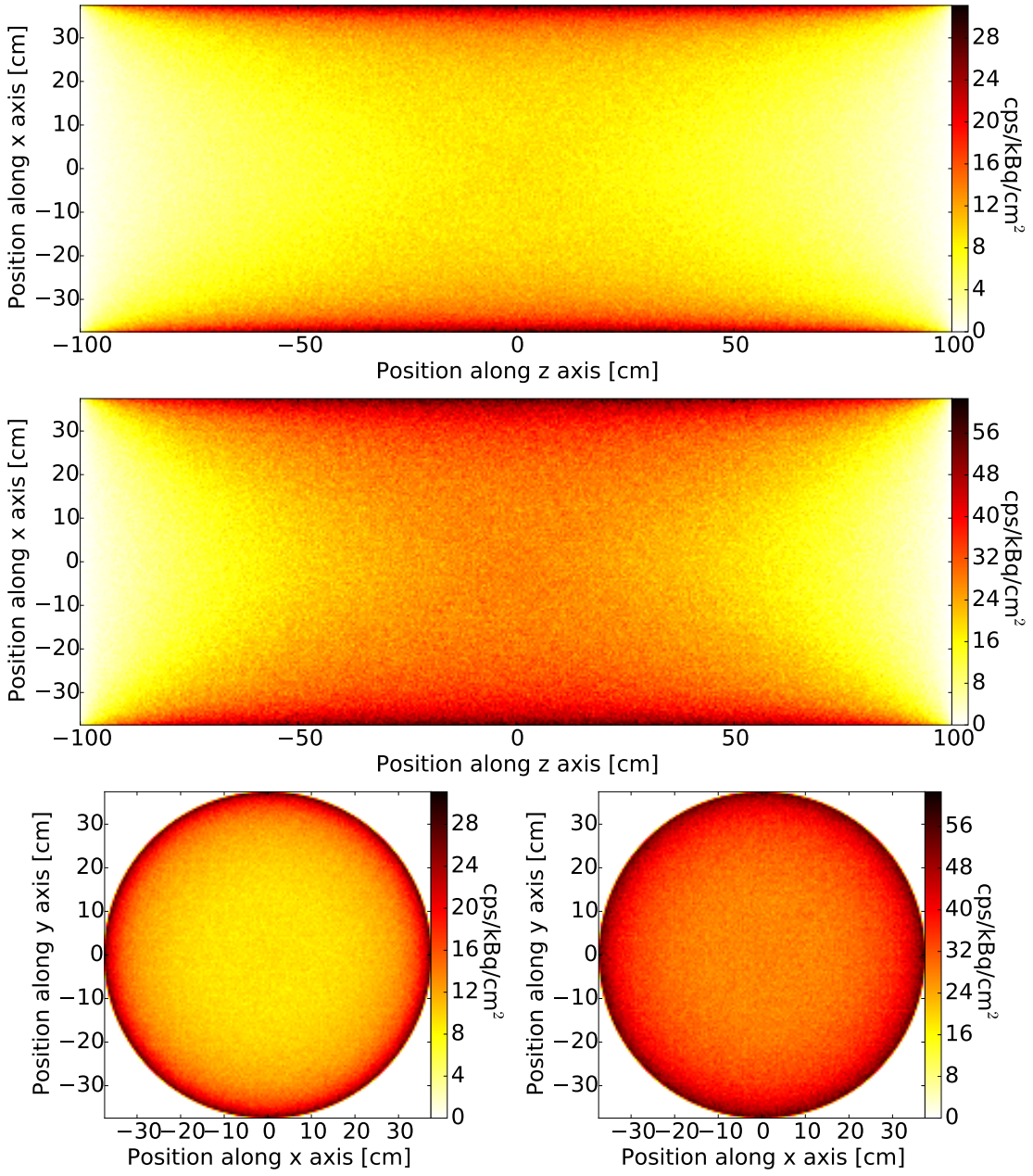

FIGURE 5.7: Maps of efficiency for the single-layer (top and left bottom) and double-layer (middle and right bottom) J-PET scanner with 200-cm-long strips

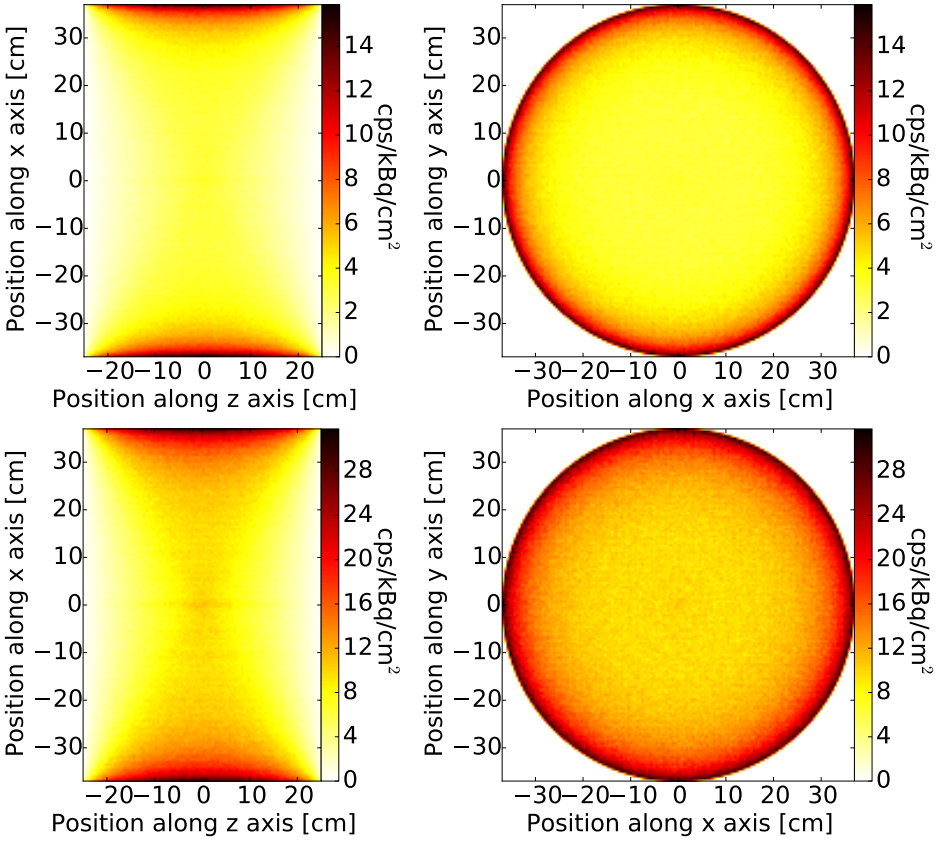

FIGURE 5.8: Maps of efficiency for the single-layer (top) and double-layer (bottom) Modular J-PET scanner with 50-cm-long strips

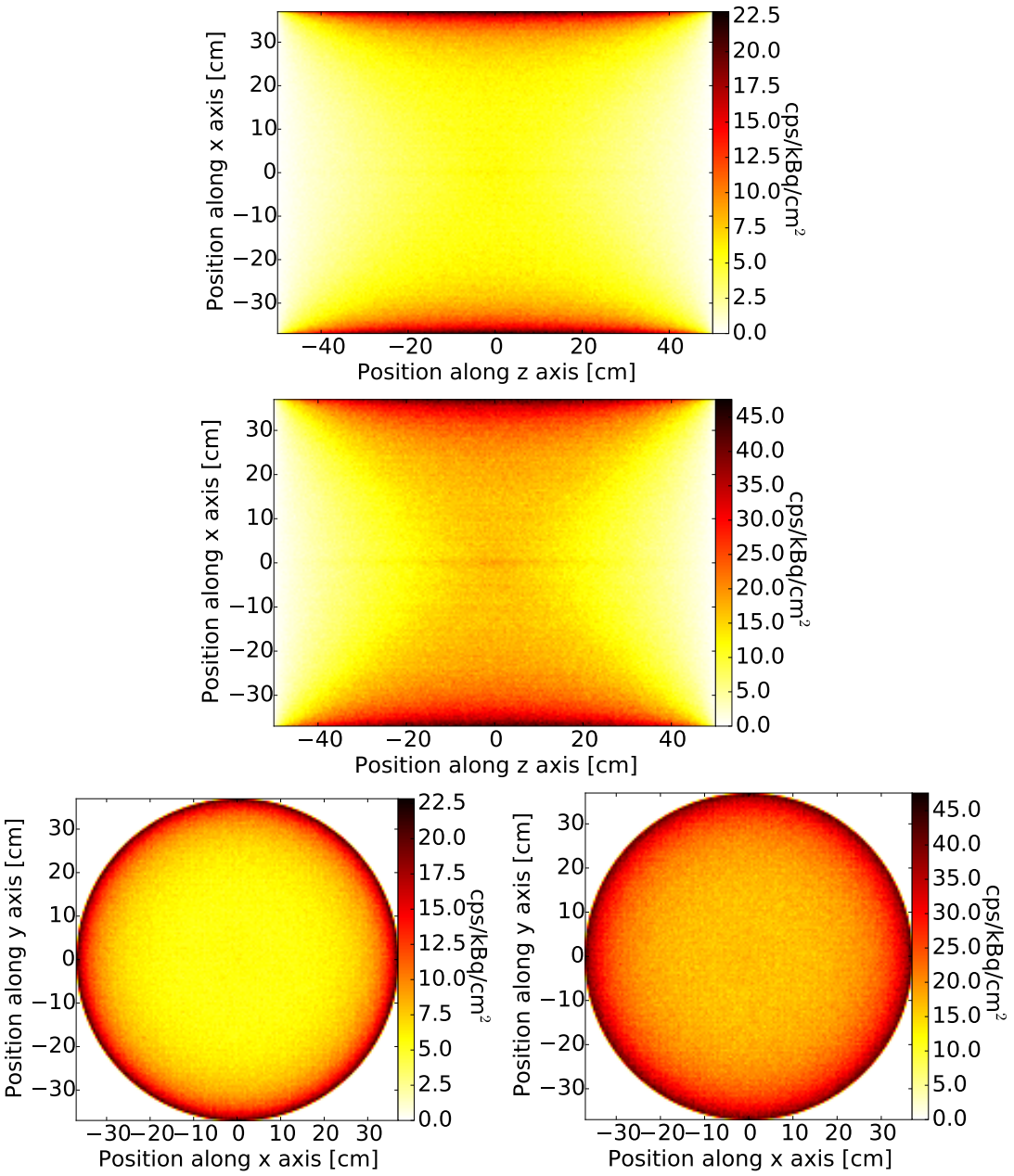

FIGURE 5.9: Maps of efficiency for the single-layer (top and left bottom) and double-layer (middle and right bottom) Modular J-PET scanner with 100-cm-long strips

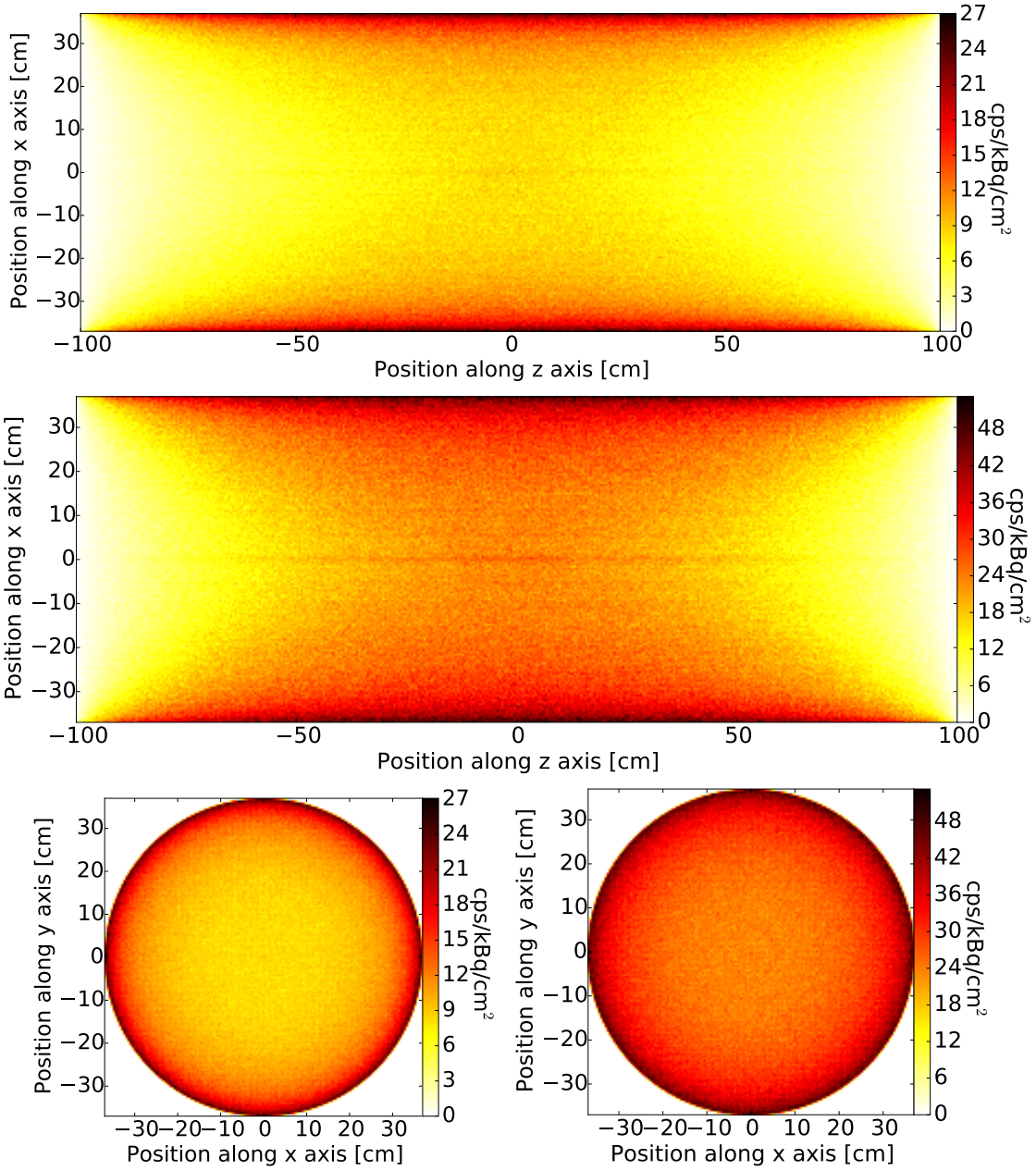

FIGURE 5.10: Maps of efficiency for the single-layer (top and left bottom) and double-layer (middle and right bottom) Modular J-PET scanner with 200-cm-long strips

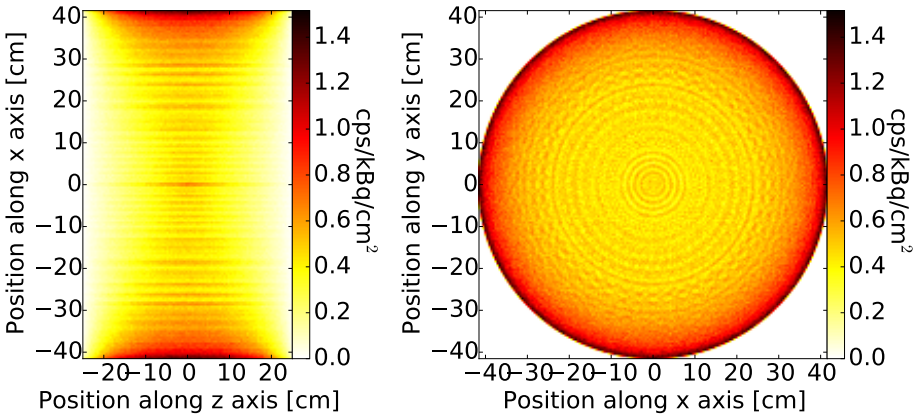

FIGURE 5.11: Maps of efficiency for the three-layer laboratory prototype of the J-PET scanner with 50-cm-long strips

5.2.3 Spatial resolution

Results were selected in order to show influence of each parameter on the final spatial resolution of the scanner. Since the 2nd layer of strips influences mainly the detection efficiency, results of the spatial resolution for the double-layer geometries are qualitatively the same.

Firstly, the influence of the axial position of the scanner was investigated. The geometry was fixed to the single-layer chamber with the diameter of 85 cm and strips with length of 50 cm and thickness equal to 7 mm. Hit-time and hit-position resolutions were used as anticipated for the SiPM readout. Results are presented in Fig. 5.12. All resolutions seem to be only very weakly dependent on radial position of the source. There is also no visible difference between resolutions for sources placed in the centre of the AFOV and in 3/8 of the AFOV. However, the axial resolution for the SiPM readout is 3 times worse than the radial and tangential resolutions.

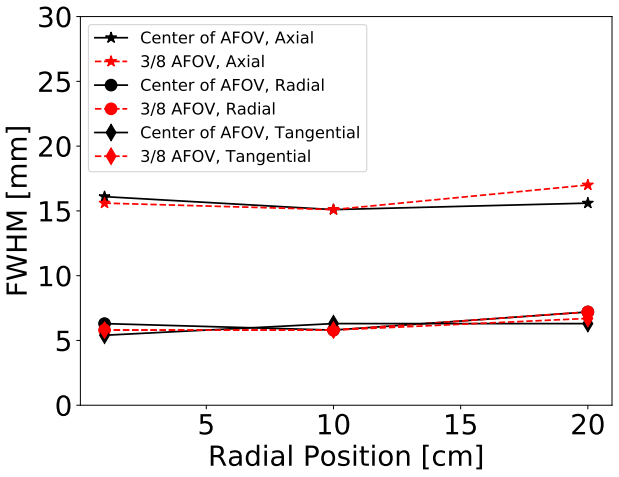

FIGURE 5.12: Spatial resolution in three directions - the radial, tangential and axial. The geometry was fixed to the single-layer chamber with the diameter of 85 cm and strips with length of 50 cm and thickness 7 mm. Hit-time and hit-position resolutions were used as anticipated for the SiPM readout. The axial resolution for this readout is 3 times worse than the radial and tangential resolutions.

Secondly, the type of the readout attached to the strips was taken into account (PMT, SiPM or SiPM+WLS) by smearing simulation data with experimental resolutions (see App. C). Geometry was fixed to the single-layer chamber with the diameter of 85 cm and strips with length of 50 cm and thickness of 7 mm. Results for different types of readouts

are presented in Fig. 5.13. It is important to note, that only axial spatial resolution depends on the kind of the anticipated light readout. Simulations confirmed intuition, viz that the smaller the experimental uncertainty, the better the axial resolution. Additionally, they showed that if the number of collected coincidences is large enough, the spatial resolution barely depends on the position of the source along the axis of the scanner.

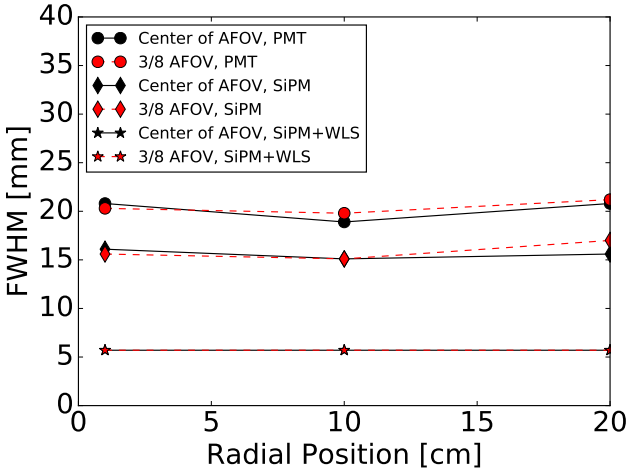

FIGURE 5.13: Axial resolution for different types of readouts attached to scintillator strips and two axial positions as a function of radial position of the source. Presented results were obtained for the single-layer geometry with the diameter of 85 cm and strips with length of 50 cm and thickness 7 mm. Note, that the results for SiPM+WLS at the centre (black stars) and at 3/8 AFOV (red stars) overlap.

Finally, the geometry of the single strip was taken into account. Results for 3 lengths and 2 thicknesses of scintillator strips are presented in Fig. 5.14. Position of the source in each case was fixed to (1,0,0) cm (only 1 cm from the centre of the tomograph). Simulations showed that, as expected in the case of the J-PET without additional WLS readout, the axial resolution worsens proportionally to the length of the strip (left panel of Fig. 5.14). However, it improves and remains constant along the scanner in case of the readout with the WLS layer (right panel of Fig. 5.14). Because of the axial symmetry of the detecting chamber, radial and tangential resolutions are independent of the length of the strip. For each type of the resolution, better results are obtained for thinner strips (4 mm), e.g. for the radial and tangential resolution, they are reduced twice with respect to results obtained with strips of 7 mm thickness. For the axial resolution there is a slight difference between geometries with 4 mm and 7 mm thick strips.

An example of reconstruction of the source placed in the centre of the tomograph may

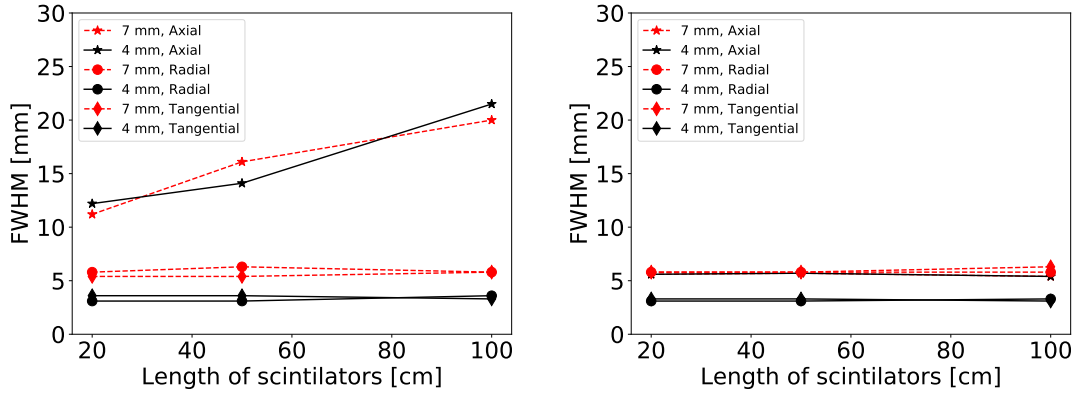

FIGURE 5.14: Spatial resolution for 3 lengths and 2 thicknesses of scintillator strips assuming (left) SiPM readout and (right) SiPM+WLS readout.

be seen in Fig. 5.15 (geometry was fixed to the single-layer chamber with the diameter of 85 cm and strips with length of 50 cm and thickness equal to 4 mm; silicon photomultipliers were used as photodetectors).

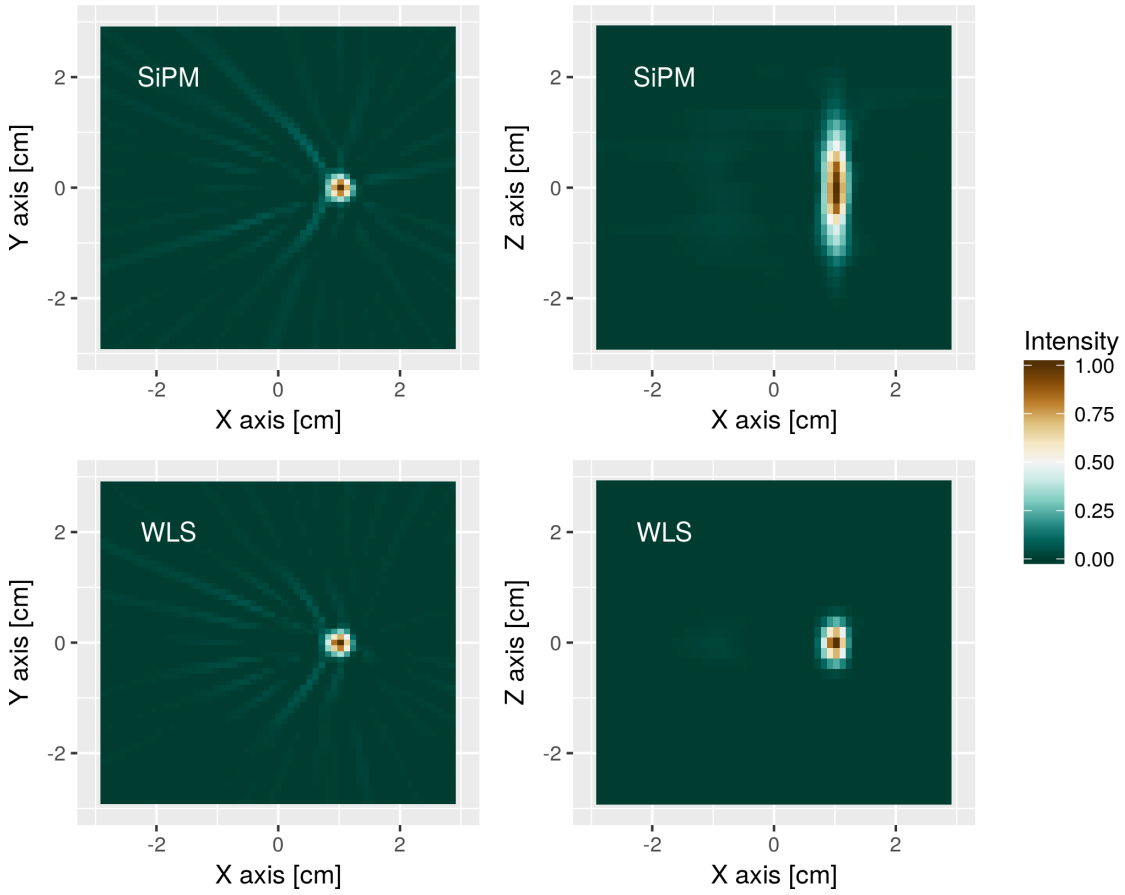

FIGURE 5.15: Example reconstruction of the source placed in the central position [(1,0,0) cm] of the detecting chamber. The geometry consisted of the single-layer chamber with the diameter of 85 cm and strips with length of 50 cm and thickness 4 mm. Silicon photomultipliers (SiPM) were used as photodetectors in upper images, WLS strips were used in bottom images. Left column corresponds to the cross-section perpendicular to the axis, right column to the cross-section along the axis of the scanner. Background artifacts visible in XY-plane are due to a fact that in STIR implementation of the FBP method TOF is not taken into account. Image by Roman Shopa.

5.2.4 Scatter fraction and NECR

In this section, results of scatter fraction and NECR are presented for 8 geometries: single- and double-layer scanners and 4 lengths L of scintillators: 20 cm, 50 cm, 100 cm and 200 cm. The diameter of the detector chamber was 85 cm and the profile of the single scintillator was 20 mm x 7 mm.

Results obtained using the method based on the sinogram analysis are presented in Tab. 5.1. The scatter fraction was also calculated using the true Monte Carlo information about types of coincidences in each event. Results for such calculations are presented in Tab. 5.2. Values obtained for these 8 geometries are consistent with the value calculated

in previous studies for one layer 384 strip geometry [76]. The scatter fraction calculated at sinogram analysis is smaller than at the identification of events based on the information from Monte-Carlo simulations. It is due to a usage of 12 cm radius cylindrical cut in the processing of sinograms [81, 82].

Nr of layers	**L = 20 cm**	**L = 50 cm**	**L = 100 cm**	**L = 200 cm**
1	35.8 %	35.6 %	35.0 %	34.5 %
2	35.2 %	35.4 %	34.3 %	34.5 %

TABLE 5.1: Scatter fraction for 8 geometries of the J-PET scanner calculated using the method based on sinograms analysis for 70-cm-long phantom

Nr of layers	**L = 20 cm**	**L = 50 cm**	**L = 100 cm**	**L = 200 cm**
1	48.6 %	48.7 %	47.3 %	46.8 %
2	50.8 %	51.5 %	50.7 %	50.5 %

TABLE 5.2: Scatter fraction for 8 geometries of the J-PET scanner calculated using the method based on true Monte Carlo for 70-cm-long phantom

Nr of layers	**L = 20 cm**	**L = 50 cm**	**L = 100 cm**	**L = 200 cm**
1	35.6 %	35.9 %	36.1 %	36.7 %
2	35.2 %	35.2 %	36.2 %	36.6 %

TABLE 5.3: Scatter fraction for 8 geometries of the J-PET scanner calculated using the method based on sinograms analysis for 200-cm-long phantom

Nr of layers	**L = 20 cm**	**L = 50 cm**	**L = 100 cm**	**L = 200 cm**
1	51.6 %	52.4 %	52.9 %	52.9 %
2	53.9 %	55.0 %	56.1 %	56.3 %

TABLE 5.4: Scatter fraction for 8 geometries of the J-PET scanner calculated using the method based on true Monte Carlo for 200-cm-long phantom

In order to calculate NECR with the Monte Carlo method, rates of true, scattered and accidental coincidences were calculated for both 70 cm (Fig. 5.16) and 200 cm (Fig. 5.17) long phantoms. Simulations were performed for activity concentrations in the range between 0 and 90 kBq/cm^3 (total activity of source inside the phantom was between 1 MBq and 2000 MBq).

After that, the NECR characteristic was calculated with both the true MC method based on obtained rates and the method based on the analysis of sinograms for both 70-cm-long (Fig. 5.18) and 200-cm-long (Fig. 5.19) phantoms. Peaks for single-layer tomographs are obtained for higher activity concentrations than for double-layer scanners (for the same length of strips). On the other hand, the longer the strips, the lower the value of activity

concentration, for which the peak is obtained. It is due to the fact that the position of the peak is dependent on the efficiency of the tomograph, which grows with the number of layers and with the length of strips (true coincidences rate is squared in the nominator of the NECR formula, see Eq. 5.2). Additionally, for 200-cm-long phantom obtained values are about 30 % smaller than for 70-cm-long phantom. It is due to the fact that for longer phantom and the same total activity of the source shorter part of the phantom lies in the region of high sensitivity (which is in the centre of the AFOV).

The best results were obtained for 70-cm-long phantom and for the geometry with two layers and 200-cm-long strips. For this geometry, the NECR peak was about 430 kcps for activity concentration of about 45 kBq/cm^3, for the method based on the sinograms analysis. As in case of the scatter fraction calculations, the true MC based method gives characteristics, which are about twice lower than in case of characteristics obtained using the sinograms analysis [82]. The difference is caused by the sharper cylindrical threshold applied in the sinograms analysis (12 cm radius cylindrical cut) compared to ellipsoidal threshold in the true MC based method (Sec. 3.2.1). Such a sharper threshold reduces the number of scattered and accidental coincidences and because of that increases the NECR characteristic (rates of scattered and accidental coincidences are in the denominator of the NECR formula, see Eq. 5.2).

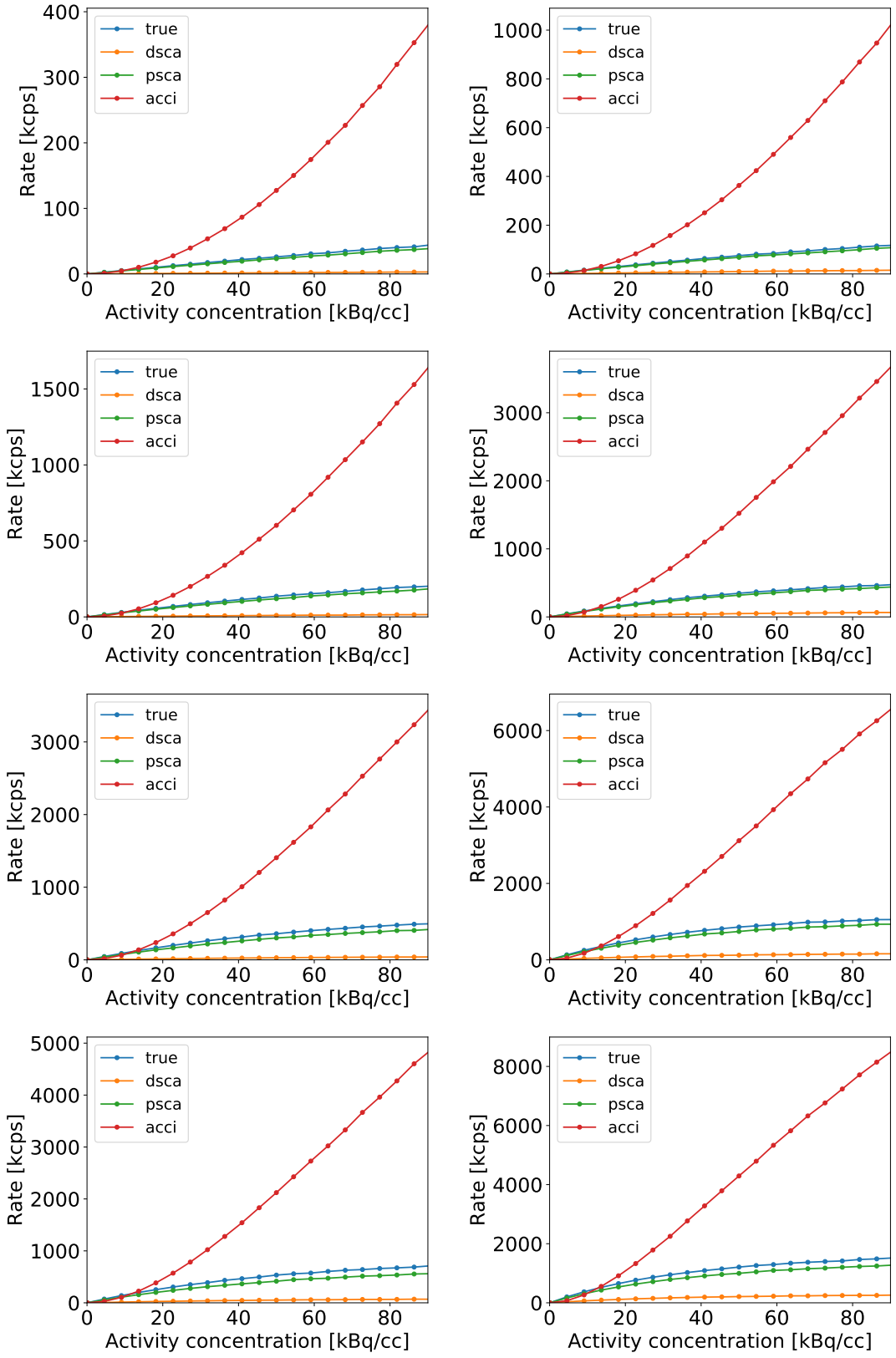

FIGURE 5.16: Count rates of different types of coincidences for 70-cm-long phantom and 8 geometries of the J-PET scanner with diameter D of 85 cm (dsca - detector-scattered, psca - phantom-scattered, acci - accidental coincidences). Left and right panel show results obtained for single- and double-layer detectors, respectively. In the first row of the figure, there are rates for 20 cm scintillators, in the second row for 50 cm scintillators, in the third row for 100 cm scintillator strips and in the fourth row for 200 cm scintillators.

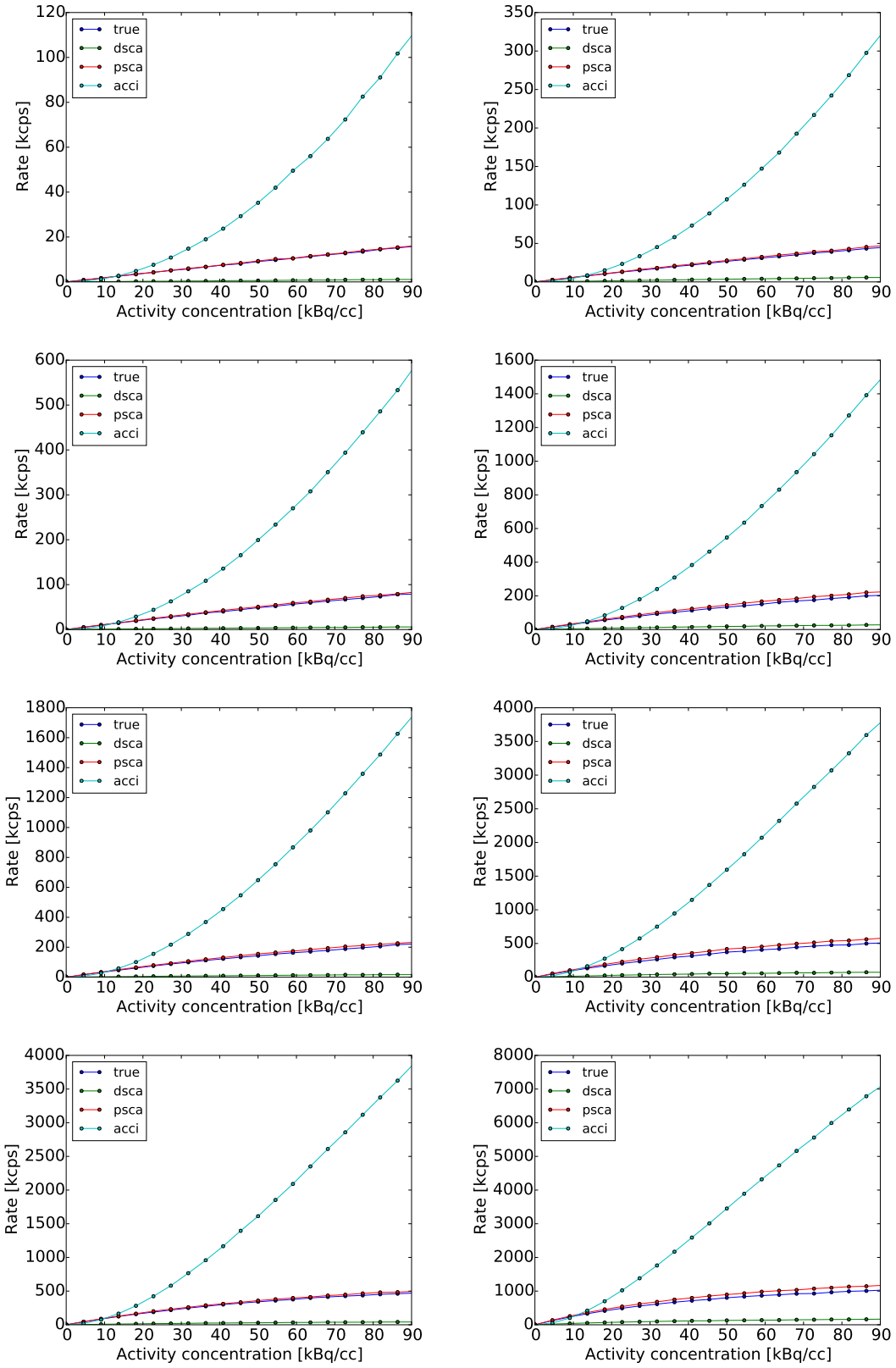

FIGURE 5.17: Count rates of different types of coincidences for 200-cm-long phantom and for 8 geometries of the J-PET scanner with diameter D of 85 cm (dsca - detector-scattered, psca - phantom-scattered, acci - accidental coincidences). Left and right panel show results obtained for single- and double-layer detectors, respectively. In the first row of the figure, there are rates for 20 cm scintillators, in the second row for 50 cm scintillators, in the third row for 100 cm scintillator strips and in the fourth row for 200 cm scintillators.

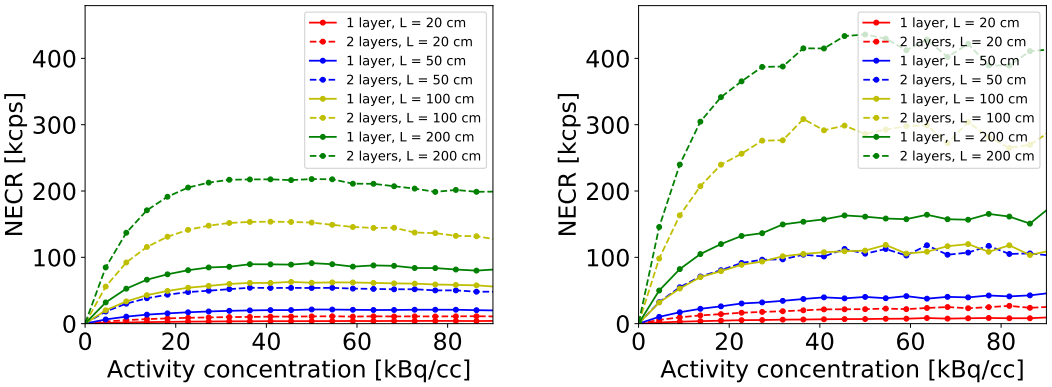

FIGURE 5.18: NECR as a function of activity concentration for 8 geometries of the J-PET scanner for 70-cm-long phantom. (left) NECR calculated using the true MC rates. (right) NECR calculated using the method based on the sinograms analysis.

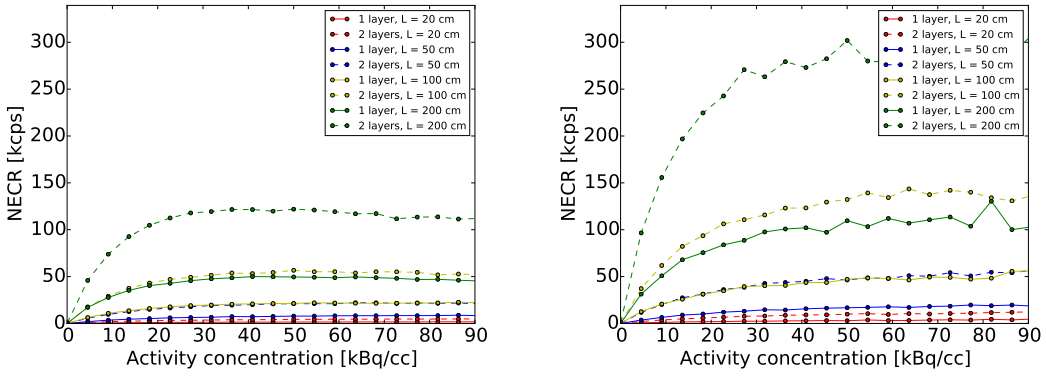

FIGURE 5.19: NECR as a function of activity concentration for 8 geometries of the J-PET scanner for 200-cm-long phantom. (left) NECR calculated using the true MC rates. (right) NECR calculated using the method based on the sinograms analysis.

Chapter 6

Comparison of the J-PET tomograph to commercial and the prototype PET devices

6.1 Performance of current PET scanners

The market of PET devices is still growing and currently its value is estimated to nearly 1 billion US $[1]. Leaders of this market are: General Electric Healthcare (GE), Siemens Healthcare and Philips Healthcare. Although these companies occupy about 90 % of the market, there are also other smaller producers of PET devices, like: Toshiba, Hitachi, Neusoft, Topgrade HealthCare and United Imaging. All these producers provide together over a dozen of different models of PET scanners. All they compete to deliver devices with the best possible parameters and characteristics. In this section flagship products of leading vendors of PET scanners are characterized. Also few devices, which are under development, are mentioned.

6.1.1 Commercial scanners in medical use

One of most modern GE PET devices is GE Discovery IQ - the PET/CT scanner [88]. It is a scalable device, that may be built of 2 up to 5 ring detectors. The AFOV in case of

[1] https://www.futuremarketinsights.com/press-release/positron-emission-tomography-scanners-market, https://www.itnonline.com/article/pet-imaging-market-overview-and-trends

5-ring version is 26 cm. Sensitivity of this scanner, measured at the centre and at 10 cm is 22.8 cps/kBq and 20.4 cps/kBq. Spatial resolution is in range of 4.2 mm at 1 cm to 8.5 mm at 20 cm. The tomograph has scatter fraction of 36.2 % and achieves the NECR peak of 124 kcps at 9.1 kBq/cm^3.

Siemens provides the Biograph family of PET devices. The most popular and flagship Siemens PET/CT scanner is the Biograph mCT [89, 90]. The scanner has the AFOV of 218 mm. The sensitivity of this scanner is about 9.7 cps/kBq in the centre of the AFOV. Both axial and tangential resolutions measured experimentally (FWHM) are 4.4 mm in the distance of 1 cm from the axis of the scanner. In the distance of 10 cm from the axis, the resolutions are 5.2 mm (transverse radial), 4.7 mm (transverse tangential) and 5.9 mm (axial). The Biograph mCT scanner has scatter fraction of 33.2 % and achieves the NECR peak of 180.3 kcps at 29 kBq/cm^3.

Philips provides the Vereos PET/CT [91, 92] scanner with the AFOV of 164 mm. The sensitivity measured at the centre is 22.1 cps/kBq and at 10 cm is 22.2 cps/kBq. The resolutions in the centre are 3.99 mm (both transverse and axial). The resolutions in the distance of 10 cm from the axis of the scanner are 4.36 mm (transverse tangential), 4.64 mm (transverse radial) and 4.39 mm (axial). The scatter fraction for this model is 31.6 % and the NECR peak of 646 kcps is achieved at 52.8 kBq/cm^3.

6.1.2 PET devices under development

As it was mentioned before, efforts of research teams involved in development of PET devices are focused mainly on improving characteristics of scanners and building the cost-effective and whole-body scanners. Examples of such prototype scanners with large AFOV are: 3D PET scanner based on lead-walled straw detectors [93], RPC-PET based on resistive plate chambers [94–96], the first generation of the presently developed total-body EXPLORER PET [32–35] and the J-PET scanner based on the plastic scintillator strips discussed in this thesis. In below paragraphs three first devices are shortly characterized.

The lead-walled straw detector is the small animal PET device. The sensitivity is 0.09 %, for a point source in the center FOV, in the absence of a scattering medium. The spatial

resolution is uniform over the entire AFOV and is equal to 1.2 mm (radial), 1.2 mm (tangential) and 2.4 (axial). The scatter fraction is 30 %.

The RPC-PET tomograph is the whole-body detector with the AFOV of 2400 mm. The absolute 3D true sensitivity of an RPC TOF-PET scanner is estimated to be about 4 times higher than sensitivity for crystal-based PET devices. The simulations suggest that the expected spatial resolution of the RPC TOF-PET scanner, is expected to be of 2.3 mm (FWHM). The average scatter fraction obtained for the RPC TOF-PET scanner with the 700 mm long NEMA NU2-2001 phantom, was of 52 %. The NECR obtained for the RPC TOF-PET scanner was found to raise from 133 kcps to a peak value of 167 kcps decreasing then to 164 kcps, for activity concentrations of, respectively, 3.4 kBq/cm^3, 7.6 kBq/cm^3 and 8.4 kBq/cm^3.

The EXPLORER detector is projected to have an effective sensitivity for total body imaging that is 40-fold higher than current commercial scanners. Its spatial resolution in the centre of the AFOV is estimated to about 3 mm and scatter fraction is estimated to 35.1 %.

6.2 The J-PET scanner vs. competitive solutions

Usage of the low-cost components in the J-PET construction (plastic detectors, minimized amount of photomultipliers) reduces costs of production of the total-body PET device. While the total-body EXPLORER based on inorganic scintillators is estimated to cost about 10 mln €, the cost of total-body Modular J-PET scanner with 2 m AFOV is estimated to about 2 mln € only.

Such a cost optimization must not require decrease in efficiency and safety. In Tab. 6.1 plastic detectors used in the J-PET scanner and in other solutions are summarized. Much lower density of plastic scintillators is compensated with their incomparably better time properties. Time of decay in the plastic scintillators is about 20 times smaller than in case of inorganic ones [97–99].

As J-PET scanner is built of plastic scintillator strips which are equipped with two photodetectors placed on its ends, the process of enlarging AFOV requires only strips to be replaced (and not read-out elements). All solutions currently offered on the market

DETECTOR	J-PET detector (plastic strips EJ230)	LYSO crystal (Philips, GE, United Imaging)	LFS crystal (Zecotec)
Density	1.03 g/cc	7.1 g/cc	7.35 g/cc
Attenuation length @511 keV	10.2 cm	1.2 cm	1.15 cm
Decay	1.8 ns	45 – 37 ns	33 ns
Light yield	~10 000 photons/MeV	30000 – 40000 photons/MeV	30700 – 32700 photons/MeV
Energy resolution	18 % (not important due to different method of data acquisition)	8,00 %	8,00 %

TABLE 6.1: Comparison of the J-PET plastic detector with inorganic ones used in competitive solutions [97–99]

SCANNER	2-m-long J-PET (EJ230)	Vereos PET/CT (LYSO)	EXPLORER (LYSO)
Coverage (AFOV)	200 cm	16.4 cm	194 cm
Acceptance angle	Full AFOV	Full AFOV	57 deg
Coincidence time window	3 ns (software enabled)	4.5 ns	4.5 - 6.9 ns (depends on angle)
Timing resolution	220 ps	310 ps (4.6 cm accuracy)	430 ps
System sensitivity @ 0 cm	~20 cps/kBq	22.1 cps/kBq	191.5 cps/kBq
Transverse resolution @ 1 cm	5-7 mm	4.1 mm	3 mm
Transverse resolution @ 10 cm	n/a	4.5 mm	~3.5 mm (@ acceptance angle 30°)
Axial resolution @ 10 cm	~5 mm (for WLS readout)	4.3 mm	~5 mm (@acceptance angle 30°)
Peak NECR	~400 kcps @40 kBq/cc (for 2 m AFOV)	646 kcps @ 52.8 kBq/cc with digital TOF regular phantom	1718 kcps @ 8.0 kBq/cc 175 cm phantom (diam. 20 cm)
Scatter fraction	34 – 36 %	31.6 %	35.1 %

TABLE 6.2: Comparison of the J-PET scanner to Philips Vereos and EXPLORER tomographs [88–92]

need in such a case addition of crystals, photomultipliers, channels, computing power or power supply what multiplies costs. Often such an extension is just impossible because of technical reasons. Additionally, in case of the Modular J-PET scanner, diameter of the detecting chamber may be adjusted by adding or removing modules, depending on imaging needs and size of the imaged patient.

J-PET detector assembly is light (e.g. single-layer gantry of 80 cm diameter and 50 cm AFOV weights ca. 60 kg). J-PET scanner works in room temperature with regular humidity and does not need any dedicated air-conditioning system. Also power requirements are low due to small amount of photomultipliers and signal processing units.

Having in mind all these advantages of the J-PET device over current solutions, one could ask: is this possible to achieve with the J-PET tomograph parameters that would allow the usage of the J-PET detector in medical applications? In order to answer this question, some performance characteristics of the J-PET scanner, commercial Philips Vereos tomograph and prototype EXPLORER device were summarized in Tab. 6.2.

System sensitivity of the J-PET is lower than in case of the total-body EXPLORER scanner but it is comparable to sensitivities of current commercial tomographs. It means that also the effective dose for a patient could be in range of typical values, which is

about 25 mSv for combined PET/CT measurement [100]. Further improvements of the detector sensitivity could even lead to the dose reduction [35].

Spatial resolution is on the order of 5 mm in each direction for the prototype with WLS strips. It is comparable with competitors and is enough for medical imaging. While scatter fraction is between 34 % and 36 % depending on detecting chamber geometry, value of the NECR peak is 3.2 times higher than for GE Discovery IQ, 2.2 times higher than for Siemens Biograph mCT, 2.5 times higher than for Philips Vereos PET/CT and 5.7 times smaller than for the EXPLORER device. However, it is obtained for typical value of activity concentration of about 40 kBq/cm^3.

To sum up, the J-PET technology allows to build the total-body PET scanner which has many advantages and has performance characteristics comparable to those obtained for both commercial and currently developed PET devices.

Chapter 7

Optimization of the J-PET detector

Designing and building the prototype of such a complex device, as the PET scanner, is associated with meticulous planning. However, before the first prototype, it is not possible to predict all problems that will occur and they must be rather successively solved with each next iteration of the device. In such an iterative process of the construction and working parameters optimization, many aspects have to be taken into account: the market research, theoretical calculations, experimental results and simulation studies. Final device should compromise between the widely understood efficiency and costs of building. In this chapter, some aspects of the J-PET scanner geometry and operating parameters optimization are presented. Also some directions of the further development are indicated.

7.1 Optimization of the construction

This section describes aspects concerning the materials selection, single module production and optimization of the detecting chamber geometry. All presented decisions concerning the materials, shapes, operating parameters, etc. were preceded by measurements, simulations and analyzes in which the whole J-PET team was involved.

7.1.1 Scintillators and photomultipliers

Two important factors that had to be accounted for before building the first prototype, was the material of scintillators and the model of photomultipliers. On the one hand, in order to maximize the amount of detected scintillation light, the emission spectrum of the scintillators and the quantum efficiency of the photomultipliers should overlap, as much as possible (the maximum of the emission spectrum should fall on the maximum of the quantum efficiency, see Fig. 2.6). On the other hand, also the time properties of the scintillators and prices of the components had to be taken into account.

For the construction of first prototypes the fast timing EJ-230 scintillators [97, 101] produced by the Eljen Technology company were chosen. These scintillators are optimized for applications where detector dimension exceeds 10 cm. However, for the last modular prototype, these scintillators were replaced with the ones with lower photon attenuation produced by the Saint-Gobain Crystals company.

While currently the BC-404 is the material with the best properties provided by this manufacturer, there is no major difference in relation to the BC-408 material [102, 103], which is more accessible. Even though the rising time of the BC-408 is lower than for the BC-404 (0.9 ns vs. 0.7 ns), effectively because of much lower light attenuation (380 cm) the BC-408 is the most optimal. Wavelength shifters for the Modular J-PET prototype were provided also by the Saint-Gobain Crystals company. Material of these WLS strips is BC-482A [103, 104].

Although in case of prototypes built so far commercially available scintillators were used, also technology of production of own scintillating materials for future versions of the J-PET scanner is developed [105–107]. It was shown that adding the wavelength shifter the composition of the polystyrene scintillator allows to minimize the decay time and maximize the light output of the scintillator. Optimal composition was found by maximizing the light output for fixed photomultipliers used in the prototype construction (in optimal situation emission spectrum of the scintillator and quantum efficiency dependence on wavelength should overlap as much as possible).

One company producing high-quality photomultipliers is Hamamatsu. Few models provided by this manufacturer were taken into account when first prototypes were built. The most important parameter was high quantum efficiency. The R4998 [108] model has

the highest efficiency but this photomultiplier is produced manually and for individual use, which is reflected in its high price. Instead of this model, the R9800 [109] one was used for the first prototype, as the much cheaper and serially produced replacement with very similar properties.

Although the R9800 photomultipliers have high quantum efficiency which allowed to prove the concept of the J-PET detector, they had also some flaws. Because of their size it was not possible to build the prototype with densely arranged scintillator strips. These detectors are also sensitive to magnetic field which makes impossible to use them in the solution combining PET and MRI techniques. Additionally, photomultiplier tubes must be powered with high voltage which complicates the construction and makes the device more expensive.

To eliminate above problems, silicon detectors were implemented in the last modular prototype. For the Modular J-PET scanner, matrices of 4 silicon photomultipliers were used as a single detector mounted at the end of each scintillator strip. Silicon photomultipliers from series S13361 [110] produced by Hamamatsu were chosen for the Modular J-PET device. These SiPMs exhibit high photon detection efficiency and are immune to magnetic field.

7.1.2 Single module

When first J-PET strip modules were developed, scintillators with many cross-sections and lengths were tested [111]. On the one hand, the bigger the cross-section of the scintillator, the higher probability of gamma photon detection. On the other hand, the wider the strip, the harder to determine exact position of interaction, which limits the angular resolution of the device. In classical PET devices cross-section of single crystal in direction perpendicular to the radius of the tomograph varies from 4 mm x 4 mm to 6.3 mm x 6.3 mm [31]. Because of that cuboid strips with width from 4 mm to 7 mm were taken into account.

Depth of the strip (size along the radius of the detector) in case of strips with rectangular cross-section is limited by the diameter of the photocathode of the photomultiplier tube attached to the strip. In case of the R4998 photomultipliers, the diameter of the photocathode is 20 mm. Because of that the diagonal of the rectangular cross-section

of the strip was limited to about 20 mm. Finally, after tests and simulations of strips with different cross-sections, the strips with cross-section 19 mm x 7 mm were chosen as optimal for the "big barrel" prototype.

Strip length of the "big barrel" prototype was set to 50 cm. For longer strips it would be hard to gain space and time resolutions for place of interaction detection along the strip allowing to get reasonable spatial resolution of the whole device. To solve this problem modular geometry of the Modular J-PET scanner with WLS strips was proposed. Attaching WLS strips to modules allowed to obtain resolution along the strip of 0.5 cm. Because of that in case of the Modular J-PET longer strips with length of 100 cm could be used.

In case of the Modular J-PET scanner, classical photomultipliers were replaced with silicon photodetectors. Size of single SiPM was 6 mm x 6 mm. As it was mentioned in previous section, at each end of the scintillator strip the matrix of 4 SiPMs was installed. It determined the shape of the cross-section of the scintillator strip to 6 mm x 24 mm. For the next prototypes scintillators with cross-section of 6 mm x 30 mm are considered. If such scintillators would be used, matrices of 5 SiPM detectors could be mounted to their ends. Moreover, usage of SiPM photodetectors simplifies design of the power supply system and opens perspectives for the combined PET/MRI measurements.

In all prototypes of the J-PET scanner, each scintillator was wrapped with the non-transparent foil to limit the escaping light and isolate the scintillators optically. Different types of foils were tested and finally the vikuiti foil was chosen as the best one [112]. Photomultipliers were glued to the strips with optically transparent glue.

7.1.3 Detecting chamber

The diameter and the length of the detecting chamber should be so as to contain the thorax and the head of the patient. Therefore, the region of the AFOV with high efficiency should be at least 1 m. To ensure that, total length of the scanner should be 1.4-2 m. Width of average patient is about 40 cm which means that the optimal diameter of the scanner should be 80-100 cm.

In case of the "big barrel" prototype, 192 single strip modules were organized in 3 layers containing, respectively, 48, 48 and 96 strips. Such a geometry was determined by the

sizes of the photomultiplier tube housings. One cannot put all strips in 1 layer one by one. However, even if this geometry would be somehow "flatten" to just one layer, still there would be no full angle coverage and there would be gaps between the subsequent scintillators.

As it was mentioned in previous sections, problem of physical size of PMT housings was solved by replacing photomultiplier tubes with silicon photomultipliers. Single modules were also organized into bigger modules containing few strips. Such a solution allowed to put all scintillators into just one layer, to minimize distances between subsequent strips and to obtain better angular coverage.

In the future also 2nd layer of such multi-strip modules could be added. Simulations show that the 2nd layer improves the sensitivity by a factor of 3 (Sec. 5.2.1). Adding next layer causes a further increase in sensitivity by the factor of about 2 in relation to double-layer geometry but it also complicates the mechanics of the device and increases costs. Because of that it seems that double-layer geometry is optimal for further prototypes.

7.2 Optimization of the operating parameters

The most important operating parameters of the J-PET scanner are the energy thresholds and the time window. These parameters are used to define the coincidence, which is crucial for any analyzes, especially when performance characteristics of the detector are calculated.

7.2.1 Fixed energy threshold

Why in previous chapters the value of 200 keV was used as the fixed energy threshold? Is this value optimal and minimizes the influence of the background from false coincidences? In order to find the answer, the following event may be considered: two scatterings originate from one photon: the primary Compton scattering and the secondary scattering (Fig. 7.1). Although such an event should be interpreted as the detector-scattered coincidence, it could be classified as the true coincidence if in both scatterings deposited energies would be bigger than the fixed energy threshold. In order to filter out such

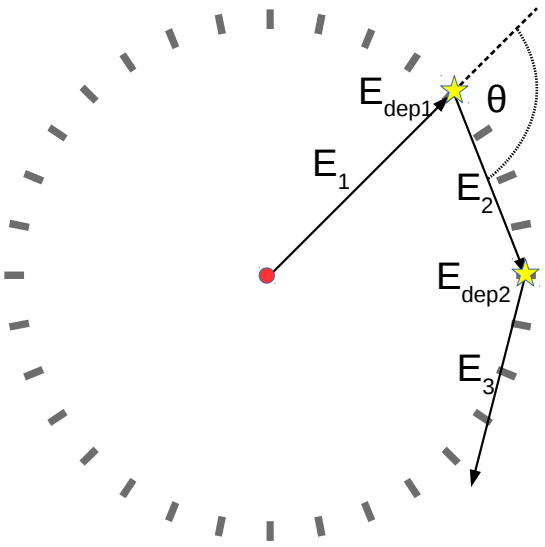

FIGURE 7.1: Visualization of the detector-scattered coincidence; E_1 - non-scattered gamma photon with energy 511 keV, E_2 - gamma photon after the primary scattering, E_3 - gamma photon after the secondary scattering, E_{dep1} - energy deposited in the primary scattering, E_{dep2} - energy deposited in the secondary scattering, θ - the angle of the primary scattering.

detector-scattered coincidences, the fixed energy threshold should be set to the value maximizing the number of primaries and minimizing the number of secondaries.

On the one hand, the smaller the fixed energy threshold E_{th}, the bigger number of primary coincidences taken into account in forming coincidences. If optimal value of the E_{th} exists, what should be the minimal value of the θ angle which would allow to deposit the energy E_{th}?

The Compton shift in the first scattering:

$$\frac{1}{E_2} - \frac{1}{E_1} = \frac{1}{m_e c^2}(1 - \cos\theta) \tag{7.1}$$

and

$$E_2 = E_1 - E_{dep1}, \tag{7.2}$$

where

$$E_{dep1} = E_1 - \left(\frac{1}{E_1} + \frac{1}{m_e c^2}(1 - \cos\theta)\right)^{-1} \geqslant E_{th} \tag{7.3}$$

is deposited energy. This leads to the following dependence:

$$\cos\theta \leqslant 1 - \frac{m_e c^2 E_{th}}{E_1(E_1 - E_{th})}. \tag{7.4}$$

For $0° \leqslant \theta \leqslant 180°$:

$$\theta_{min} = \arccos\left(1 - \frac{m_e c^2 E_{th}}{E_1(E_1 - E_{th})}\right) \tag{7.5}$$

On the other hand, there is a question, what should be the minimal energy of scattered gamma photon E_2, that would allow to deposit at least the energy E_{th} also in the second scattering?

The biggest part of energy E_{th} would be deposited in the second scattering, if there was a back scattering (to be easily seen from the Klein-Nishina formula). In other words, E_2 must at least enable deposition of energy E_{th} in back-scattering in the second hit ($E_{dep2} \geqslant E_{th}$).

$$\frac{1}{E_3} - \frac{1}{E_{2min}} = \frac{1}{m_e c^2}(1 - \cos(180°)) = \frac{2}{m_e c^2} \tag{7.6}$$

$$E_{2min} = E_{dep2} + E_3 \rightarrow E_3 = E_{2min} - E_{dep2} \tag{7.7}$$

If $E_{dep2} = E_{th}$, then we get:

$$E_{2min} = 0.5(E_{th} + \sqrt{E_{th}(E_{th} + 2m_e c^2)}) \tag{7.8}$$

If the photon's E_2 (after the first scattering) has at least such energy, then there may be second scattering if it is back-scattered. If the photon will scatter with the smaller angle, then the deposited energy will be smaller than the threshold, and the scattering will not be taken into account during forming the coincidence. Further on, the smaller the energy

E_{2min} – the better, because there is smaller chance to have the second scattering over the threshold.

At what minimal value of threshold E_{th} both hits are over the threshold (and form the detector-scattered coincidence)? From the first condition (Eq. 7.5), we have the biggest possible θ angle (the biggest energy deposited in first scattering E_{dep1} and the smallest energy of scattered photon E_2). If we want to have the second scattering (to produce the detector-scattered coincidence), then we need the highest possible value of energy E_2 (Eq. 7.8). These are two contradictory conditions. Because of that one can find the optimal value of the E_{th} to detect both hits. It will be the minimal value of the energy threshold, above which, such event is not possible. Compton shift equation for minimal value of energy after first scattering E_{2min} and minimal angle θ_{min} would be:

$$\frac{1}{E_{2min}} - \frac{1}{E_1} = \frac{1}{m_e c^2}(1 - cos(\theta_{min})) \tag{7.9}$$

In order to calculate the optimal energy threshold E_{th} one needs to put equations 7.5 and 7.8 to formula 7.9:

$$\frac{2}{E_{th} + \sqrt{E_{th}(E_{th} + 2m_e c^2)}} - \frac{1}{E_1} = \frac{E_{th}}{E_1(E_1 - E_{th})} \tag{7.10}$$

After some transformations we get the square equation with two solutions:

$$4E_{th}^2 - E_{th}(6E_1 + m_e c^2) + 2E_1^2 = 0 \tag{7.11}$$

$$\begin{aligned} E_{th} &= \frac{6E_1^2 + m_e c^2 \pm \sqrt{\Delta}}{8}, \\ \Delta &= (6E_1^2 + m_e c^2)^2 - 32E_1^2 \end{aligned} \tag{7.12}$$

After inserting the number values ($E_1 = 511\ keV$) we get:

$$E_{th1} \approx 184\ keV \tag{7.13}$$

$$E_{th2} \approx 711\ keV \tag{7.14}$$

Only the first solution is physical as the deposited energy may be not higher than the energy of the incident photon which is 511 keV. If we set the fixed energy threshold to 184 keV (or a little smaller) then it is possible to have 2 hits with energies at least E_{th} (which means that $E_{dep1,2} \geqslant E_{th}$). If we set the threshold to value higher than calculated threshold (for example 200 keV), then detector-scattered coincidences should be eliminated from the dataset.

7.2.2 Noise energy threshold

Noise energy threshold was introduced for studies of the coincidence definition when an optimal definition was searched for. In coincidence forming we allow to have in time window exactly two hits over the fixed energy threshold (see previous section) and $N-2$ additional hits with energies above the noise energy threshold and below the fixed energy threshold (see Sec. 3.2.1 and [84]). Introducing such a parameter was motivated by the a low experimental energy threshold of 10 keV which minimizes the background. Because of that it was also checked how it influences results and if it should be taken into account in analysis of simulation results.

In order to study this parameter, simulations of scatter fraction of the single-layer prototype were processed with different definitions of the coincidence. Simulation was performed for the single layer J-PET geometry with 50 cm strips and 85 cm diameter of the detecting chamber. Rates of subsequent types of coincidences were calculated (Fig. 7.2). Also rate of prompts and scatter fraction were obtained (Fig. 7.3).

For each type of coincidence, rate grows with the number of all hits N and with the value of energy threshold E_{th0}. If there would be only 2 hits above the fixed energy threshold and no hits with energies below this threshold, about 60 % of true coincidences would be lost. Increasing number of hits above the noise energy threshold increases also the rate of true coincidences to maximum level. Also other rates increase. While growth of phantom-scattered coincidence rate follows the growth of true coincidences rate, rates of detector-scattered and accidental coincidences remain at a negligible level. It seems that for $E_{th0} = 0\ keV$ (no noise energy threshold) and for $N = 8$ (6 additional hits)

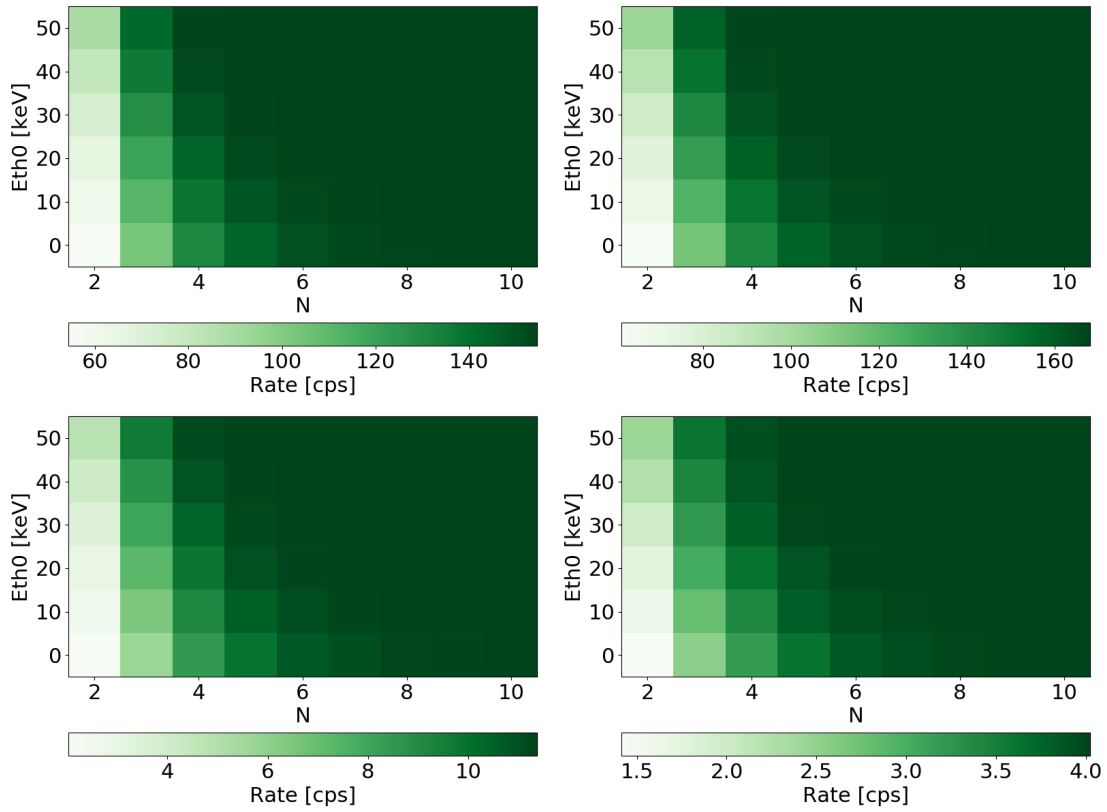

FIGURE 7.2: Rates of subsequent types of coincidences in function of the noise threshold of deposited energy and number of additional hits above the noise energy threshold and below the fixed energy threshold equal to 200 keV: (left-top) true, (right-top) phantom-scattered, (left-bottom) detector-scattered, (right-bottom) accidental. For true coincidences, the darker the cell the better. For other types of coincidences, the lighter the cell the better.

there is no further improvement in rates. It is caused by the fact that for a fixed time window of 3 ns there is negligible number of events with multiplicity higher than 8 [77]. Increasing the noise energy threshold also increases all rates but it seems that the effect is less visible than in case of increasing the number of additional hits.

Rate of prompt coincidences and scatter fraction presented in Fig. 7.3 may be treated as two figures of merit. On the one hand, to get the highest possible prompt coincidences rate, there should be high number of additional hits. On the other hand, to get the lowest scatter fraction, number of additional hits should be minimal. Taking into account these 2 contradictory conditions and their consequences we have decided to allow any number of additional hits with energy lower than the fixed energy threshold (the noise energy threshold is switched off). In such a solution we increase number of prompt coincidences by a factor of about 2.5, while the scatter fraction increases by about 2 % only in relation

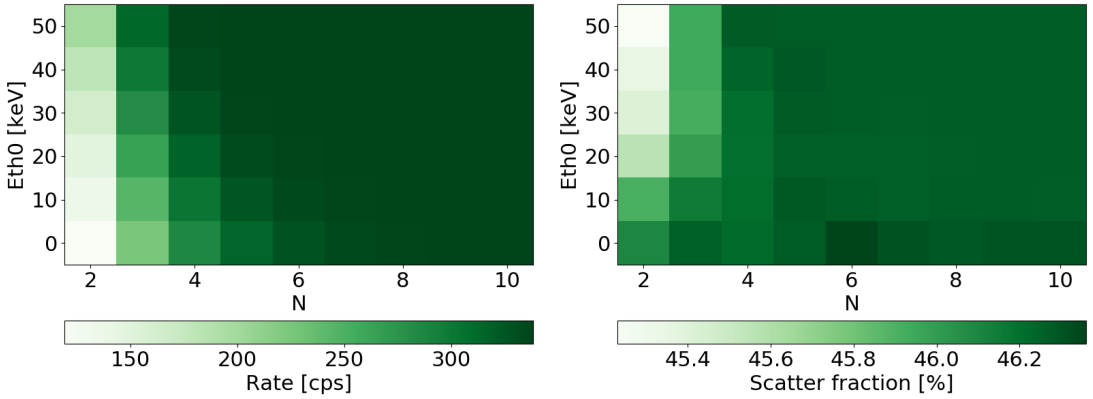

FIGURE 7.3: (left) prompt coincidences, (right) scatter fraction. For prompt coincidences, the darker the cell the better. For scatter fraction, the lighter the cell the better.

to the lowest possible value. Additionally, it simplifies the definition of a coincidence as much as possible, which facilitates further analyzes.

7.2.3 Time window

At first, it might seem that the time window should be dependent mainly on the size of the detecting chamber. We can think about worst situation when point of emission of back-to-back gamma photons would be located at the end of the diagonal of the longitudinal cross-section of the detecting chamber and the LOR would overlap with this diagonal. Then the time difference between two hits forming the coincidence would be the longest possible. For 50 cm AFOV and 80 cm diameter of the detecting chamber such a time difference would be about 3.15 ns. For the same diameter but 2 m AFOV such a time difference would be even 7.19 ns and could be treated as the upper limit of the time window.

On the other hand, in a typical situation during the measurement, the region of interest lies in the central area of the detecting chamber. It may be assumed that an average patient would fit in a cylinder of diameter of about 40 cm. Additionally, for LORs where the angle between the LOR and the axis of the scanner is smaller than 30°, there is very low probability that anything will be registered because of exponential attenuation in the patient body which means that the SNR worsens dramatically. Taking above assumptions into account we could calculate a maximal length difference along the LOR

in such a pessimistic situation, to be $\frac{40\ cm}{sin(30°)} = 80\ cm$. To "catch" such an event, the minimum value of the time window should be 2.67 ns.

Having both the upper and lower limits for the time window, it seems reasonable to set it closer to the lower limit. The narrower the time window, the smaller number of accidental coincidences registered. As long as the time window is even slightly wider than the lower limit, it should not affect the number of registered true coincidences. Because of that we use 3 ns time window for most of analyzes in the J-PET project.

7.3 Recommendations for further prototypes

Recommendations presented in this section base on both results of performance characteristics simulations described in Chap. 5 and aspects of optimization described in previous sections. In order to take into account all above figures of merit in process of designing the J-PET prototype, the compromise must be found between the geometrical acceptance, the background, the image quality and the production costs.

The best spatial resolutions were obtained for the 4 mm thick strips and the SiPM readout with additional layer of the WLS strips. The longer the strips, the higher the sensitivity, the higher the NECR peak (which is obtained for smaller value of the activity concentration) and the smaller the scatter fraction. On the other hand, without WLS strips, the axial resolution worsens with the growth of strips length. As the future J-PET prototypes are designed to base on both silicon photomultipliers and WLS strips, the cross-section of the strip should be a multiplication of the area of single SiPM photomultiplier. Currently, studies on scintillators with cross-section 6 mm x 30 mm are being performed. Matrices of 5 standard SiPMs could be attached to each end of such a scintillator strip.

Adding a second cylindrical layer of strips seems to have slight influence on the spatial resolution and the scatter fraction, but it strongly improves the sensitivity and the NECR characteristics. Increasing the diameter of the detecting chamber worsens the sensitivity of the scanner. It seems that from all tested geometries, the best results were obtained for the double-layer geometry built from strips with length of 200 cm and thickness of 4 mm, the diameter equal to 75 cm and the SiPM photomultipliers with the additional layer of the WLS strips used as a readout.

Chapter 8

Summary

Studies presented in this thesis cover verification of GATE simulations of the J-PET scanner with experimental data, estimation and analysis of the NEMA norms for the J-PET device and optimization of its geometry and operating parameters. The spatial resolution, the scatter fraction, the NECR and the sensitivity were estimated according to the NEMA norm as a function of the length of the tomograph, the number of the detection layers, diameter of the tomographic chamber and as a function of the applied type of readout.

The sensitivity profiles were estimated for four lengths of scintillator strips (20 cm, 50 cm, 100 cm and 200 cm), three diameters of detecting chamber (75 cm, 85 cm, 95 cm) and two thicknesses of scintillators (4 mm, 7 mm). The sensitivity grows with the length of scintillators and with the number of layers (it is bigger for double-layer geometries than for single-layer geometries). On the other hand, the larger the diameter of detecting chamber, the smaller the sensitivity.

For the double-layer geometry with diameter equal to 85 cm and 50-cm-long scintillator strips with 2 cm radial thickness, the sensitivity at the centre of the tomograph was about 6.6 cps/kBq, for 100 cm strips it exceeded 16.1 cps/kBq while for 200-cm-long strips it was 23.8 cps/kBq. Sensitivities of the double-layer J-PET scanners with 100 cm and 200 cm AFOV are in the range of typical values of modern commercial PET scanners.

For each geometry configuration, the spatial resolution was calculated for six different positions of point source inside the detecting chamber. All resolutions seem to be independent of the radial distance of source from the axis of the scanner. While tangential

and radial resolutions are independent of the length of the detecting strips, the axial resolution is better when shorter strips are used.

The spatial resolution is strongly dependent on the type of readout simulated. The shorter the CRT and axial position resolution, the better the PSF. However, for the WLS strips used in the latest Modular J-PET prototype, axial resolution is independent of the position along the axis of the scanner.

Simulations showed that when the silicon photomultipliers were used (for geometry with diameter of 85 cm, with strips of length 100 cm, thickness equal to 4 mm), the spatial resolution (PSF) in the centre of the scanner is about 3 mm (radial, tangential) and 20 mm (axial). If an additional layer of WLS would be used to improve the readout, the axial PSF would be 6 mm. It is comparable to values of currently used commercial PET scanners.

The values of scatter fraction are strongly dependent on the method used in order to calculate the characteristic. If the method based on the sinogram analysis was used, the scatter fraction was in the range of 34 % to 36 %. On the other hand, if the method based on true Monte Carlo was used, scatter fraction was in the range of 47 % to 52 %, depending on geometry. Obtained values of scatter fraction are similar to those computed and measured for commercial PET scanners.

Next characteristic from the NEMA norm is the NECR dependency. The NECR was obtained for geometries listed above for scatter fraction and for the same cylindrical phantom. The activity concentration ranges from 0 to about 90 kBq/cm^3. The simulations showed that the longer the strips, the higher value of NECR peak and in addition the longer the strip the smaller value of the activity concentration at which the value of NECR is maximal. The smaller the activity concentration, the smaller dose deposited in the patient's body and shorter recuperation.

The best results of NECR were obtained for double-layer geometry with 200 cm scintillator strips. The NECR peak for this geometry is equal to about 400 kcps and it was achieved at 40 kBq/cm^3.

All these characteristics have typical values. However, current studies show that there is a place for a significant improvement in reduction of the random background, which may give higher values of NECR peaks and finally images with higher qualities [113].

Studies presented in this thesis confirmed that the PET scanner based on the plastic scintillator strips, may achieve the NEMA characteristics comparable to those obtained for commercially used PET scanners. We believe that presented results may be improved. Next studies will be devoted to simulations of the total-body J-PET device and humanoid XCAT phantom. Also methods of image reconstruction will be developed with the GATE simulations.

Appendix A

Measurements of the absorption length dependence on light wavelength

According to data sheet supplied by the manufacturer, absorption length of EJ230 material is typically about 100 cm [97] and depends on the wavelength of transmitted photons. In order to check what is the spectrum of absorption length of the EJ230 material, measurements of 50-cm-long strip of EJ230 scintillator were performed.

The measuring setup consisted of the scintillator, the source of the UV radiation, the monochromator, the detector, the lock-in amplifier and the computer (Figs A.1, A.2). Scintillator had shape of 50 cm x 1.9 cm x 0.5 cm and was made of EJ230 polymer. One of its ends was put into the monochromator. Maximum of the emission spectrum of this scintillator was at 391 nm (emission spectrum of the scintillator is presented in Ref. [101]). The UV lamp model was *Dors 50* with emission maximum of 365 nm and power of 4 W [114] (the UV lamp for checking banknotes, see Fig. A.3a). The monochromator used in measurements was the *Newport 74125* device. It was controlled with the computer using the *CS260 Utility* application. Output of the monochromator was connected with the optical detector *Newport 71889_70316NS* (its gain was set to 10^6). Voltage signal outgoing from the detector was amplified with the lock-in amplifier *Stanford Research System SR530*, synchronized with the monochromator using generator of sinusoidal signals with frequency of 75 Hz (Fig. A.3b).

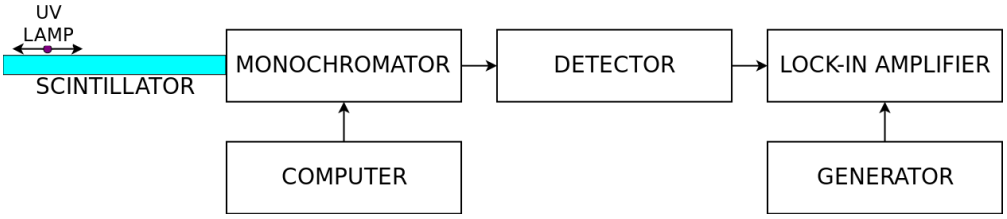

FIGURE A.1: Scheme of the measurement setup

FIGURE A.2: The measurement setup: 1) the scintillator, 2) the UV lamp, 3) the monochromator, 4) the detector, 5) the lock-in amplifier, 6) the computer to control the monochromator

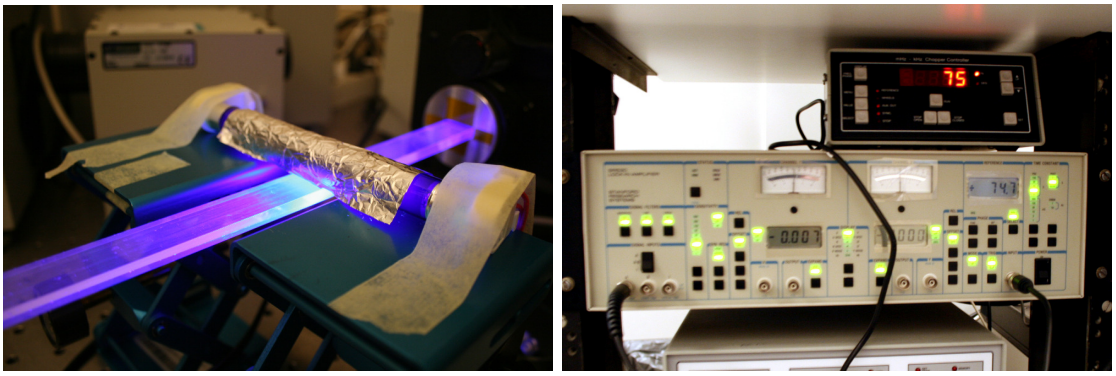

FIGURE A.3: Left - the UV lamp with the activated scintillator; right - the lock-in amplifier

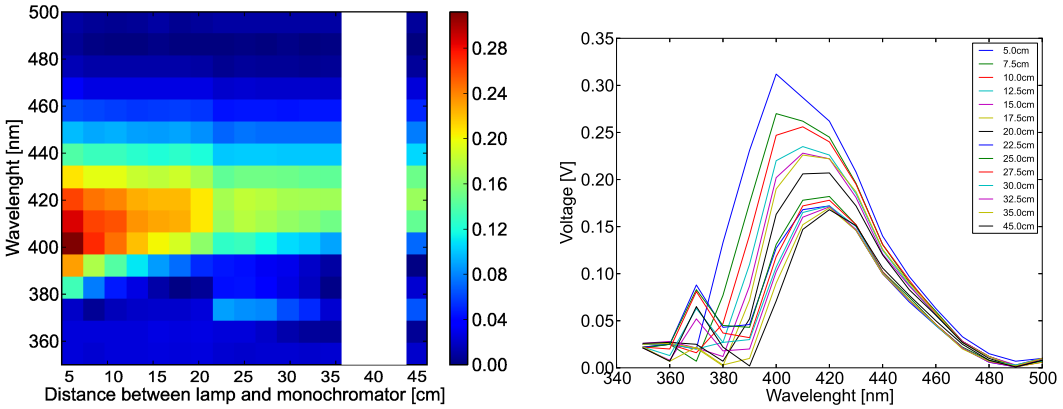

FIGURE A.4: Results of measurements: (left) values of pixels correspond to values of voltages measured using the lock-in amplifier (colour scale); white area corresponds to distances that were omitted; (right) one-dimensional spectra for each distance between the lamp and the monochromator. Measurements were done for 14 points, curves are to guide one's eye.

During the measurements, the source of UV radiation was moved along the scintillator in 2.5-cm-long steps. The distance between the lamp and the monochromator was changing from 5 cm to 45 cm. For each position of the lamp, the following measuring procedure was performed:

1. Wavelength of detected light was set using the monochromator controlled by the computer.
2. The voltage signal measured by the lock-in amplifier was acquired for about 30 s.
3. When value of measurement was stable, it was written down.

The procedure was repeated until the whole spectrum for a fixed position of lamp was acquired. Range of wavelengths of detected light was between 350 nm and 500 nm. Number of all measurements was 224 organized in 16 measurement series (16 spectra for different positions of the UV lamp). Each spectrum was measured for 14 different values of wavelengths. Results of these measurements are presented in Fig. A.4. Each column of the matrix presented in the left panel of Fig. A.4 is a spectrum for a fixed position. These spectra are presented as one-dimensional graphs in the right panel of Fig. A.4.

For each wavelength the dependence between the amplitude of the measured signal and the distance between the lamp and the monochromator was fitted with an exponential

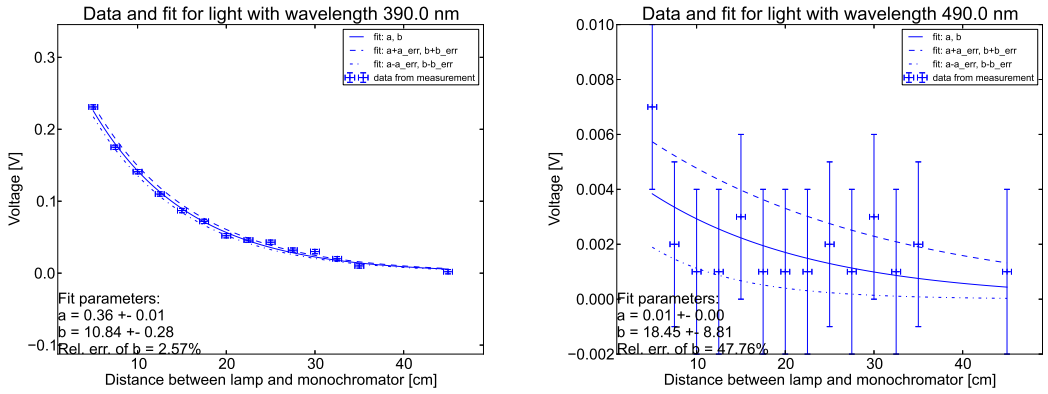

FIGURE A.5: Example dependencies U(d) for wavelengths 390 nm and 490 nm; error bars represent measurement uncertainties (details in text)

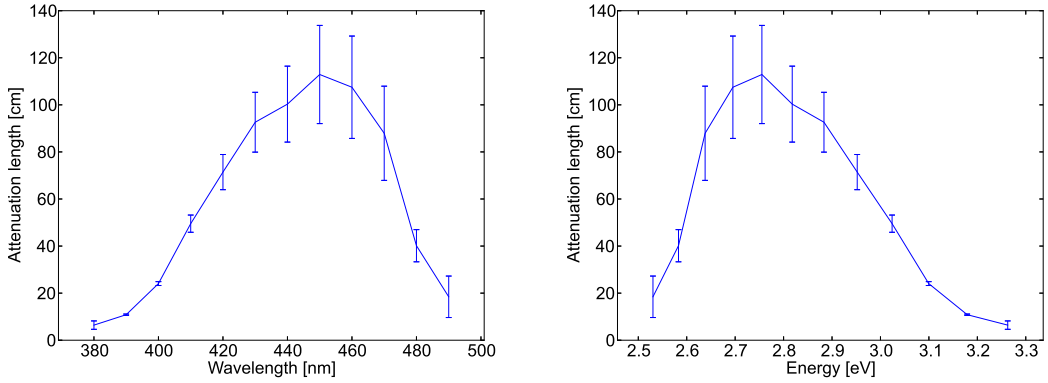

FIGURE A.6: Dependence of absorption length: (left) on wavelengths, (right) on energies of photons; error bars represent the standard deviation of the fitted absorption lengths

function[1] and the value of the absorption length b was calculated as the fit parameter (Fig. A.5). The fitting was performed using the *curve_fit* function from the *SciPy* package [115], taking into account measurement uncertainties (± 0.5 cm for distance and ± 3 mV for voltage).

Dependencies of the absorption length on wavelength and on energy of photons, are presented in Fig. A.6. Maximum of the spectrum is for photons with wavelength of 450 nm. Calculated value of absorption length for this wavelength is (112.9 $\pm$ 20.9) cm. Most photons generated and transmitted using the EJ230 scintillator have wavelengths in range of 390 nm and 400 nm. For photons with these wavelengths, calculated absorption length is about 20 cm.

[1]Exponential function used for fitting was: $a \cdot \exp(-x/b)$, where b is an absorption length.

The smallest error of fitting is for wavelength of 390 nm - (10.84 ± 0.28) cm (relative error is about 2.6%). Much worse is for higher wavelengths, like for 490 nm (Fig. A.5). It is caused by the fact that values of amplitudes of measured voltage signals were of the order of the device accuracy.

Appendix B

Software developed for the simulation study of the J-PET detector

Most of simulations performed for the purpose of the J-PET project were performed using the GATE [59, 60] software. GATE provides mechanisms to save simulation output to different formats and to cut the output with some thresholds (like the energy threshold). These mechanisms must be set before the simulation and they strongly affect the contents of the output data. For efficiency reasons, the analysis of simulated data was done independently, after recording these data.

For this purpose, I have developed the GATE Output J-PET Analyzer (GOJA). The GOJA software takes as the input the *.root output file of the GATE software and analyzes it to obtain the listmode file with the set of coincidences for further analysis. The *.root format is a special format of data used by the ROOT software [116]. Additionally, I have developed two wrappers for the GOJA software: the GOJA Manager and the Simulations Manager. While the GOJA is used to obtain coincidences from the single result file, the GOJA Manager manages the results from the single simulation. When the simulation is performed with the cluster using many processors, the output of the simulations consists of many *.root files. Finally, the Simulations Manager was developed to manage the sets of simulations, from generating them to analyzing their results with the GOJA Manager.

B.1 The GATE Output J-PET Analyzer

The GOJA takes the GATE output configured to contain only the *Hits* tree with full information about all hits (without any thresholds). Other trees, like the *Singles* or the *Coincidences*, may be disabled. The GOJA application reads the provided *.root file in its main loop and performs the pre-selection of all hits. Only interactions of the Compton-scattered gamma photons, which were not scattered with the Rayleigh scattering before and in which the energy deposited is bigger than the noise energy threshold, are taken into account in further processing. After the pre-selection stage, the set of hits is sorted by the time of interaction or by the ID of event, depending on the method of events forming. Events may be formed using both the time-window method and the true Monte Carlo method. Methods of events forming may be switched using the command line interface of the GOJA application (option *–sep*).

Both methods are performed in the second loop, that iterates over all pre-selected and sorted hits. Building up of the event starts with the first hit with energy deposited higher than the fixed energy threshold (200 keV). In the time window method, this first hit opens the time window. All hits fitting in the time window are added to the event. Forming of the event stops when the time window is exceeded. In the true Monte Carlo method, ID of the event is taken into account. All hits with the same event ID as the first hit are added to the event. Forming of the event stops when the event ID of the hit differs from the event ID of the first collected hit. When the event is formed and number of hits with energy deposited higher than the fixed energy threshold in the time window is at least 2, the coincidence is formed and printed to the output (Lst. B.1).

```
vector<Hit> event;
int start_window_eventID = 0;
double start_window_time = 0.;
for (unsigned int i=0; i<hits.size(); i++) {
  auto hit = hits[i];
  if(DEBUG) cout << "hit.edep=" << hit.edep << "\thit.time=" << hit.time <<
    "\tstart_window_time=" << start_window_time << "\thit.eventID=" << hit.eventID << endl;
  if (event.size()==0) {
    if (hit.edep>COMPTON_E_TH) {
      event.push_back(hit); // start forming the event with the hit with edep>E_TH
      start_window_time = hit.time;
      start_window_eventID = hit.eventID;
      lr.counter_compton_hits_over_the_ETH += 1;
    }
```

```
    }
    else {
      bool hit_in_event;
      if (EVENTS_SEPARATION_USING_TIME_WINDOW)
        hit_in_event = (hit.time-start_window_time)<TIME_WINDOW;
      else if (EVENTS_SEPARATION_USING_IDS_OF_EVENTS)
        hit_in_event = hit.eventID==start_window_eventID;
      if (hit_in_event) { // if the current hit belongs to the current event
        event.push_back(hit); // then it is added to the current event
      }
      else { // if the current hit does not belong to the current event
        lr.multiplicities.push_back(event.size());
        if (event.size()>=2) { // if the number of hits in the current event is at least 2
          EventAnalysis ea;
          ea.analyze_event(event); // then the current event is analyzed
        }
        event.clear(); // the current event is destroyed
        if (hit.edep>COMPTON_E_TH) { // start forming the event with the hit with edep>E_TH
          event.push_back(hit);
          start_window_time = hit.time;
          start_window_eventID = hit.eventID;
          lr.counter_compton_hits_over_the_ETH += 1;
        }
      }
    }
  }
  // the last event
  if (event.size()>=1) {
    lr.multiplicities.push_back(event.size());
    if (event.size()>=2) { // if the number of hits in the last event is at least 2
      EventAnalysis ea;
      ea.analyze_event(event); // then the last event is analyzed
    }
    event.clear(); // the last event is destroyed
  }
```

LISTING B.1: After the pre-selection stage, the GOJA application iterates over all collected hits. Events are formed and analyzed. Full sources of the GOJA application (and the GOJA Manager) are available online with the GitHub: `https://github.com/JPETTomography/j-pet-gate-tools/tree/master/goja`.

Next lines of the GOJA output are the subsequent coincidences obtained from the analysis. Next columns of the GOJA output listmode file contain the following data:

1. X coordinate of the position of the 1st hit in cm,

2. Y coordinate of the position of the 1st hit in cm,
3. Z coordinate of the position of the 1st hit in cm,
4. time of the 1st hit in ns,
5. X coordinate of the position of the 2nd hit in cm,
6. Y coordinate of the position of the 2nd hit in cm,
7. Z coordinate of the position of the 2nd hit in cm,
8. time of the 2nd hit in ns,
9. volumeID of the 1st hit,
10. volumeID of the 2nd hit,
11. deposited energy of the 1st hit keV,
12. deposited energy of the 2nd hit keV,
13. type of the coincidence (1 - true, 2 - phantom-scattered, 3 - detector-scattered, 4 - accidental),
14. X coordinate of the source position of the 1st hit in cm,
15. Y coordinate of the source position of the 1st hit in cm,
16. Z coordinate of the source position of the 1st hit in cm,
17. X coordinate of the source position of the 2nd hit in cm,
18. Y coordinate of the source position of the 2nd hit in cm,
19. Z coordinate of the source position of the 2nd hit in cm.

In the first 4 columns of the GOJA output, the position and the time of the 1st hit is saved. Next 4 columns contain analogous information about the second hit. 9th and 10th columns are identifiers of the scintillators, while 11th and 12th are energies deposited in the 1st and in the 2nd interactions. 13th column contains information about the type of the coincidence (the classification algorithm is presented in Lst. B.2). Next 3 columns are the source position coordinates of the 1st hit, while the last 3 ones contain the source position of the 2nd hit.

```
EventType t = kUnspecified;
if (h1.eventID==h2.eventID) { //true, phantom-scattered and detector-scattered
  if (h1.nPhantomCompton==0 and h2.nPhantomCompton==0) {
    if (h1.nCrystalCompton==1 and h2.nCrystalCompton==1) { //true
      t = kTrue;
    }
    else { //detector-scattered
      t = kDetectorScattered;
    }
  }
  else { //phantom-scattered
    t = kPhantomScattered;
  }
}
else { //accidental
  t = kAccidental;
}
```

LISTING B.2: The algorithm that classifies the coincidences by types (part of the GOJA software).

The GOJA software saves also information about the real simulated time of the performed simulation and some additional statistics. Real simulated time is calculated as the difference between the times of the last and the first hits in the whole *.root file. It seems that it should be always equal to the time set in the main macro of the GATE simulation but when the simulation is stopped because of the time limit of the cluster queue or just by the cluster administrator, the real simulated time is shorter than the time set in the main macro. Additional statistics contain information about the number of all Compton scatterings in the analyzed *.root file and numbers of hits over the noise and the fixed energy thresholds.

B.2 The GOJA Manager

The GOJA Manager is the python script with the command line interface, that allows to run the single GATE simulation and analyze its results with the GOJA application. It provides several modes, like: *run*, *analyze* and *concatenate* (full list of modes is available after typing *goja_manager.py –help* in the command line). The *run* mode allows to execute the simulation on the local machine or on the CIŚ computing cluster. On the local machine, jobs are executed one by one, while on the cluster, jobs are run in

parallel using the queue system. The *analyze* mode starts the analysis for each result *.root file separately. In this mode three output files per each *.root file are generated: outputX_coincidences, outputX_realtime and outputX_statistics (where X is the number of the job). For example, if the simulation was split into 100 jobs, there would be 100 output *.root files from the GATE software, 100 outputX_coincidences files from the GOJA software, etc.

After the analysis step, the GOJA results may be concatenated to three summary result files (default names of final result files after the concatenation step are: simulation_COINCIDENCES, simulation_REALTIME and simulation_STATISTICS; 'simulation' prefix may be adjusted with the *–simulation-name* option). Also the coincidence parameters, like the time window or the energy thresholds may be adjusted with the command line options. Obtained result files may be used in further calculations.

B.3 The Simulations Manager

The Simulations Manager is the tool written in python, that uses the GOJA Manager (and indirectly also the GOJA application) but provides also other useful functionalities[1]. Modes provided by the Simulations Manager are all modes from the GOJA Manager and also the following ones: *init*, *calibrate*, *aggregate*, *calculate* and *plot* (full list of modes and options is available after typing *simulations_manager.py –help* in the command line). Additionally, the manager allows to configure geometries set (with the option *–geometries-set*), like: *jpet*, *djpet* and *djpet-total-body*. Also the simulations set may be configured with the option *–simulations-set* (example simulations sets are: *nema*, *maps*). Both geometries set and simulations set may be filtered out with two regular expression filters (provided with options *–geometries-filter* and *–simulations-filter*).

In order to gain the benefits of the Simulations Manager, one needs to use the *init* mode first. In this mode, in the *SIMULATIONS* catalogue (that is automatically created in the Simulations Manager directory), the set of simulation macros for each geometry and for each simulation is generated. Each simulation consists of the main macro and the macros with the geometry (the geometry macros are generated with the dedicated python classes), the source, the phantom (if occurs), the physics macro, some material

[1]Sources available online with the GitLab: `https://gitlab.com/J-PET/j-pet-gate-tools-private/-/tree/master/python_scripts/simulations_manager`.

data files and cluster configuration files. When the simulation is initialized, the time of simulation is estimated to obtain few thousand of coincidences in the resulting GOJA output file. Also the simulation is set to only one job.

After the initialization, the *run* mode must be executed. This mode starts the GATE simulation. When the simulation is finished, the *analyze* and the *concatenate* modes must be performed. After these steps, the user gets the listmode GOJA output file with the limited set of coincidences. Having these initial results, the user may calibrate the simulations to get the desired number of coincidences per each simulation. For example, in case of the NEMA characteristics simulations, the final number of coincidences is taken from the NEMA norm and hardcoded in the sources of the Simulations Manager. However, it is possible to set the desired number of coincidences with the dedicated option *–nr-of-coincidences*.

In the *calibrate* mode, the time of each simulation from the chosen simulations set is rescaled proportionally to obtain the desired number of coincidences in the final GOJA output listmode file. Additionally, the number of splits may be set with the option *–nr-of-splits*. By default, it is set to 2000, which is the maximum number of jobs for a single user for the *i3d* queue on the CIŚ cluster (the maximum number of jobs is used to minimize the time of simulations).

After the calibration, the simulations must be runned, analyzed and concatenated again. Having concatenated results, one may aggregate them to the *Aggregated* subdirectory and perform further calculations with them. For example, in case of the *nema* simulations set, all NEMA norms are calculated and saved to the *Results* subdirectory. Some results obtained with these calculations may be also visualised with the *plot* mode. The example usage of the Simulations Manager tool is presented in Lst. B.3. The presented workflow allows to obtain some of results presented in 5th chapter of this thesis. The Simulations Manager may be extended straightforwardly to provide new sets of simulations or geometries and new modes of analysis.

```
simulations_manager.py -m init -ss nema -gs jpet
simulations_manager.py -m run -ss nema -gs jpet
simulations_manager.py -m analyze -ss nema -gs jpet
simulations_manager.py -m concatenate -ss nema -gs jpet
simulations_manager.py -m calibrate -ss nema -gs jpet
simulations_manager.py -m run -ss nema -gs jpet
simulations_manager.py -m analyze -ss nema -gs jpet
```

```
simulations_manager.py -m concatenate -ss nema -gs jpet
simulations_manager.py -m aggregate -ss nema -gs jpet
simulations_manager.py -m calculate -ss nema -gs jpet
simulations_manager.py -m plot -ss nema -gs jpet
```

LISTING B.3: Example usage of the Simulations Manager tool (details in the text). The parameter *-ss* is the short version of the *–simulations-set* parameter, while the *-gs* replaces the *–geometries-set* parameter. The Simulations Manager is available at the Gitlab service: repo `https://gitlab.com/J-PET/j-pet-gate-tools-private`, subdirectory *python_scripts/simulations_manager*.

Appendix C

Smearing simulation results

The three-layer prototype of the J-PET scanner consists of strips with single photomultipliers attached to their ends. Such a construction does not allow to measure exact position of the gamma-photon interaction in the plane perpendicular to the axis of the scanner. There are some studies covering measurements of the depth of interaction (DOI) but in current solution only the strips may be identified. Because of that, strips centers (in the x-y plane) are taken for the reconstruction. Also the position of interaction along the strip (z coordinate) and the time may be measured with the finite resolution. On the other hand, the GATE software provides exact positions of hits and exact times of interactions. In order to imitate the detector behaviour, the simulated x and y coordinates are moved to the strips centers, while the z coordinate and the time are smeared with the experimental resolutions.

C.1 Coordinates x and y

When the GATE simulation is performed, the GATE numbers all sensitive detectors (in this case the scintillators) with integer identifiers. Unfortunately, the numbering of the detecting volumes is not intuitive and not always strips are numbered consecutively (especially for multi-layer or modular geometries). Fortunately, the numbering algorithm is deterministic, which means that for the fixed geometry, the fixed identifier always refers to the same detector in all simulations performed for this geometry. Because of that, having the mapping between the strips identifiers and the strips centers, one may take

the smeared (or rather aligned) coordinates from the table (file) instead of recalculating it for each hit.

In order to prepare the mapping, the below algorithm was developed:

1. The coordinates of the strips centers are calculated analytically.
2. Having the coincidences set (for example for the simulation of the point source, simulated in the center of the detecting chamber), the algorithm searches for the hits that are no further than the half of the thickness of the strip from the analytically calculated strips centers (to guarantee that the hits have the same strip center calculated analytically).
3. For selected hits, their identifiers are checked.
4. The algorithm stops when coordinates of strips' centers for all strips are found.

In order to validate the algorithm also the average position of all hits is calculated. Then having the visualisation, one may judge if the algorithm works properly. In Fig. C.1 there is a simple visualisation of the algorithm with some additional explanations.

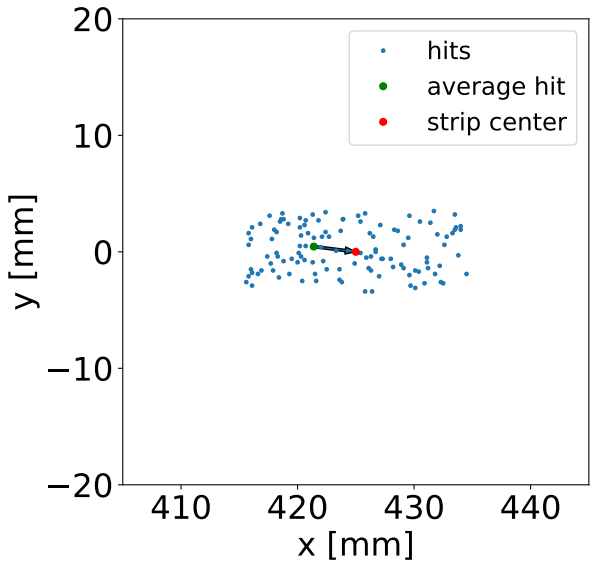

FIGURE C.1: Visualisation of interactions from the chosen scintillator in the x-y plane (1st scintillator from the inner layer of the 192-strip three-layer geometry). Blue dots are the single hits. Green dot is the average position of all hits in the strip. Red dot is the strip center calculated analytically. The arrow shows symbolically (on the example of the average hit) how the coordinates are aligned to the strips centers.

C.2 Coordinate z and time

When the x and y coordinates were only aligned to the strips' centers, the z position and the time were smeared with the *SmearEvents* application written by Roman Shopa which is available at: `https://github.com/JPETTomography/j-pet-gate-tools/tree/master/goja-tools/smear-events`. The tool iterates GOJA list mode output file line by line and smears positions z and times of both hits. Smearings are generated using normal distributions with experimental or simulated standard deviations (values of smearings for used types of readouts are presented in Sec. 3.1.2) and added to smeared positions and times. If the smeared z position is out of range of the AFOV, an event is filtered out and omitted in further analysis.

Bibliography

[1] Boss A. et al. Hybrid PET/MRI of intracranial masses: initial experiences and comparison to PET/CT. *Journal of Nuclear Medicine*, 51(8):1198–1205, 2010.

[2] Vandenberghe S. et al. Recent developments in time-of-flight PET. *European Journal of Nuclear Medicine and Molecular Imaging Physics*, 3:3, 2016.

[3] United States Department of Energy Office of Biological and Environmental Research. *A Vital Legacy: Biological and Environmental Research in the Atomic Age*. Ernest Orlando Lawrence Berkeley National Laboratory, 1997.

[4] Jones T. and Townsend D. W. History and future technical innovation in positron emission tomography. *Journal of Medical Imaging*, 4(1):011013, 2017.

[5] Vandenberghe S., Moskal P. and Karp J. S. State of the art in total body pet. *European Journal of Nuclear Medicine and Molecular Imaging Physics*, 7(1):1–33, 2020.

[6] Badawi R. D. et al. First human imaging studies with the EXPLORER total-body PET scanner. *Journal of Nuclear Medicine*, 60(3):299–303, 2019.

[7] Karp J. S. et al. Pennpet explorer: Design and preliminary performance of a whole-body imager. *Journal of Nuclear Medicine*, 61(1):136–143, 2020.

[8] Moskal P. et al. Novel detector systems for the positron emission tomography. *Bio-Algorithms and Med-Systems*, 7:73–78, 2011.

[9] Moskal P., ..., Kowalski P. et al. Time resolution of the plastic scintillator strips with matrix photomultiplier readout for J-PET tomograph. *Physics in Medicine and Biology*, 61:2025–2047, 2016.

[10] Niedźwiecki Sz., ..., Kowalski P. et al. J-PET: A new technology for the whole-body PET imaging. *Acta Physica Polonica B*, 48(10):1567, 2017.

[11] Leo W. R. *Techniques for nuclear and particle physics experiments: a how-to approach*. Springer-Verlag Berlin Heidelberg, 1987.

[12] Szymański K., ..., Kowalski. P. et al. Simulations of γ quanta scattering in a single module of the J-PET detector. *PBio-Algorithms and Med-Systems*.

[13] Moskal P. et al. Positronium in medicine and biology. *Nature Reviews Physics*, 1 (9):527–529, 2019.

[14] Moskal P., ..., Kowalski P. et al. Feasibility study of the positronium imaging with the J-PET tomograph. *Physics in Medicine and Biology*, 64, 2019.

[15] Ayden J. and Nourafchan L. Radiological engineering in brain dysfunction imaging processes and neuro informatics. *Journal of nuclear medicine and radiation therapy*, 2013.

[16] Beyer T. et al. The future of hybrid imaging – part 2: PET/CT. *Insights into imaging*, 2(3):225–234, 2011.

[17] Gelman A. et al. Statistical analysis of a medical imaging experiment. *Technical Report, Department of Statistics, University of California*, 349, 1992.

[18] Ramachandran G. N. and Lakshminarayanan A. V. Three-dimensional reconstruction from radiographs and electron micrographs: application of convolutions instead of Fourier transforms. *Proceedings of the National Academy of Sciences*, 68(9):2236–2240, 1971.

[19] Słomski A., ..., Kowalski P. et al. 3D PET image reconstruction based on the maximum likelihood estimation method (MLEM) algorithm. *Bio-Algorithms and Med-Systems*, 10(1):1–7, 2014.

[20] Thielemans K. et al. STIR: software for tomographic image reconstruction release 2. *Physics in Medicie and Biology*, 57:867, 2012.

[21] Moskal P., ..., Kowalski P. et al. Test of a single module of the J-PET scanner based on plastic scintillators. *Nuclear Instruments and Methods in Physics Research A*, 764:317–321, 2014.

[22] Moskal P., ..., Kowalski P. et al. A novel method for the line-of-response and time-of-flight reconstruction in TOF-PET detectors based on a library of synchronized model signals. *Nuclear Instruments and Methods in Physics Research A*, 775: 54–62, 2015.

[23] Moskal P., ..., Kowalski P. et al. J-pet: A novel TOF-PET detector based on plastic scintillators. *IEEE Xplore: Nuclear Science Symposium, Medical Imaging Conference and Room-Temperature Semiconductor Detector Workshop*, 2016. doi: 10.1109/NSSMIC.2016.8069617.

[24] Moses W. W. and Derenzo S. E. Prospects for time-of-flight PET using LSO scintillator. *IEEE Transactions on Nuclear Science*, 46:474–478, 1999.

[25] Moses W. W. Time of flight in PET revisited. *IEEE Transactions on Nuclear Science*, 50:1325–1330, 2003.

[26] Humm J. L., Rosenfeld A. and Del Guerra A. From PET detectors to PET scanners. *European Journal of Nuclear Medicine and Molecular Imaging*, 30:1574–1597, 2003.

[27] Townsend D. W. Physical principles and technology of clinical PET imaging. *ANNALS Academy of Medicine Singapore*, 33:133–145, 2004.

[28] Karp J. S. et al. Benefit of time-of-flight in PET: Experimental and clinical results. *Journal of Nuclear Medicine*, 49:462–470, 2008.

[29] Conti M. State of the art and challenges of time-of-flight PET. *Physica Medica*, 25:1–11, 2009.

[30] Conti M. Focus on time-of-flight PET: the benefits of improved time resolution. *European Journal of Nuclear Medicine and Molecular Imaging*, 38:1147–1157, 2011.

[31] Słomka P. et al. Recent advances and future progress in PET instrumentation. *Seminars in Nuclear Medicine*, 46:5–19, 2016.

[32] Viswanath V. et al. Development of PET for total-body imaging. *Acta Physica Polonica B*, 48(10):1555–1566, 2017.

[33] Zhang X. et al. Quantitative image reconstruction for total-body PET imaging using the 2-meter long EXPLORER scanner. *Physics in Medicine and Biology*, 62:2465, 2017.

[34] Cherry S. R. et al. Total-body imaging: Transforming the role of positron emission tomography. *Science Translational Medicine*, 9, 2017.

[35] Cherry S. R. et al. Total-body PET: Maximizing Sensitivity to Create New Opportunities for Clinical Research and Patient Care. *The Journal of Nuclear Medicine*, 59(1):3–12, 2018.

[36] Moskal P. and Stępień E. Ł. Prospects and clinical perspectives of total-body PET imaging using plastic scintillator. *PET Clinics 2020, in print.*

[37] Raczyński L., ..., Kowalski P. et al. Novel method for hit-position reconstruction using voltage signals in plastic scintillators and its application to positron emission tomography. *Nuclear Instruments and Methods in Physics Research A*, 764:186–192, 2014.

[38] Raczyński L., ..., Kowalski P. et al. Compressive sensing of signals generated in plastic scintillators in a novel J-PET instrument. *Nuclear Instruments and Methods in Physics Research A*, 786:105–112, 2015.

[39] Pałka M., ..., Kowalski P. et al. Multichannel FPGA based MVT system for high precision time (20ps RMS) and charge measurement. *Journal of Instrumentation*, 12:P08001, 2017.

[40] Korcyl G., ..., Kowalski P. et al. Sampling FEE and trigger-less DAQ for the J-PET scanner. *Acta Physica Polonica B*, 47:492–496, 2016.

[41] Korcyl G., ..., Kowalski P. et al. Evaluation of Single-Chip, Real-Time Tomographic Data Processing on FPGA - SoC Devices. *IEEE Transactions on Medical Imaging*, 2018. doi: 10.1109/TMI.2018.2837741. URL `https://doi.org/10.1109/tmi.2018.2837741`. in print.

[42] Sharma N. G., ..., Kowalski P. et al. Hit-time and hit-position reconstruction in strips of plastic scintillators using multi-threshold readouts. *IEEE Transactions on Radiation and Plasma Medical Sciences*, 2020.

[43] Krzemień W., ..., Kowalski P. et al. Analysis framework for the J-PET scanner. *Acta Physica Polonica A*, 127:1491–1494, 2015.

[44] Krzemień W. et al. J-PET Framework: Software platform for PET tomography data reconstruction and analysis. *SoftwareX*, 11:100487, 2020.

[45] Olcott P. D. and Levin C. S. Pulse width modulation: A novel readout scheme for high energy photon detection. In *2008 IEEE Nuclear Science Symposium Conference Record*, pages 4530–4535. IEEE, 2008.

[46] Sharma S., ..., Kowalski P. et al. Estimating relationship between the time over threshold and energy loss by photons in plastic scintillators used in the J-PET scanner. *European Journal of Nuclear Medicine and Molecular Imaging Physics*, 7(1):1–15, 2020.

[47] Moskal P. J-PET: Towards total-body modular PET from plastic scintillators. 2018. Invited talk at *Total Body PET - From Mice to Men*, Ghent 2018.

[48] Smyrski J., ..., Kowalski P. et al. Measurement of gamma quantum interaction point in plastic scintillator with WLS strips. *Nuclear Instruments and Methods in Physics Research A*, 851:39–42, 2017.

[49] Moskal P., ..., Kowalski P. et al. Performance assessment of the 2-gamma positronium imaging with the total-body PET scanners. *arXiv preprint arXiv:1911.06841*, 2019.

[50] Jasińska B., ..., Kowalski P. et al. Human tissue investigations using PALS technique - free radicals influence. *Acta Physica Polonica A*, 132(5):1556, 2017.

[51] Jasińska B., ..., Kowalski P. et al. Human tissues investigation using PALS technique. *Acta Physica Polonica B*, 48(10):1737, 2017.

[52] Dulski K., ..., Kowalski P. et al. Analysis procedure of the positronium lifetime spectra for the J-PET detector. *Acta Physica Polonica A*, 132(5):1637, 2017.

[53] Dulski K., ..., Kowalski P. et al. Commissioning of the J-PET detector in view of the positron annihilation lifetime spectroscopy. *Hyperfine Interactions*, 239(1):40, 2018.

[54] Gajos A., ..., Kowalski P. et al. Feasibility study of the time reversal symmetry tests in decays of metastable positronium atoms with the J-PET detector. *ArXiv e-prints*, April 2018.

[55] Mohammed M., ..., Kowalski P. et al. A method to produce linearly polarized positrons and positronium atoms with the J-PET detector. *Acta Physica Polonica A*, 132(5):1486, 2017.

[56] Kowalski P. et al. Moskal P., ... Feasibility studies of the polarization of photons beyond the optical wavelength regime with the J-PET detector. *The European Physical Journal C*, 78(11):970, 2018.

[57] Raj J., ..., Kowalski P. et al. A feasibility study of the time reversal violation test based on polarization of annihilation photons from the decay of ortho-positronium with the J-PET detector. *Hyperfine Interactions*, 239(1):56, 2018.

[58] Krawczyk N. ..., Kowalski P. et al. Simulation studies of annihilation-photon's polarisation via Compton scattering with the J-PET tomograph. *Hyperfine Interactions*, 240(1):81, 2019.

[59] Jan S. et al. GATE: a simulation toolkit for PET and SPECT. *Physics in Medicie and Biology*, 49:4543–4561, 2004.

[60] Jan S. et al. GATE v6: a major enhancement of the GATE simulation platform enabling modelling of CT and radiotherapy. *Physics in Medicie and Biology*, 56: 881–901, 2011.

[61] Sarrut D. et al. A review of the use and potential of the gate monte carlo simulation code for radiation therapy and dosimetry applications. *Medical Physics*, 41(6 Part 1), 2014.

[62] Ferrari A. et al. FLUKA: A multi-particle transport code (Program version 2005). Technical report, 2005.

[63] Böhlen T. T. et al. The FLUKA code: developments and challenges for high energy and medical applications. *Nuclear Data Sheets*, 120:211–214, 2014.

[64] Vlachoudis V. FLUKA Medical Simulations, 2015-05-20. URL `https://indico.cern.ch/event/395106/contributions/938969/attachments/791238/1084580/Lithuania_Minister_of_Health_2015.pdf`.

[65] Robert C. et al. Distributions of secondary particles in proton and carbon-ion therapy: a comparison between GATE/Geant4 and FLUKA Monte Carlo codes. *Physics in Medicine and Biology*, 58(9):2879, 2013.

[66] Sølie J. R. et al. A comparison of proton ranges in complex media using GATE/Geant4, MCNP6 and FLUKA. *arXiv preprint arXiv:1708.00668*, 2017.

[67] Agostinelli S. et al. Geant4 - a simulation toolkit. *Nuclear Instruments and Methods in Physics Research A*, 506:250–303, 2003.

[68] Allison J. et al. Geant4 developments and applications. *IEEE Transactions on Nuclear Science*, 53(1):270–278, 2006.

[69] Allison J. et al. Recent developments in geant4. *Nuclear Instruments and Methods in Physics Research Section A*, 835:186–225, 2016.

[70] Casella C. et al. A high resolution TOF-PET concept with axial geometry and digital SiPM readout. *Nuclear Instruments and Methods in Physics Research A*, 736:161–168, 2014.

[71] Gillam J. E. et al. Sensitivity recovery for the AX-PET prototype using inter-crystal scattering events. *Physics in Medicine and Biology*, 59:4065–4083, 2014.

[72] Solevi P. et al. AX-PET: from demonstrator towards a full-ring brain scanner. *Acta Physica Polonica A*, 127:1462–1464, 2015.

[73] Segars W. P. et al. 4D XCAT phantom for multimodality imaging research. *Medical Physics*, 37:4902–4915, 2010.

[74] Geant4 Collaboration. Geant4 - physics reference manual. 2016. URL `http://geant4.web.cern.ch/geant4/UserDocumentation/UsersGuides/PhysicsReferenceManual/fo/PhysicsReferenceManual.pdf`. 2018-03-29.

[75] Ivanchenko V. and Incerti S. Geant4 standard and low energy electromagnetic libraries. In *EPJ Web of Conferences*, volume 142, page 01016. EDP Sciences, 2017.

[76] Kowalski P. et al. Scatter fraction of the J-PET tomography scanner. *Acta Physica Polonica B*, 47:549–560, 2016.

[77] Kowalski P. et al. Multiple scattering and accidental coincidences in the J-PET detector simulated using GATE package. *Acta Physica Polonica A*, 127:1505–1512, 2015.

[78] Pawlik-Niedźwiecka M. and Shivani. Report from Big Barrel Run-4. *J-PET Report*, (14), 2017.

[79] Skurzok M., ..., Kowalski P. et al. Time calibration of the j-pet detector. *Acta Physica Polonica A*, 132(5):1641, 2017.

[80] Skurzok M. Interthreshold Time Calibration. *J-PET Report*, (4), 2018.

[81] NEMA. Performance measurements of positron emission tomographs. *NEMA Standards Publication*, (NEMA NU 2-2012), 2012.

[82] Yang X. and Peng H. The use of noise equivalent count rate and the NEMA phantom for PET image quality evaluation. *Physica Medica*, 31:179–184, 2015.

[83] Kowalski P. et al. Determination of the map of efficiency of the Jagiellonian Positron Emission Tomograph (j-pet) detector with the GATE package. *Bio-Algorithms and Med-Systems*, 10:85–90, 2014.

[84] Kowalski P. et al. Estimating the NEMA characteristics of the J-PET tomograph using the GATE package. *Physics in Medicine and Biology*, 63:165008, 2018.

[85] Dadgar M. and Kowalski P. GATE simulation study of the 24-module J-PET scanner: data analysis and image reconstruction. *Acta Physica Polonica B*, 51(1), 2020.

[86] Shopa R. Y., ..., Kowalski P. et al. Three-dimensional image reconstruction in J-PET using filtered back projection method. *Acta Physica Polonica B*, 48(10): 1757, 2017.

[87] Witherspoon D. et al. Treatment of axial data in three-dimensional PET. *Journal of nuclear medicine*, 28(11):1717–1724, 1987.

[88] Reynés-Llompart G. et al. Performance characteristics of the whole-body Discovery IQ PET/CT system. *The Journal of Nuclear Medicine*, 58(7):1155–1161, 2017.

[89] Siemens. Online catalogue with technical details. URL `http://www.activexray.com/pdf/Siemens_Biograph.pdf`. 2018-03-29.

[90] Ghabrial A. et al. A Monte Carlo simulation study of the impact of novel scintillation crystals on performance characteristics of PET scanners. *Physica Medica*, 50:37–45, 2018.

[91] Philips. Philips Vereos PET/CT brochure. URL `https://philipsproductcontent.blob.core.windows.net/assets/20170523/360753349c5d4a6aa46ba77c015e75b4.pdf`. 2020-06-29.

[92] Miller M. A. Focusing on high performance. *Philips brochure*, 2016. URL `www.philips.com/VereosPETCT`.

[93] Lacy J. et al. New PET scanner for small animal imaging based on innovative straw detector technology. *The Journal of Nuclear Medicine*, 51:190, 2010.

[94] Crespo P. et al. Whole-body single-bed time-of-flight rpc-pet: simulation of axial and planar sensitivities with nema and anthropomorphic phantoms. *IEEE Transactions on Nuclear Science*, 59(3):520–529, 2012.

[95] Crespo P. et al. Resistive plate chambers in positron emission tomography. *The European Physical Journal Plus*, 128:73, 2013.

[96] Couceiro M. et al. Time-of-flight positron emission tomography with resistive plate chamber detectors: An unlikely but promising approach. *Acta Physica Polonica As*, 127(5):1453–1461, 2015.

[97] EJ-230 datasheet, . URL `https://eljentechnology.com/products/plastic-scintillators/ej-228-ej-230`.

[98] LYSO datasheet, . URL `https://www.crystals.saint-gobain.com/sites/imdf.crystals.com/files/documents/lyso-material-data-sheet_0.pdf`.

[99] LFS datasheet, . URL `http://zecotek.com/zecotek-lfs-scintillation-crystals`.

[100] Kaushik A. et al. Estimation of radiation dose to patients from ^{1}8FDG whole body PET/CT investigations using dynamic PET scan protocol. *The Indian Journal of Medical Research*, 142(6):721, 2015.

[101] Kapłon Ł. Emission spectra of EJ-230 plastic scintillator strip. *J-PET Report*, (7), 2013.

[102] BC-404 datasheet, . URL `http://www.crystals.saint-gobain.com/products/bc400-bc404`.

[103] Kapłon Ł. and Wieczorek A. Quality check of BC-404 and BC-482A plastic scintillator strips. *J-PET Report*, (6), 2017.

[104] BC-482A datasheet, . URL `http://www.crystals.saint-gobain.com/products/bc480-bc482a-bc484`.

[105] Kapłon Ł. *Synthesis and characterization of polystyrene scintillators and their application in positron emission tomography.* PhD thesis, Faculty of Physics, Astronomy and Applied Computer Science, Jagiellonian University, 2017.

[106] Wieczorek A. *Development of novel plastic scintillators based on polyvinyltoluene for the hybrid J-PET/MR tomograph.* PhD thesis, Institute of Physics, Jagiellonian University, 2017.

[107] Wieczorek A., ..., Kowalski P. et al. Novel scintillating material 2-(4-styrylphenyl)benzoxazole for the fully digital and MRI compatible J-PET tomograph based on plastic scintillators. *PLoS ONE*, 12(11), 2017.

[108] R4998 datasheet, . URL `https://www.hamamatsu.com/us/en/product/type/R4998/index.html`.

[109] R9800 datasheet, . URL `https://www.hamamatsu.com/us/en/product/type/R9800/index.html`.

[110] S13361 series datasheet, . URL `https://www.hamamatsu.com/jp/en/product/optical-sensors/mppc/mppc_mppc-array/index.html`.

[111] Silarski M. Polymer scintillators for PET produced commercially. *J-PET Report*, (19), 2012.

[112] Sharma N. G., ..., Kowalski P. et al. Different foils tests. *J-PET Report*, (10), 2014.

[113] Oliver J. F. and Rafecas M. Modelling random coincidences in positron emission tomography by using singles and prompts: A comparison study. *PLOS ONE*, 2016.

[114] Dors catalogue 2012. URL `http://www.dors.com/files/CATALOGUE%202012.pdf`.

[115] SciPy curve_fit documentation. URL `https://docs.scipy.org/doc/scipy/reference/generated/scipy.optimize.curve_fit.html`. 2020-02-16.

[116] Brun R. and Rademakers F. ROOT—an object oriented data analysis framework. *Nuclear Instruments and Methods in Physics Research Section A: Accelerators, Spectrometers, Detectors and Associated Equipment*, 389(1-2):81–86, 1997.